NUMERICAL SIMULATIONS AND OBSERVATIONS OF EQUATORIAL F REGION PLASMA IRREGULARITIES

A Dissertation

Presented to the Faculty of the Graduate School

of Cornell University

in Partial Fulfillment of the Requirements for the Degree of

Doctor of Philosophy

by

Henrique Carlotto Aveiro

August 2012

NUMERICAL SIMULATIONS AND OBSERVATIONS OF EQUATORIAL F REGION PLASMA IRREGULARITIES

Henrique Carlotto Aveiro, Ph.D.

Cornell University 2012

This dissertation describes a theoretical, experimental, and modeling investigation of the plasma irregularities in equatorial spread *F* (ESF). The primary scientific objective is to evaluate the electrodynamic nature of equatorial *F* region plasma instabilities. In particular, the difference between two-dimensional and three-dimensional electrodynamic effects on the onset and evolution of equatorial instabilities is investigated.

Statistical studies are performed using the Jicamarca Unattended Long Term Investigations of the Ionosphere and Atmosphere (JULIA) radar at Jicamarca. The climatology, persistence, and the correlation with the phase of the moon of equatorial spread *F* irregularities are evaluated, and different forecasting tools are compared.

A three dimensional electrostatic numerical model of the equatorial ionosphere using a finite volume method transport scheme is described. The model incorporates realistic ionospheric conductivities, electric fields, and winds. The model is capable of reproducing the full complement of relevant equatorial *F* region ionospheric plasma instabilities under realistic conditions, including bottomside shear flow. Of chief importance is the so-called "collisional shear instability" which has come to light recently as a potentially important mechanism in the initiation of ESF. This instability has a faster growth rate than the conventional generalized Rayleigh Taylor (gRT) instability under typical post-sunset

conditions. The combination of gRT and CSI produces an instability which develops into an intense ESF event more quickly and with more realistic characteristics than the other two independently in simulations. The model is initialized with data acquired by the C/NOFS satellite, the Jicamarca Radio Observatory, ALTAIR radar, and other ground-based instruments.

The forecast potential of the simulation is evaluated through a number of "after the fact" case studies. Various diagnostic codes are used to validate the simulations. To compute the magnetic induction due to ionospheric currents, for example, we solve the partial differencial equation resulting from the Ampère's law for magnetostatics. Airglow emissions corresponding to the simulation runs are likewise computed for the 6300-Å (or oxygen red) line. Simulated airglow images are obtained through the integration of the volume emission rates along the camera line of sight.

Coherent/incoherent scatter simulations corresponding to the model runs show the typical three stages of ESF evolution, from bottom-type to bottomside to topside ESF. Some of the features that the simulated electron density maps share with ALTAIR scans include westward tilted ascending depletions connected to the bottomside, periodic spacing of 100-200 km in the zonal direction, bifurcation, secondary instabilities growing on the western walls of the primaries, and rates of development.

The main goal of these studies has been both to verify the efficacy of the simulation code and its forecast potential while also placing these common but ambiguous diagnostic methods in a formal theoretical/modeling context for the first time.

BIOGRAPHICAL SKETCH

Henrique Carlotto Aveiro was born and raised in Brazil. He joined the graduate school of Electrical and Computer Engineering at Cornell University in the Summer of 2009. Prior to coming to Ithaca, he received a B.S. degree in Electrical Engineering at *Universidade Federal de Santa Maria* (UFSM) and a M.S. degree in Space Geophysics at *Instituto Nacional de Pesquisas Espaciais* (INPE). During the M.S. studies at INPE, he worked with coherent radar and magnetometer observations of the equatorial electrojet. During his years at Cornell University, he became the *dictator* (officially named *President* but was never elected by popular vote) of the Luso-Brazilian Student Association during two terms (2009-2011). As a good Brazilian, his most notable achievement was the 2011 Ithaca Soccer League Championship.

Para meus pais, José Telmo Carvalho Aveiro & Cleudete Carlotto Aveiro,

e minha irmã, Juliana Carlotto Aveiro,

por seu apoio e amor incondicional.

ACKNOWLEDGEMENTS

I would like to thank the members of my Special Committee. My special gratitude goes to my Committee Chair, Prof. David Hysell, for his constant support and accessibility throughout my Ph.D. studies. Thanks for not letting me derail from the scientific career. I also have very deep gratitude to Prof. Michael Kelley. Without his e-mails and letters, Cornell Graduate School would not have accepted me. I thank Prof. Charles Seyler for the hours he spent helping me understand the philosophical views behind magnetohydrodynamics and dynamo simulations. Prof. Peter Diamessis had an indirect but large contribution to my work. He introduced me to the amazing world of computational fluid dynamics. Throughout our interactions, he made me believe that I was born for academia.

Many thanks to Jorge L. Chau and the staff of the Jicamarca Radio Observatory for their prompt communication and for providing me radar data for my research. I also thank Rob Pfaff, Jeff Klenzing, Rod Heelis, Russel Stoneback, Hermann Lühr, and Jaeheung Park, for providing me satellite observations.

I would also like to thank (ex-)members of the Upper Atmosphere/Space Plasma Physics research group at Cornell: Eliana Nossa, Gabriel Michhue, Tatsuhiro Yokoyama, Ronald Ilma, Rob Miceli, Eugene Dao, Roger Varney, and Ben Tang. I will miss the Friday evenings (with $1 beers) at the Big Red Barn with you folks.

My special thanks go to my wife, Karen Osorio, for her love and support. Her company during the first years at Cornell made my life much easier. Being apart from her in the last two years of grad school gave me the strength to work more intensively on my dissertation.

TABLE OF CONTENTS

LIST OF FIGURES

CHAPTER 1

INTRODUCTION

In research, if you know what you are doing, then you shouldn't be doing it.

–Richard W. Hamming, in *Numerical methods for scientists and engineers*

Equatorial spread *F* (ESF) has been recognized for years to be the manifestation of a collection of plasma instability processes that ocurr in the equatorial *F* region of the ionosphere. One of the first papers published in this subject, *Berkner and Wells* (1934), dates from more than 75 years ago and shows the observations of spreading of ionogram traces, which they attributed to kilometer-scale structures in the electron density. Research has been done in order to solve the puzzle behind ESF, but 75 years of research has not been enough (yet!). Different instruments supply hints to the solution of the puzzle. For example, radars provide measurements of electron density fluctuations for a specific wavenumber in a given altitude range and time span. Satellites can measure plasma state parameters along their flight path. Still, other instruments supply more information with varying degrees of ambiguity. No one observation completely captures the phenomenon.

1.1 Background and motivation

This dissertation is written to contribute ideas toward a better understanding of the phenomenology behind ESF. The research presented here is mainly based on the results of three-dimensional numerical simulations of ESF developed during the last 3 years. Those simulations are what we call "full 3-D" since

they do not make use of field line-integrated quantities, or the computation of parallel electric fields based mainly on ambipolar electric fields or other simplification. Three-dimensional simulations are pathologicaly problematic due to large conductivities along the magnetic field lines (plus a larger dependence on computer power and state-of-the-art numerical methods). However, the correct computation of the electrostatic field structure without artificial assumptions seems to be essential. Since simulations prove useful through validation, observations made by remote sensing techniques using incoherent and coherent scatter radars, and *in situ* measurements made by satellite-borne instruments are consulted throughout the dissertation.

The philosophical idea of the dissertation comes from an article by Donald Farley, Emeritus Professor from Cornell University: *Farley et al.* (1970). In the article, he challenges the 70's understanding of ESF. His main conclusion is that none of the present theories (by that time) could explain the observations. Later studies, as e.g. *Haerendel* (1973), coronated a gravitational instability, the *generalyzed Rayleigh-Taylor* (gRT), as the driving mechanism of ESF. Without any attempt to compare the results presented in this dissertation to the contributions from Prof. Farley, we challenge the acceptance of gRT as the sole instability that leads to ESF. Based on theoretical and numerical studies of the *collisional shear* instability (CSI) by *Hysell and Kudeki* (2004), we cast numerical simulations of ESF in a realistic background ionosphere to assess the relative contribution of CSI and gRT. Our goal in developing a model was to evaluate the system as a three-dimensional initial boundary value problem in order to gain additional insight into ESF behavior. The simulation differs in two important respects from other contemporary simulations (e.g. *Retterer* (2005); *Huba and Joyce* (2007); *Huba et al.* (2008); *Yokoyama et al.* (2009)). One difference is that it solves the potential equa-

tion in three dimensions fully rather than assuming equipotential magnetic field lines. This opens the door to the possible effects of drift waves and related instabilities that may play secondary roles in ESF (*Huba and Ossakow*, 1979; *LaBelle et al.*, 1986; *Hysell et al.*, 2002). It also allows us to keep track of the distribution of parallel currents and of the parallel closure of currents forced by dynamos. Magnetic field lines cease to be equipotentials near the bottom of the *E* region, decoupling the plasma and decreasing the conductive loading on the dynamo. This may influence the overall plasma circulation. Also, as later shown in Chapter 8, the equipotential field line approach is unable to describe the structure of the ionosphere currents accurately.

1.2 Organization

We start Chapter 2 with a review of equatorial spread *F* theories and observations. Chapter 3 describes statistical studies using the Jicamarca Unattended Long Term Investigations of the Ionosphere and Atmosphere (JULIA) radar at Jicamarca. The climatology, persistence, and the correlation with the phase of the moon of equatorial spread *F* irregularities are evaluated. Different forecasting tools are compared and show, for instance, that lunar tides affect the occurrence of ESF during geomagnetically quiet periods.

Chapters 4–7 include three-dimensional numerical simulations of plasma density irregularities in the postsunset equatorial *F* region ionosphere leading to equatorial spread *F*. The simulations advance the plasma number density and electrostatic potential forward in time by enforcing the constraints of quasineutrality and momentum conservation. In Chapter 4, we describe simulations for

cases with no background winds, with no background electric field or gravity, and with winds, a background electric field, and gravity all working in concert. Chapter 5 shows a simulation incorporating C/NOFS satellite data which partially specify the forcing. Simulation results are compared to ALTAIR radar observations in the Pacific sector. Chapter 6 describes a study of perturbations to magnetic field generated by disruptions in the ionospheric currents during equatorial spread *F*. Simulated satellite passes are performed and compared with observations by the CHAMP satellite magnetometer. In Chapter 7, numerical simulations are evaluated using three different diagnostics including *in situ* observations of satellite-borne magnetometers and remote sensing observations made by coherent/incoherent scatter radar and airglow imagers.

Chapter 8 presents an evaluation of the electrostatic potential in the ionosphere under ESF conditions using three different approaches. First, we calculate the potential using an analytical approach, applying force balance laws to a simplified ionosphere. Second, we compute the potential around a cylinder-like plasma depletion in an idealized ionosphere using both the equipotential field line (EFL) approach and the full 3-D solution to the electrostatic potential problem numerically. Our third approach involves an initial boundary value simulation in a realistic ionosphere using both EFL and 3-D potential solutions.

Finally, in Chapter 9, conclusions and future studies envolving the numerical simulations and equatorial spread *F* are described.

1.3 List of reviewed publications

- Aveiro, H. C., D. L. Hysell, Three-dimensional numerical simulations of equatorial spread *F*: results and observations in the Peruvian sector, AGU Monograph on *Modeling the Ionosphere-Thermosphere System*, *submitted*, 2012.
- Aveiro, H. C., D. L. Hysell, Implications of the equipotential field line approximation on equatorial spread *F*, *Geophys. Res. Lett.*, *in press*, 2012.
- Aveiro, H. C., D. L. Hysell, R. G. Caton, K. M. Groves, J. Klenzing, R. F. Pfaff, R. A. Stoneback, and R. A. Heelis, Three-dimensional numerical simulations of equatorial spread *F*: results and observations in the Pacific sector, *J. Geophys. Res.*, *117*, A03325, 2012.
- Aveiro, H. C., D. L. Hysell, J. Park, and H. Lühr, Equatorial spread *F*-related currents: Three-dimensional simulations and observations, *Geophys. Res. Lett.*, *38*, L21103, 2011.
- Aveiro, H. C., and D. L. Hysell, Forecast assessment of topside spread *F* at Jicamarca, *J. Geophys. Res.*, *115*, A12331, 2010*b*.
- Aveiro, H. C., and D. L. Hysell, Three-dimensional numerical simulation of equatorial *F*-region plasma irregularities with bottomside shear flow, *J. Geophys. Res.*, *115*, A11321, 2010*a*.

CHAPTER 2

THE IONOSPHERIC POST-SUNSET SCENARIO

In five minutes you will say that it is all so absurdly simple.

–Sherlock Holmes, in *The Adventure of the Dancing Men*
Sir Arthur Conan Doyle

This chapter presents a compilation of important information that offers clues about the nature of equatorial spread *F*. Certainly, this chapter does not intend to cover every aspect of ESF theory and observations. Complete reviews of the phenomenon can be found in the literature, as e.g. *Fejer and Kelley* (1980), *Ossakow* (1981), *Fejer and Hysell* (1998), *Kelley and Hysell* (1991), *Hysell* (2000), *Kelley* (2009), *Woodman* (2009), and *Kelley et al.* (2011).

2.1 The Earth's ionosphere

The ionosphere is a weakly ionized portion of the atmosphere located between approximately 60 and 1500 km altitude. The ionospheric plasma is mainly created by the interaction of short wavelength solar radiation and precipitating energetic particles with the neutral atmosphere. The ionosphere is usually subdivided in three layers: *D*, *E*, and *F*. Figure 2.1 and Figure 2.2 show vertical profiles of the densities of the major ionospheric species obtained from the International Reference Ionosphere (IRI-2007) model (*Bilitza and Reinisch*, 2008) for daytime and nighttime, respectively. The *D* region is located between about 60 km and 90-95 km. Its main source of ionization is photoionization of NO by Lyman-α radiation. Also, high energy cosmic rays contribute to the ionization of O_2 and

N_2 below 70 km. The *E* region is the portion of the Earth's ionosphere located between about 90-95 km and 130 km altitude. The diurnal variation of the *E* region is characterized by an α-Chapman layer (*Hargreaves*, 1992). The maximum electron density of the *E* region tipically varies from $5{\times}10^9$ electrons/m^3 during nighttime to $\sim 10^{11}$ during daytime. The *F* region begins above 130 km and is sometimes subdivided into two layers (during the day), F_1 and F_2 (*Brasseur and Solomon*, 2005). The main source of *F* region ionization is the interaction of the extreme ultraviolet radiation with atomic oxygen and molecular nitrogen. The F_1 layer is composed primarily by O^+, and its electron density peaks around 170 km altitude (*Kivelson and Russel*, 1995). The maximum electron density in the ionosphere, the *F* peak, is located at the F_2 layer. Above it, the electron density decreases, and helium (He^+) and hydrogen (H^+) ions become important (*Brasseur and Solomon*, 2005).

2.2 Ionospheric dynamo theory

Neglecting stress, heat flow, and inertia, the fluid continuity and momentum equations for the ionized species α are given as:

$$\frac{\partial n_\alpha}{\partial t} + \nabla \cdot (n_\alpha \mathbf{v}_\alpha) = P_\alpha - L_\alpha, \tag{2.1}$$

$$\begin{aligned} 0 = \quad & -\nabla p_\alpha + n_\alpha q_\alpha (\mathbf{E} + \mathbf{v}_\alpha \times \mathbf{B}) \\ & + m_\alpha n_\alpha [\mathbf{g} - \nu_{\alpha n}(\mathbf{v}_\alpha - \mathbf{U}) - \sum_{\beta}^{\alpha \neq \beta} \nu_{\alpha\beta}(\mathbf{v}_\alpha - \mathbf{v}_\beta)], \end{aligned} \tag{2.2}$$

where $p_\alpha = n_\alpha k_B T_\alpha$ is the thermal pressure. The magnetic pressure is much smaller than the thermal contribution and thus is neglected (i.e., the ionosphere is a low β plasma). The variables n_α, q_α, m_α, T_α, P_α, L_α, and $\mathbf{v}_\alpha$ are number density, electric charge, mass, temperature, production and loss rates, and velocity

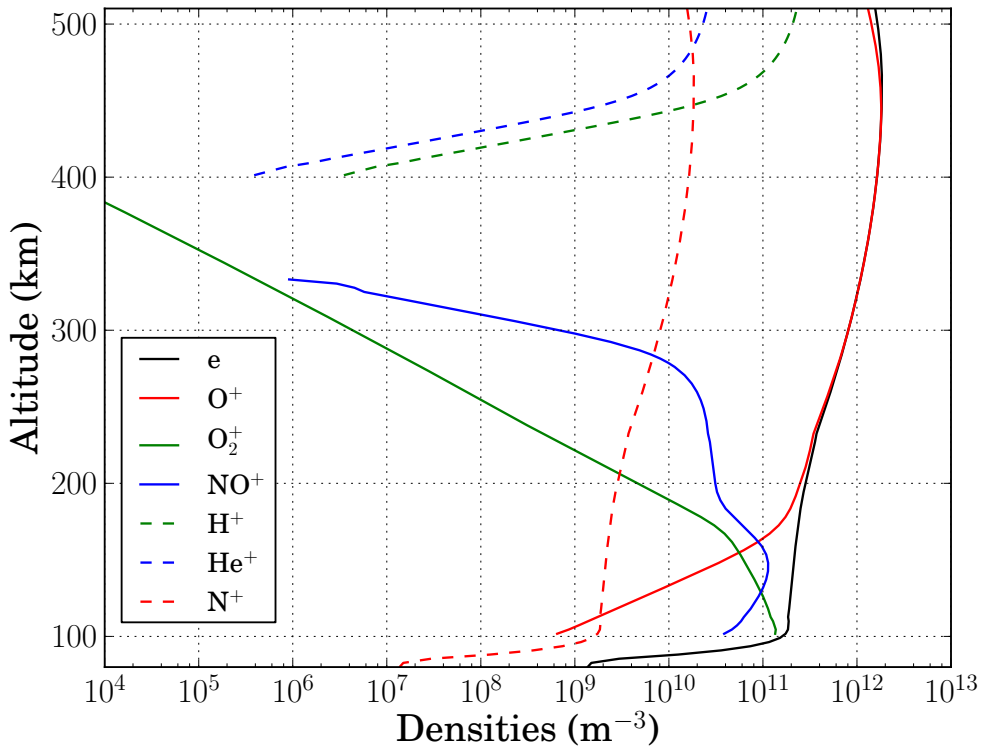

Figure 2.1: Vertical profiles of densities of major species during daytime.

of the species α, respectively. The loss term includes charge exchange and dissociative recombination for a given species. Here, β represents the other ionized bodies that exchange momentum or energy with α. The terms $\nu_{\alpha\beta}$ and $\nu_{\alpha n}$ are the collision rates with ionized species β and neutrals, respectively. The terms **E**, **B**, **U**, **g**, and k_B represent the electric field, magnetic field, neutral wind, gravity, and the Boltzmann constant, respectively.

Assuming that ion-neutral (Maxwell molecule) collisions are more frequent than Coulomb collisions and that the total electron collision rate is the combination of electron-ion (Coulomb) and electron-neutral (Maxwell molecule) collisions, a general explicit equation for the species velocity in the directions perpendicular and parallel to the magnetic field can be obtained from Equation 2.2

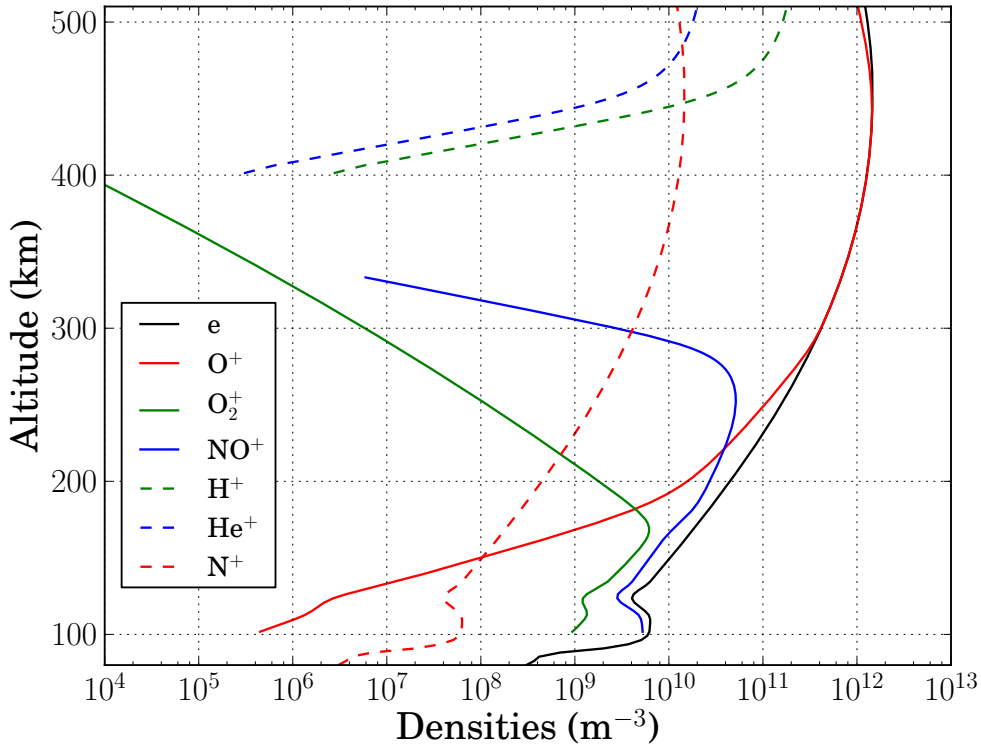

Figure 2.2: Vertical profiles of densities of major species during nighttime.

and expressed, respectively, as

$$\begin{aligned}\mathbf{v}_{\alpha\perp} &= \frac{\Omega_\alpha \nu_\alpha}{|\mathbf{B}|(\Omega_\alpha^2+\nu_\alpha^2)}(\mathbf{E}_\perp + \mathbf{U}\times\mathbf{B}) + \frac{\Omega_\alpha^2}{|\mathbf{B}|(\Omega_\alpha^2+\nu_\alpha^2)}(\mathbf{E}+\mathbf{U}\times\mathbf{B})\times\hat{\mathbf{b}} \\ &\quad -\frac{\nu_\alpha}{\Omega_\alpha^2+\nu_\alpha^2}\frac{k_B T_\alpha}{m_\alpha}\nabla_\perp \ln n_\alpha - \frac{\Omega_\alpha}{\Omega_\alpha^2+\nu_\alpha^2}\frac{k_B T_\alpha}{m_\alpha}\nabla_\perp \ln n_\alpha \times \hat{\mathbf{b}} \\ &\quad +\frac{\nu_\alpha}{\Omega_\alpha^2+\nu_\alpha^2}\mathbf{g}_\perp + \frac{\Omega_\alpha}{\Omega_\alpha^2+\nu_\alpha^2}\mathbf{g}\times\hat{\mathbf{b}} + \mathbf{U}_\perp \end{aligned} \tag{2.3}$$

and

$$v_{\alpha\parallel} = -\frac{k_B T_\alpha}{m_\alpha}\nabla_\parallel \ln n_\alpha + \frac{\mathbf{g}_\parallel}{\nu_\alpha} + \frac{q_\alpha}{m_\alpha \nu_\alpha}\mathbf{E}_\parallel + U_\parallel, \tag{2.4}$$

where $\hat{\mathbf{b}} = \frac{\mathbf{B}}{|\mathbf{B}|}$ and Ω_α is the (signed) species gyrofrequency ($=\frac{q_\alpha}{|\mathbf{B}|m_\alpha}$). The resulting plasma current density $\mathbf{J}$ ($=\sum_\alpha n_\alpha q_\alpha \mathbf{v}_\alpha$) is given by

$$\mathbf{J} = \sigma_P(\mathbf{E}_\perp + \mathbf{U}\times\mathbf{B}) + \sigma_H\hat{\mathbf{b}}\times(\mathbf{E}+\mathbf{U}\times\mathbf{B}) + \sigma_o E_\parallel$$

$$-\sum_{\alpha}\left(d_{P\alpha}\nabla_{\perp}n_{\alpha}+d_{H\alpha}\nabla n_{\alpha}\times\hat{\mathbf{b}}+d_{o\alpha}\nabla_{\parallel}n_{\alpha}\right)$$
$$+\gamma_{P}\mathbf{g}_{\perp}+\gamma_{H}\mathbf{g}\times\hat{\mathbf{b}}+\gamma_{o}\mathbf{g}_{\parallel}, \tag{2.5}$$

where the σ, d, and γ terms are conductivity, diffusion, and gravity coefficients, respectively. The subscripts P, H, and o indicate Pedersen, Hall, and direct (parallel to the magnetic field) quantities, respectively (see full derivation in Appendix C). The coefficients are given by

$$\sigma_{P}=\sum_{\alpha}n_{\alpha}q_{\alpha}\frac{\Omega_{\alpha}\nu_{\alpha}}{|\mathbf{B}|(\Omega_{\alpha}^{2}+\nu_{\alpha}^{2})};\ \sigma_{H}=-\sum_{\alpha}n_{\alpha}q_{\alpha}\frac{\Omega_{\alpha}^{2}}{|\mathbf{B}|(\Omega_{\alpha}^{2}+\nu_{\alpha}^{2})};\ \sigma_{o}=\sum_{\alpha}\frac{n_{\alpha}q_{\alpha}^{2}}{m_{\alpha}\nu_{\alpha}} \tag{2.6}$$

$$d_{P\alpha}=\frac{q_{\alpha}\nu_{\alpha}}{\Omega_{\alpha}^{2}+\nu_{\alpha}^{2}}\frac{k_{B}T_{\alpha}}{m_{\alpha}};\ d_{H\alpha}=\frac{q_{\alpha}\Omega_{\alpha}}{\Omega_{\alpha}^{2}+\nu_{\alpha}^{2}}\frac{k_{B}T_{\alpha}}{m_{\alpha}};\ d_{o\alpha}=\frac{q_{\alpha}}{\nu_{\alpha}}\frac{k_{B}T_{\alpha}}{m_{\alpha}} \tag{2.7}$$

$$\gamma_{P}=\sum_{\alpha}\frac{n_{\alpha}q_{\alpha}\nu_{\alpha}}{\Omega_{\alpha}^{2}+\nu_{\alpha}^{2}};\ \gamma_{H}=\sum_{\alpha}\frac{n_{\alpha}q_{\alpha}\Omega_{\alpha}}{\Omega_{\alpha}^{2}+\nu_{\alpha}^{2}};\ \gamma_{o}=\sum_{\alpha}\frac{n_{\alpha}q_{\alpha}}{\nu_{\alpha}}. \tag{2.8}$$

For an electrostatic model (i.e., neglecting electromagnetic effects), the current density is solenoidal ($\nabla\cdot\mathbf{J}=0$) and the total electric field can be written as a combination of a background electric field ($\mathbf{E}_{o}$) and a polarization potential ($\nabla\Phi$) as $\mathbf{E}=\mathbf{E}_{o}-\nabla\Phi$. The dynamo forcing term, the polarization potential, is obtained from the solenoidal curret density through

$$\nabla\cdot\left[\hat{\Sigma}\cdot\nabla\Phi\right]=\nabla\cdot\mathbf{J}_{0}, \tag{2.9}$$

where $\hat{\Sigma}$ is the conductivity tensor. The total current density can be written as a combination of the background ($\mathbf{J}_{0}$), the polarization ($\hat{\Sigma}\cdot\nabla\Phi$), and the (divergence-free) diamagnetic ($\mathbf{J}_{d}$) current densities (i.e., $\mathbf{J}=\mathbf{J}_{0}+\hat{\Sigma}\cdot\nabla\Phi+\mathbf{J}_{d}$). Using a magnetic dipole coordinate system, where p is the McIlwain parameter (L), q is a coordinate parallel to the magnetic field, and ϕ is longitude in radians,

the PDE in Equation 2.9 can be rewritten as

$$\frac{\partial}{\partial\phi}\left[h_p h_q\left(\sigma_P\frac{1}{h_\phi}\frac{\partial\Phi}{\partial\phi}+\sigma_H\frac{1}{h_p}\frac{\partial\Phi}{\partial p}\right)\right]+\frac{\partial}{\partial p}\left[h_q h_\phi\left(-\sigma_H\frac{1}{h_\phi}\frac{\partial\Phi}{\partial\phi}+\sigma_P\frac{1}{h_p}\frac{\partial\Phi}{\partial p}\right)\right]$$
$$+\quad\frac{\partial}{\partial q}\left[h_p h_\phi\left(\sigma_o\frac{1}{h_q}\frac{\partial\Phi}{\partial q}\right)\right]=\frac{\partial}{\partial\phi}(h_p h_q J_{0\phi})+\frac{\partial}{\partial p}(h_q h_\phi J_{0p})+\frac{\partial}{\partial q}(h_p h_\phi J_{0q}),\qquad(2.10)$$

where the h's are scale factors. Equations for the scale factors and coordinate transformation are given in Appendix A.

The presence of neutral wind motions driven by tidal oscillations that propagate from below and by *in situ* absorption of solar radiation in the ionosphere play an important role in the generation of global electric fields and currents. The denomination "ionospheric dynamo" comes from the analogy of this system with the conversion of mechanical to electrical energy by an electrical generator, i.e., a dynamo. It is worth mentioning that variations in the conductivities also play a role. For instance, steep vertical gradients in the conductivities at the equatorial E region altitudes lead to a large zonal current known as equatorial electrojet (see e.g., *Forbes* (1981)).

Figure 2.3 shows vertical profiles of daytime (DT) and nighttime (NT) ionospheric conductivities. Plasma mobilities were calculated using neutral composition and temperature estimates from the Mass Spectrometer and Incoherent Scatter (NRL-MSISE00) model (*Picone et al.*, 2002) and ionospheric composition estimates from the International Reference Ionosphere (IRI-2007) model (*Bilitza and Reinisch*, 2008). Expressions for the ion-neutral and electron-neutral collision frequencies used to compute conductivities are taken from *Richmond* (1972). The direct conductivity is much larger than Pedersen and Hall conductivities througout the E and F regions during both daytime and nighttime. The Hall conductivity has a single peak at E region altitudes. Its amplitude is reduced during nighttime due to (the fast) molecular recombination. The Pedersen con-

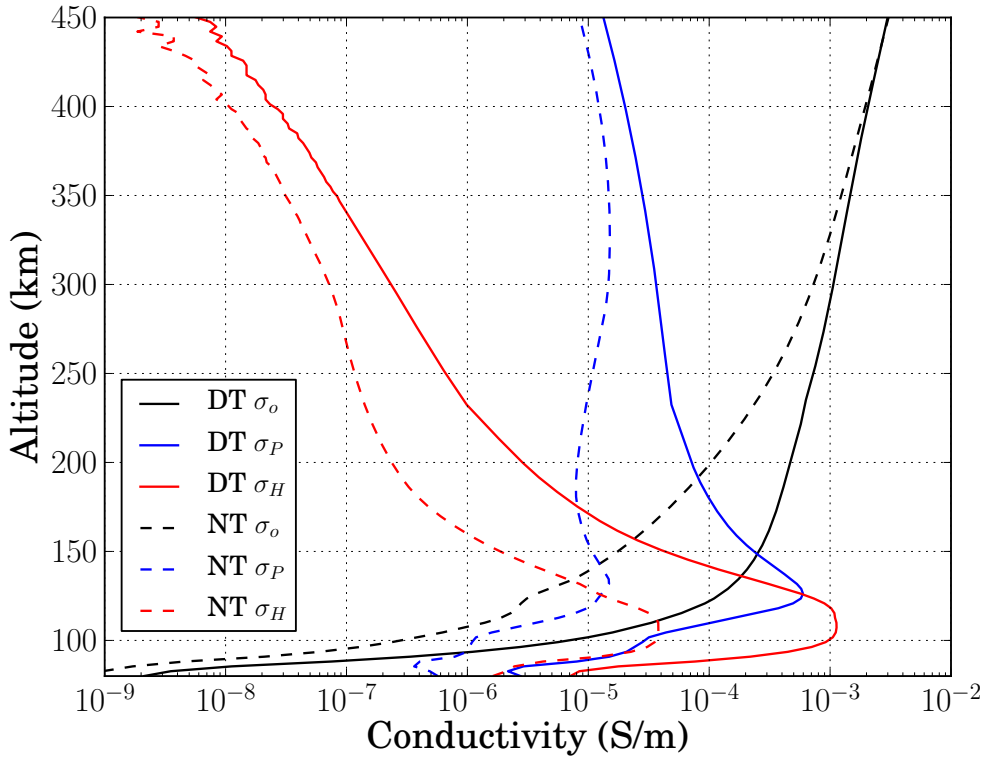

Figure 2.3: Vertical profiles of daytime (DT) and nighttime (NT) ionospheric conductivities: (black) direct (σ_o), (red) Hall (σ_H), (blue) Pedersen (σ_P) conductivities. σ_o is downscaled by a 10^4 factor for visualization.

ductivity peaks at the *E* region during daytime, but it becomes comparable to *F* region magnitudes during nighttime. Large transverse (Pedersen and Hall) conductivities at *E* region altitudes lead to the circulation of large horizontal currents known as solar quiet (S_q) and equatorial electrojet (see *Forbes* (1981) for a review). The competition between the *E* and *F* region Pedersen conductivities plays a major role in the development of post-sunset ionospheric irregularities. During this period, due to large zonal gradients in the conductivities, the ionospheric currents establish new paths and give rise to large vertical currents we now believe to be essential for the triggering of equatorial spread *F*.

2.3 Post-sunset scenario and zonal plasma shear flow

Around sunset, the transfer of dominance from the *E* region to the *F* region dynamo creates a shear in the horizontal plasma flow in the equatorial *F* region bottomside (*Haerendel et al.*, 1992). Above the shear node, the vertical electric field points downward, and the plasma drifts eastward (see Figure 2.4). Below the node, the vertical electric field points upward, and the plasma drifts westward, even though the neutral flow is everywhere eastward (*Kudeki et al.*, 1981; *Tsunoda et al.*, 1981). Several factors contribute to shear flow, including *E* region dynamo winds, vertical winds and horizontal electric fields on flux tubes with significant Hall conductivity, and vertical currents sourced in the electrojet region near the solar terminator (see *Haerendel et al.* (1992) and *Haerendel and Eccles* (1992) for reviews). The imperfectly efficient *F* region dynamo sets up a vertical current supplied in part by field-aligned currents connecting the equatorial *F* region to the *E* layer at low-to-mid latitudes. Related to this phenomenon, a family of plasma irregularities collectively referred to as equatorial spread *F* (ESF) disturbs the nighttime equatorial *F* region (see review by *Woodman* (2009)).

It is known that layers of plasma irregularities (called bottom-type layers) exist near the region of shear flow, beneath the node (*Woodman and La Hoz*, 1976; *Woodman*, 2009). These layers, which often form at sunset, serve as precursors for more dynamic equatorial spread *F* events. The layers may persist for several hours but do not develop vertically over time, remaining confined to layers usually less than 50 km thick. Once they disappear on a given night, they do not reappear. Nor are they seen after bottomside layers or topside plumes make their first appearances (*Hysell*, 2000). *Kudeki and Bhattacharyya* (1999) argued that the irregularities in bottom-type layers are generated by conventional wind-

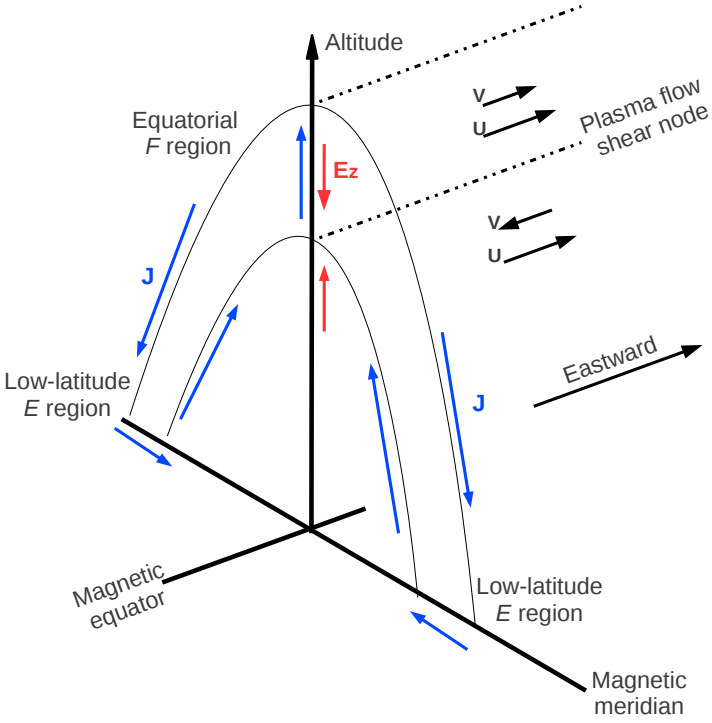

Figure 2.4: Sketch of the plasma horizontal shear flow. The archs represent the magnetic field lines. Ionospheric currents (**J**) (in blue) connect the equatorial *F* region to the low latitude *E* region. Neutral and plasma velocities are denoted by **u** and **v**, respectively. Above (below) the shear node, the vertical electric field ($\mathbf{E}_z$) (in red) points downward (upward), and the plasma flows eastward (westward). Below the node, neutrals and plasma flow in opposite directions. Note that zonal currents are not represented in the sketch.

driven gradient drift instabilities which are readily excited in regions of retrograde plasma drift (where the local plasma velocity and neutral wind are antiparallel) and where zonal conductivity gradients, of the kind that arise across the solar terminator at sunset, also exist. *Hysell et al.* (2004) then presented radar imagery supporting the *Kudeki and Bhattacharyya* (1999) hypothesis regarding wind-driven gradient drift instabilities and also showing that bottom-type irregularities frequently occur in patches arranged periodically in the zonal direction. They surmised that the periodicity was caused by large-scale waves, the

different phases of which being alternately stable and unstable to wind-driven instability. Such waves, if present, could precondition large-scale interchange instabilities and equatorial spread *F*.

The necessity of a some kind of ancillary process for initiating ESF has long been appreciated. Using the flux-tube-integrated formalism introduced by *Haerendel* (1973), it can readily be shown that, in the absence of unusually strong storm-time electric fields at the magnetic equator, the e-folding growth time for the generalized Rayleigh-Taylor (gRT) instability is seldom less than about 15–20 min. in the postsunset bottomside *F* region and seldom for more than one or two e-folding times under moderate solar-flux conditions (see for example *Sultan* (1996); *Retterer et al.* (2005); *Krall et al.* (2009); *Singh et al.* (2010).) The time of most rapid wave growth is generally about 1900 SLT, depending on season, solar cycle, and longitude. How is it possible then for large-scale depletions and radar plumes to start appearing by 2000 SLT and earlier? The large-scale waves suggested by the bottom-type layers would seem to be relevant to this question.

The predominance of large-scale waves in the the postsunset equatorial ionosphere has been highlighted by *Tsunoda and White* (1981), *Kil and Heelis* (1998), and *Tsunoda* (2005). Their source is often attributed to gravity waves (*Röttger*, 1973; *Kelley et al.*, 1981; *Singh et al.*, 1997; *McClure et al.*, 1998). This hypothesis is difficult to test experimentally, however, since only the effects of gravity waves and not the gravity waves themselves can be detected in the thermosphere using incoherent scatter radars (ISR). *Vadas and Fritts* (2004) were among the first to address the issue theoretically, showing that a spectrum of gravity waves launched by mesoscale convection cells could survive wind shears and viscous and conductive damping and penetrate into the lower

thermosphere. However, the preferred range of horizontal wavelengths for the surviving gravity waves was about 50–150 km. This barely includes but does not favor either the 30 km or the 200+ km large scale waves preferentially seen in experiments at Jicamarca and Kwajalein (e.g. *Hysell et al.* (2006*b*)).

2.4 Previous numerical studies of equatorial spread *F*

Numerical simulations of ESF have been used as a tool for the understanding the mechanisms behind it. The first numerical simulation of the collisional gRT mechanism in the post-sunset equatorial *F* region was done by *Scannapieco and Ossakow* (1976). Their model had initially been designed for nonlinear studies of *F* region barium clouds (*Scannapieco et al.*, 1976), but by a suggestion of Dr. Ronald Woodman, the numerical model was modified to run ESF simulations (see the timeline in *Woodman* (2009)). Two-dimensional ESF simulations were also performed by *Zalesak and Ossakow* (1980), *Zalesak et al.* (1982), *Zargham and Seyler* (1989), *Huang and Kelley* (1996), and *Chou and Kuo* (1996). For instance, *Zargham and Seyler* (1989) performed 2-D simulations of the interchange instability in both collisional and inertial regime using a Navier-Stokes solver. In the collisional regime, the irregularities presented anisotropic structure with nonlinear states due to dominant effect of Pedersen current on the accumulation and relaxation of space charges in regions of density perturbation in the plane perpendicular to the density gradient. In the inertial regime, isotropic rotational flow was observed. The bubble shape resembled a folded circular cap with associated generation of shed vortices. The plasma irregularity development in the collisional and inertial regime was similar during the initial phase, but significant differences were present in the nonlinear phase.

Guzdar et al. (1983) evaluated the influence of a transverse velocity shear on the gRT instability. Their linear nonlocal theory predicts that the Kelvin-Helmholtz (KH) instability can reduce the growth rate of gRT in the short wavelength regime. They tried to explain the long wavelength oscillations of the bottomside of the *F* layer in terms of the velocity shear, but the magnitude of the velocity shear was approximately 10 times larger than the observed values in nature.

However, *Hysell and Kudeki* (2004) proposed that shear flow itself could be the source of the large-scale waves. They followed the formalism developed by *Keskinen et al.* (1988) who assessed the viability of electrostatic KH instabilities in the auroral *F* region. That study suggested that ion-neutral collisions damp the instability in the ionosphere. In their 2-D fluid model, *Hysell and Kudeki* (2004) assumed the current to be dominated by the ion Pedersen and polarization currents:

$$\mathbf{J} = \frac{nq}{\Omega_i B}\left[\nu_{in}(\mathbf{E} + \mathbf{U} \times \mathbf{B}) + \left(\frac{\partial}{\partial t} + \mathbf{v} \cdot \nabla\right)\mathbf{E}\right]. \tag{2.11}$$

In addition, they used the continuity equation (Eq. 2.1) and the quasineutrality condition ($\nabla \cdot \mathbf{J} = 0$). They linearized these equations in the form:

$$\begin{aligned} n(x,z) &= n_\circ(z) + n_1(z)\exp(i(kx - \omega t)) \\ \phi(x,z) &= \phi_\circ(z) + \phi_1(z)\exp(i(kx - \omega t)) \end{aligned} \tag{2.12}$$

where k is the horizontal wavenumber and a plane wave dependence is assumed in the $\hat{x}$ direction but where the vertical variation ($\hat{y}$ direction) in the fields is retained explicitly. The subscripts "$\circ$" indicate background parameters, where the background zonal drift velocity has the form $\mathbf{v}_\circ = \hat{y} \times \nabla\phi_\circ / B$. The

resulting dispersion relation derived by *Hysell and Kudeki* (2004) is given by

$$(\omega + i\nu_{in} - kv_\circ)\left[\frac{d}{dz}\left(n_\circ\frac{d\phi_1}{dz}\right) - n_\circ k^2\phi_1\right] = - in_\circ\frac{d\nu_{in}}{dz}\frac{d\phi_1}{dz} - k\frac{d}{dz}\left(n_\circ\frac{dv_\circ}{dz}\right)\phi_1 - ik\frac{d}{dz}\left(\nu_{in}\frac{u - v_\circ}{\omega - kv_\circ}\frac{dn_\circ}{dz}\phi_1\right) \quad (2.13)$$

Using a nonlocal analysis, *Hysell and Kudeki* (2004) plugged in idealized profile shapes of zonal velocity, ion collision, and ion density to Eq. 2.13 and solved the eigenvalue problem for the complex frequency $\omega = \omega_r + i\gamma$, where γ is a wavenumber dependent growth rate. They found a collisional branch of the instability that could operate (in the collisional regime) in regions of strong, retrograde plasma motion, i.e., where the differential velocity between ions and neutrals maximize. The retrograde motion and associated vertical current, not the shear, is key to the instability, although the shear is inherently present and must be considered and accounted for. The growth rate of what was termed a "collisional shear instability" or CSI was found to be potentially several times greater than that of the Rayleigh-Taylor instability under nominal conditions. Nonlocal analysis predicted that the growth rate should be a maximum for $kL \sim 1/2$, where L is the vertical scale length of the shear. Taking $L \sim 15$ km on the basis of typical observations therefore implies a preferred wavelength of about 200 km. The associated e-folding time was later predicted to be about 5 min. An initial value analysis meanwhile suggested that the instability could also exhibit a much shorter dominant wavelength in its early stages, of the order of a few times L in simulation. The transient response of the instability could therefore account for the decakilometric large-scale waves in the post-sunset ionosphere while the asymptotic response (the boundary value problem result) could account for the 200+ km large scale waves observed. Although short lived, the transient response entails even faster growth than the asymp-

totic response (*Kudeki et al.*, 2007). CSI therefor can account for the scales and rapid growth of the dominant irregularities observed by radar in ESF. Topside irregularities are driven by the gRT instability near and above the *F* peak. This is a universal instability (i.e., nearly scale independent), and thus gRT theory cannot explain by itself the predominant scale sizes of ESF irregularities.

In recent years, efforts to simulate ESF in three-dimensions have been made either using quasi-three-dimensional models incorporating magnetic flux tube integrated quantitities (as e.g., *Huba et al.* (2008) and *Retterer* (2010)) or incorporating the full 3-D solution for the electrostatic potential (*Keskinen et al.*, 2003). Those models seem to emphasize the role of gRT while mainly neglecting CSI. The work we present in the subsequent chapters shows that the two instabilities function together in nature: CSI appears neither to suppress gRT nor merely to seed it; rather, the two mechanisms appear to grow and develop faster when acting together than either when acting alone, exhibiting a greater mixing depth (*Aveiro and Hysell*, 2010*a*).

2.5 Observational perspective

In order to begin to evaluate the accuracy and utility of the simulations presented in the next chapters, examples of ESF observations made by coherent/incoherent scatter radar and airglow cameras are shown.

ALTAIR incoherent scatter radar (on Kwajalein Atoll) observations were made over ten nearly contiguous evenings in the Summer of 2004 starting at about 0845 UT. ESF appeared on nine out of the ten nights. Figure 2.5 shows an ALTAIR scan taken at about 1015 UT. The radar scan, which is typical of

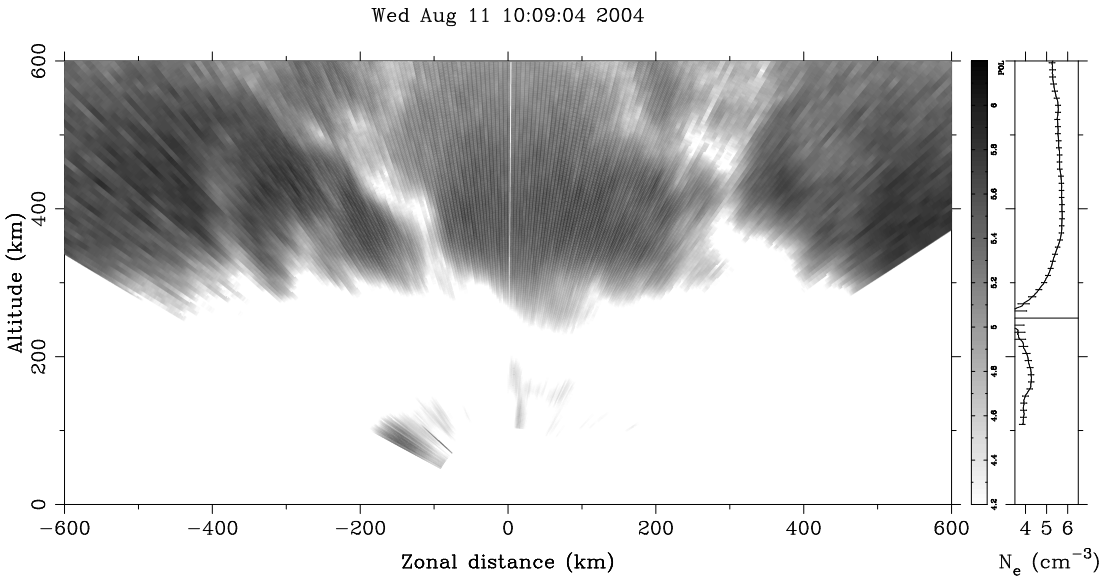

Figure 2.5: Plasma density over Kwajalein measured by the ALTAIR incoherent scatter radar on August 7, 2004, 1009 UT during the NASA EQUIS II sounding rocket campaign. A vertical plasma density profile is plotted to the right. Some meteorological clutter is present in ranges between 100-200 km.)

the Kwajalein observations, shows large-scale waveforms occupying altitudes mainly between about 250–500 km by this time. The dominant waveforms have the ying-and-yang characteristic of ascending depletions (descending enhancements) tilting to the west (east). The highest depletions are connected to the bottomside via very thin channels. The separation distance between the most prominent depletions is about 150–200 km. The relative density perturbation amplitude is close to 100% in both cases. While the ALTAIR data exhibit considerable fine structure, evidence of secondary instabilities, and so forth, the 45-km radar pulse width combined with the incoherent integration requirement for ISR data analysis severely limits the spatial resolution of images like Figure 2.5.

A prototypical example of bottomside spread *F* irregularities is shown in Figure 2.6. The figure shows coherent scatter intensity from small-scale field-aligned plasma density irregularities observed over Jicamarca. The data were taken on August 29, 2004. The range time intensity plot shows backscatter intensity rather than plasma number density. It can be interpreted as an indication of the altitude and local-time extent of plasma instabilities. In this example, a bottom-type layer was observed between about 2130–2210 LT. Thin, seemingly undifferentiated layers like these were the impetus for our modeling effort and are believed to represent wind-driven gradient drift instabilities growing on horizontal conductivity gradients created either by CSI or by the solar terminator. They are often precursors of large-scale depletions and strong ESF events. In this case, however, the bottom-type layer gave way to a bottomside layer which persisted until about local midnight.

The bottomside layer occupied altitudes mainly between about 200–350 km. While no plumes were produced, signatures of primary, intermediate-scale plasma waves just large enough to be resolved by Jicamarca are visible above about 300 km. The altitude range of the irregularities is too low to be explained by gRT, which operates preferentially in the steepest part of the bottomside. It is a better match for the CSI. Interferometry data confirm that strong zonal shear flow existed throughout most of the event. The persistent confinement of the irregularities to a narrow range of altitudes further argues against gRT and for CSI, which may therefore be the primary mechanism behind not only bottom-type layers but at least some fraction of the bottomside layers observed.

The Jicamarca 50 MHz radar is not fully steerable like ALTAIR, but this limitation has been overcome to some extent with the advent of ionospheric radar

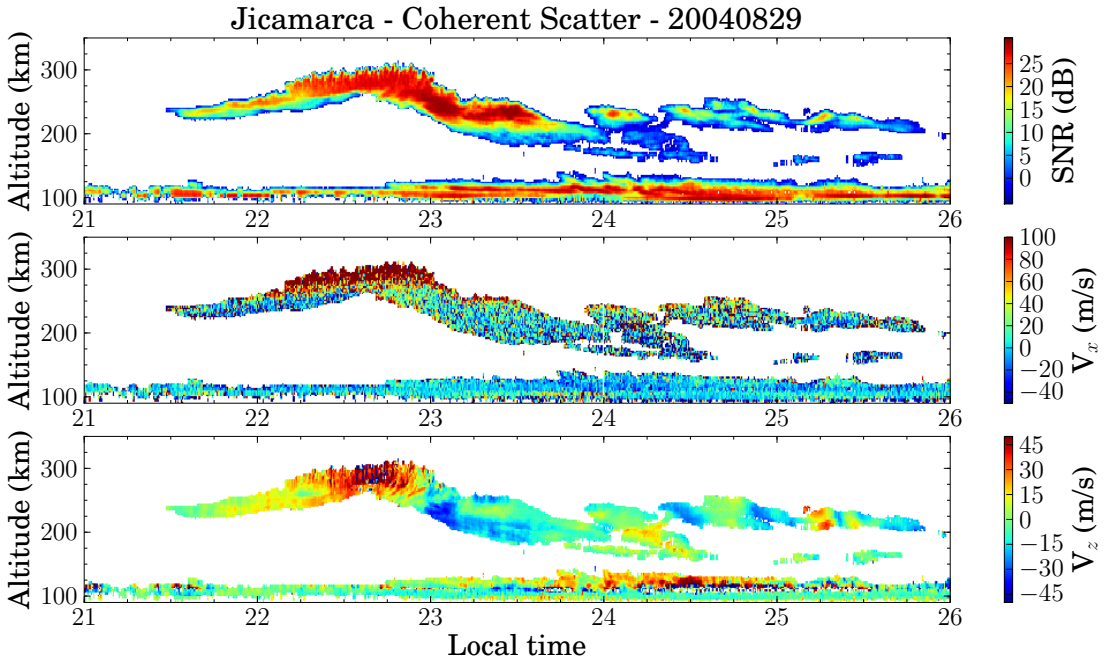

Figure 2.6: Range time intensity representation of a bottomside ESF event over Jicamarca on August 29, 2004. (Top) Coherent backscatter from 3-m scale field-aligned irregularities within the plasma. Colorscale indicate backscatter signal-to-noise ratio (in dB). (Middle) Zonal and (bottom) vertical velocity of the plasma irregularities (in m/s).

imaging (*Hysell*, 1996; *Woodman*, 1997). The right panel of Figure 2.7 shows a typical range time intensity representation of ESF. Bottom-type layers are observed during the first hours after sunset (1920–2100 LT) followed by a sequence of "C-shape" topside irregularities periodically spaced by ~ 50 min. In contrast, (left panel) the radar image shows that the "C-shape" structures are westward tilted plasma irregularities. The image was created using aperture systhesis techniques (see *Hysell and Chau* (2006) for a description of the algorithm). Red (blue) shifted echoes denote ascent (descent) drifting.

Incoherent scatter observations of plasma density and drifts made by the

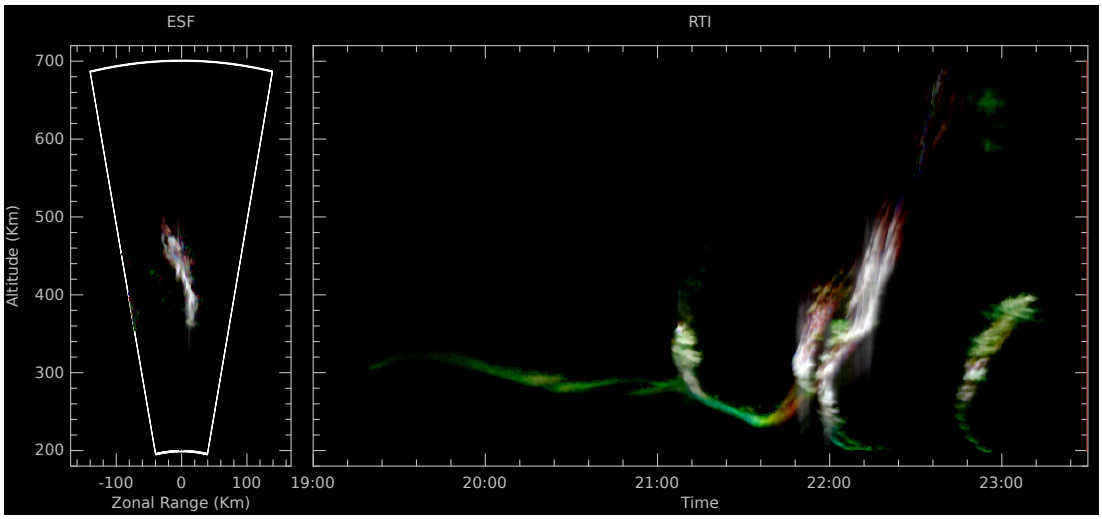

Figure 2.7: Coherent backscatter observations over Jicamarca on October 2, 2010. (Left) Radar image of topside ESF at 22:16 LT. (Right) Range time intensity representation.

Jicamarca radar are shown in Figure 2.8. Electron density measurements (top panel) were not available above 750 km altitude and after 2030 LT. Density observations show the diurnal variation of the *F* peak in the range 300–500 km altitude. At lower altitudes, during daytime, an enhancement in the power was detected due to backscatter from the "150-km echoes". The mechanism behind those echoes is not well understood, but they may be either caused by enhanced ion-line spectra and/or plasma instabilities (*Chau et al.*, 2009). Around sunset, a shear in the zonal plasma flow (bottom panel) is followed by the appearance of plasma irregularities at the shear node. Large zonal electric fields propelled the irregularities upwards due to $\mathbf{E} \times \mathbf{B}$ forcing (middle panel). The plasma depletions are depicted as organized gaps (dark regions) during the post-sunset hours in the velocity maps. The same plasma irregularities were detected at the bottomside of the *F* region in the electron density observations during its first stage; however, due to radar limitations, the method was not able to show the full development of the irregularities.

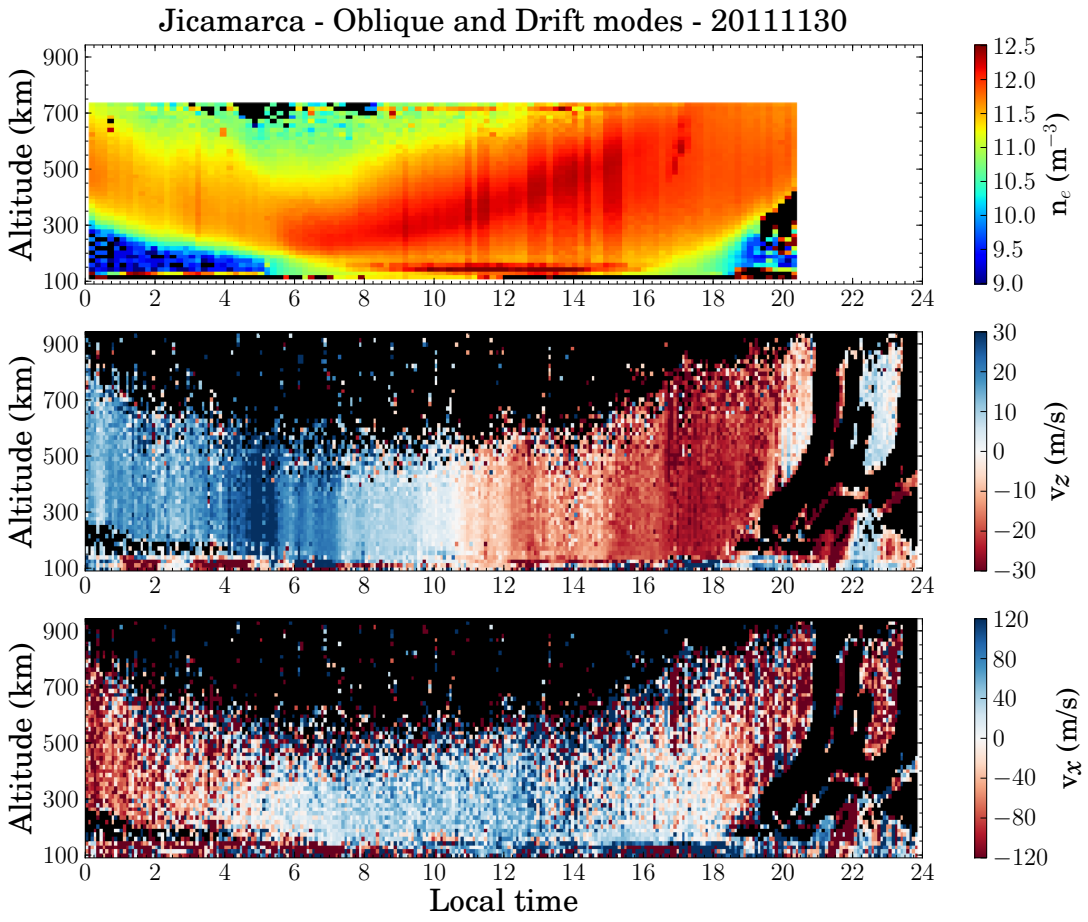

Figure 2.8: Range time intensity representation of incoherent scatter observations over Jicamarca on August 11, 2011. (Top) Electron density (n_e) in log scale of m^{-3}, and (middle) vertical and (bottom) zonal velocities in m/s.

Finally, a keogram of the 6300-Å (or oxygen red) emission on February 17, 2012 is shown in Figure 2.9. The observation was made by an airglow imaging system at the Cerro Tololo InterAmerican Observatory, Chile, looking north (*Makela and Miller*, 2008). A sequence of four plasma depletions were detected in the field-of-view of the camera followed by an enhanced brightness close to local midnight (i.e., 05:00 UT). Bifurcations of the plasma depletions as well as secondary instabilities growing on the walls of the primaries were evident.

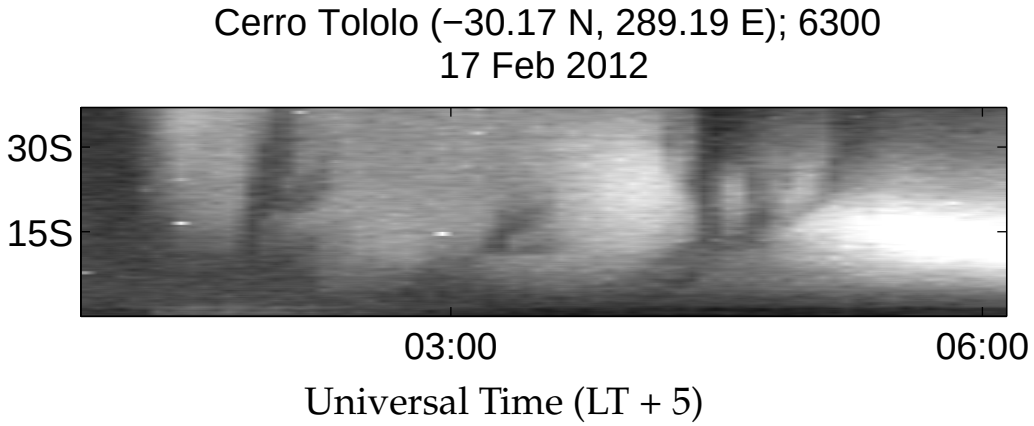

Figure 2.9: Keogram representation of 6300-Å optical data collected by a camera located at the Cerro Tololo Inter-American Observatory, Chile. Courtesy of Jonathan Makela (2012).

CHAPTER 3

FORECAST ASSESSMENT OF TOPSIDE SPREAD *F* AT JICAMARCA

The purpose of computing is insight, not numbers.

–Richard W. Hamming, in *Introduction to Applied Numerical Analysis*

3.1 Introduction

The C/NOFS satellite was launched in April, 2008, to investigate and forecast ambient plasma density and irregularities in the equatorial *F* region ionosphere (*de La Beaujardiere*, 2004, 2009). C/NOFS fostered an explosion in ESF modeling and forecast efforts, including those undertaken here. For C/NOFS-based forecasts to demonstrate skill, they must outperform forecasts based on climatology and persistence alone. A study of ESF using the JULIA radar was described by *Hysell and Burcham* (2002). They analyzed the climatology and persistence of ESF using data gathered between August 1996 and April 2000. The statistics were mainly based on equinox data and did not provide information about seasonal variations. The study presented here expands their previous one. The purpose of this study is to establish the climatology and persistence for one longitude using an extensive radar database.

*This chapter is based on the original published work, *Aveiro and Hysell* (2010*b*). Reproduced by permission of the American Geophysical Union.

3.2 Climatology

Based on the JULIA radar dataset from August, 1996, to May, 2009, the statistics of the different ESF echoes are calculated. To examine the seasonal variation of the statistics, the data were grouped by the following seasonal classification: (1) December solstice, consisting of November, December, January, and February; (2) equinox, consisting of March, April, September, and October; and (3) June solstice, consisting of May, June, July, and August. The solar cycle dependence is based on the 10.7 cm solar flux in three classes: $\phi < 90$ (low solar flux), $90 < \phi < 160$ (moderate solar flux), and $\phi > 160$ (high solar flux). The geomagnetic activity is evaluated using the Kp index averaged over the preceding 6 hours in two levels: Kp<4o for geomagnetically quiet days and Kp≥4o for disturbed days. For post-midnight studies, the analysis is based only on the presence or absence of those echoes, without any further classification. Pre-midnight ESF is classified as bottom-type, bottomside, or topside based on the predominant feature in the JULIA data.

Fig. 3.1a (left) depicts the climatology of pre-midnight spread *F* types versus magnetic activity and solar flux for December solstice (top), equinox (middle), and June solstice (bottom). A remarkable feature is the high occurrence of pre-midnight spread *F* during equinox and December solstice generally, with infrequent occurrence only during the June solstice. Irregularities are extremely common over Jicamarca at all solar flux levels during all seasons except June solstice. More sensitive incoherent scatter experiments indicate, in fact, that nights without irregularities of some kind are extremely rare outside of June solstice. During equinox and December solstice, strong spread *F* events (bottomside or topside) are more common during geomagnetically quiet times. This re-

sult agree with *Chapagain et al.* (2009). Geomagnetic activity generally decreases topside ESF occurrence except at low solar flux outside December solstice.

Fig. 3.1b presents the results of the climatology of post-midnight ESF versus magnetic activity and solar flux for the different seasons. Post-midnight irregularities are most common during low and moderate solar flux conditions (ϕ <160) in all seasons. A positive correlation with geomagnetic activity is observed during solar minimum. This feature was also observed by *Hysell and Burcham* (2002) in a general way, but not according to season and solar flux. A frequent occurrence of post-midnight irregularities during solar minimum years (2008-2009) with no significant correlation with geomagnetic disturbances has been observed by the C/NOFS satellite (*Huang et al.*, 2010). For moderate fluxes, the dependence is almost negligible, and geomagnetic activity seems to be anticorrelated with post-midnight occurrences at higher solar fluxes. The occurrence of post-midnight ESF is higher in December solstice during low solar activity and decreases with increasing solar activity. The same pattern was observed in the Indian sector by *Niranjan et al.* (2003), but the geomagnetic activity dependence was not taken into account in their analysis.

3.3 Persistence

The day-to-day occurrence of topside ESF is poorly correlated with ESF activity two or more days prior (*Hysell and Burcham*, 2002). Using their definition, we therefore define "persistence" as the one day lag correlation. Values approaching +1 indicate a tendency for ionospheric conditions to repeat night-after-night, 0 means no correlation, and -1 indicate a tendency for reversal of conditions.

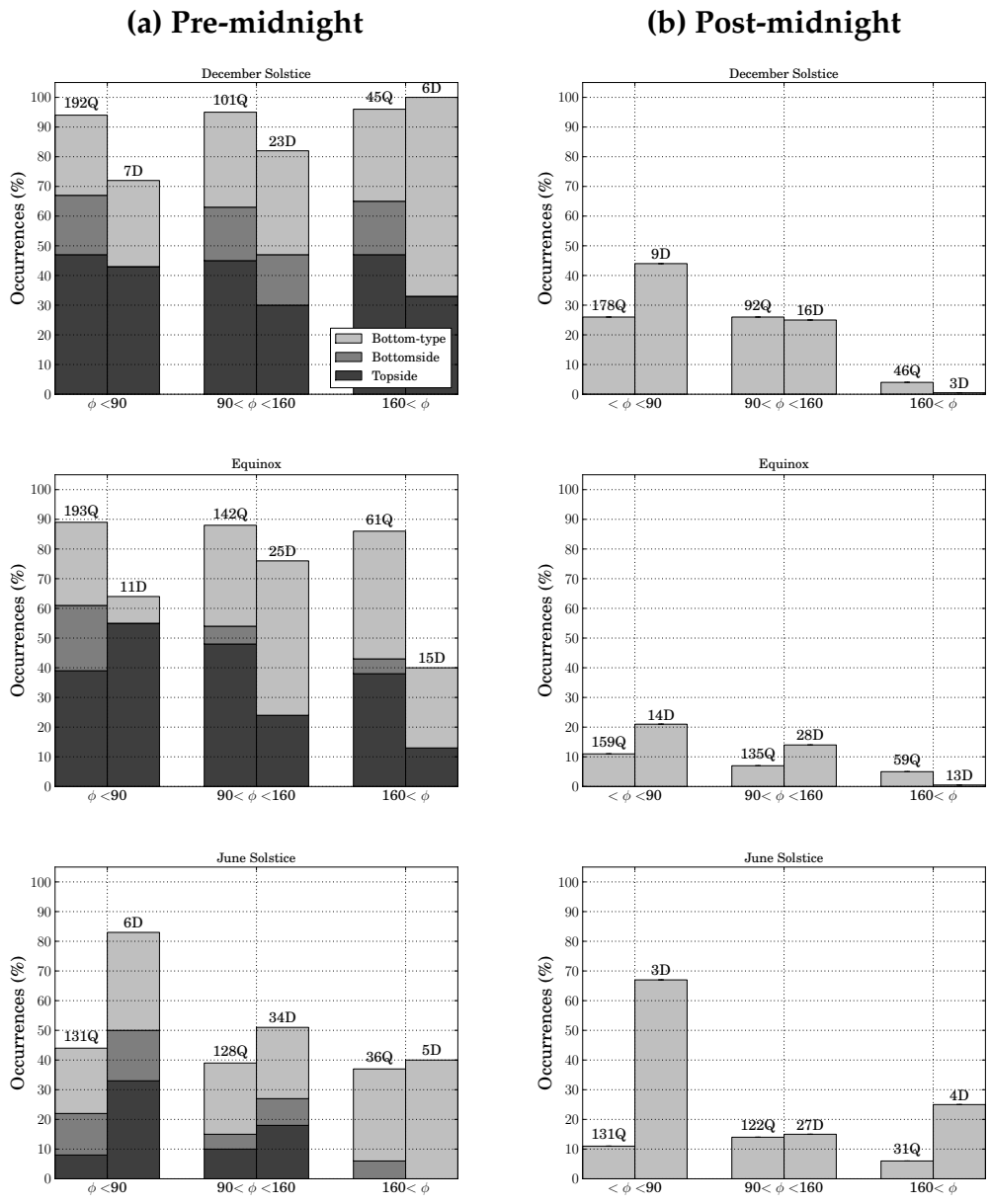

Figure 3.1: Occurrence statistics for (left) postsunset and (right) post-midnight spread *F* echo types versus 10.7 cm solar flux and Kp for (top) December solstice, (middle) equinox, and (bottom) June solstice. The number on the top of the bars are the number of observations followed by a letter: 'Q' for geomagnetic quiet days (left bar) and 'D' for geomagnetic disturbed days (right bar).

Table 3.1: Persistence analysis of pre-midnight topside ESF occurrence

Season	ϕ <90	90< ϕ <160	ϕ >160
Dec. sols.	-0.02 (151)	0.04 (94)	-0.11 (26)
Equinox	0.11 (158)	0.29 (122)	0.19 (55)
June sols.	-0.01 (112)	0.01 (132)	0.00 (28)

Table 3.1 presents the results for pre-midnight topside echo persistence binned by season and solar flux conditions. The values enclosed in parentheses are the number of observation pairs contributing to the persistence computation. Day-to-day occurrences during December and June solstice show little correlation under all solar flux conditions. During equinox, the persistence is higher, approaching 0.3 at moderate solar flux levels. The results for equinox show some discrepancy compared to the *Hysell and Burcham* (2002) analysis which yielded high correlation values. The differences may be attributed to some bias related to the database size, since results similiar to those from *Hysell and Burcham* (2002) were recovered by constraining the analysis to the same dataset (through April 2000 instead of May 2009). Based on the statistics presented here, given a persistence of 0.3 and a mean occurrence rate of 50%, the occurrence of topside ESF will mirror the occurrence of the previous day 65% of the time. Although not shown here, this percentage declines as geomagnetic activity increases.

The same analysis was applied to post-midnight ESF occurrences (Table 3.2). Except for December solstice at solar minimum, the correlation is very low. This indicates that persistence does not provide much useful information for post-midnight ESF forecasting.

Table 3.2: Persistence analysis of post-midnight ESF occurrence

Season	ϕ <90	90< ϕ <160	ϕ >160
Dec. sols.	0.15 (134)	0.09 (71)	-0.01 (26)
Equinox	0.06 (128)	0.01 (116)	0.00 (52)
June sols.	0.07 (107)	0.07 (117)	0.10 (21)

3.4 Lunar effects

The JULIA dataset was next limited to geomagnetically quiet days when Kp was smaller than 4. Using standard techniques and definitions, we compute the correlation between the phase of the moon and topside ESF occurrence. Fig. 3.2 shows the results for pre-midnight and post-midnight irregularities versus solar flux during geomagnetically quiet conditions (Kp<4o). For December solstice during solar maximum: 71% of the "full moon" nights (from first to third quarter) exhibited topside ESF (21 observations) compared to 25% of the "new moon" nights (from third to first quarter, based on 24 observations). At all seasons and solar fluxes other them December solstice during solar maximum, the correlation is negligible.

3.5 Forecasting skill

Using standard statistics, we calculate the mean square error (MSE) between the forecast and observations. Following *Murphy* (1988), a skill score SS based on the mean-squared-error measure of accuracy can be expressed as follows:

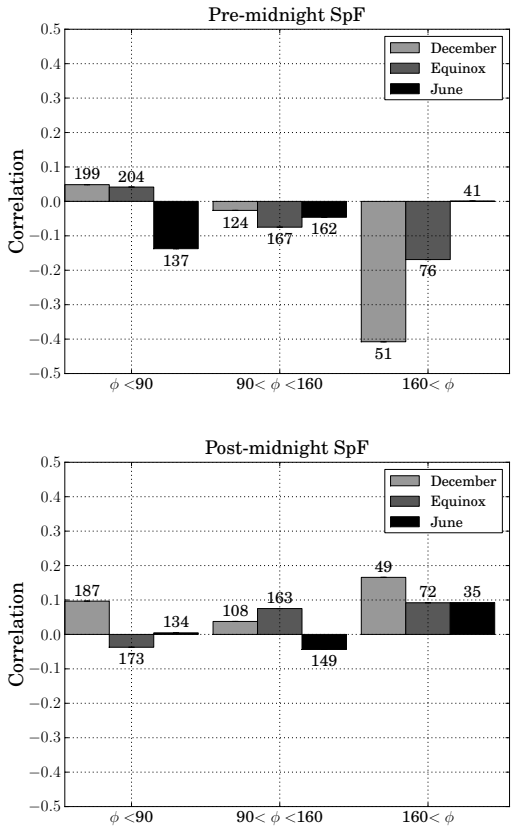

Figure 3.2: Correlation between the phase of the moon and the occurrence of (left) pre-midnight and (right) post-midnight irregularities versus the solar flux. Correlation functions for December solstice (light gray), equinox (dark gray), and June Solstice (black) during geomagnetic quiet conditions (Kp<4o) are shown. The number on the top (or bottom) of the bars are the number of observations.

$$\mathrm{SS} = 1 - \frac{\mathrm{MSE}_{forecast}}{\mathrm{MSE}_{reference}}. \tag{3.1}$$

SS can be interpreted as a measure of percentage improvement in accuracy. The skill score SS is positive (negative) when the accuracy of the forecasts is greater (less) than the accuracy of the reference forecasts. When SS=1 we have a perfect forecast, and SS=0 means that there was no improvement.

Table 3.3: Numerical values of the skill scores of persistence vs. climatology in function of solar flux and geomagnetic activity

	ϕ <90	90< ϕ <160	ϕ >160
Kp<4o	0.06	0.12	0.10
Kp≥4o	0.38	-0.10	0.27

3.5.1 Persistence vs. climatology

As described above, persistence showed negligible values at the solstices. At equinox, however, the persistence is a good candidate as a forecasting tool. In order to evaluate quantivatively, we calculate the SS using the persistence as the forecasting tool and the climatology as a reference. Table 3.3 shows the results. For most conditions, forecasting using persistence shows improvement. The best results are obtained during geomagnetically disturbed periods, with a ~40% improvement at low solar flux.

3.5.2 Lunar phase vs. climatology

The correlation 'R' of the phase of the moon with the occurrences of ESF during solar maximum at Jicamarca can be described by a cosinusoidal function given by $R = -0.42\cos(2\pi\Phi - 0.4)$, where Φ is the phase of the moon (0–new moon, 0.5–full moon, and so on). In the same manner as for persistence, we calculate the SS using the correlation function (adding 0.5 in such a way to have positive probabilities) as the forecasting tool and the climatology as the reference. For solar maximum during geomagnetically quiet periods, information about the phase of the moon gives an improvement of ~17 % over the climatology. We

repeated the calculation for geomagnetically disturbed periods, obtaining ~ -18 %, what means that climatology still yields the best forecasting results for the latter.

3.6 Summary and discussions

This chapter presented the first forecast assessment of equatorial spread *F* over Jicamarca based on JULIA radar data. The climatology, persistence, and the phase of the moon for pre-midnight and post-midnight ESF is analyzed using approximately 1500 nights of the JULIA radar observations.

The climatology reflects a high occurrence of pre-midnight spread *F* during equinox and December solstice generally, with infrequent occurrence only during June solstice. Irregularities are extremely common over Jicamarca at all solar flux levels during all seasons except June solstice. During equinox and December solstice, most strong spread *F* events occurred during geomagnetically quiet times. Geomagnetic activity generally decreases topside ESF occurrence except at low solar flux levels outside December solstice. Post-midnight irregularities are most common during low and moderate solar flux conditions (ϕ <160) in all seasons. A positive correlation between geomagnetic activity and post-midnight occurrences is observed during solar minimum. For moderate fluxes, the dependence is almost negligible, and geomagnetic activity seems to be anticorrelated with post-midnight occurrences at higher solar fluxes. The occurrence of post-midnight ESF is higher in December solstice during low solar activity and decreases with increasing sunspot activity.

During equinox, a day-to-day analysis of ESF events show a high persistence

(1-day correlation). We calculate and evaluate forecasts based on persistence vs. climatology for that season based on the skill score. The results show that the persistence information improves the forecast in relation to the climatology alone, with a ~40% improvement during disturbed periods at low solar flux.

December solstice ESF observations show a high correlation with the lunar phase, with periods close to the full moon presenting the highest probability of ESF occurrence. The lunar semidiurnal tide can affect the amplitude of the pre-reversal enhancement and the time of reversal of the evening upward drifts. Since those parameters play fundamental roles in the generation of spread *F* (*Fejer et al.*, 1999) and the vertical ion drift amplitudes are larger for December solstice months during solar maximum (*Stening and Fejer*, 2001), the results presented here agree with previous observations. Moreover, *Stening et al.* (2002) based on numerical simulations show that the amplitude of the lunar tidal contribution on the H-component of the geomagnetic field is higher during December solstice and increases by a factor of two from solar minimum to maximum. Using this information for geomagnetically quiet periods during December solstice, we calculate the forecasting ability in comparison to the climatology alone. The results show that the information about the phase of the moon improves the forecasting ability in ~17 % when compared to the climatological model.

CHAPTER 4

NUMERICAL SIMULATIONS OF EQUATORIAL *F*-REGION PLASMA IRREGULARITIES: A SINGLE-FLUID MODEL

When you follow two separate chains of thought, Watson, you will find some point of intersection which should approximate the truth.

–Sherlock Holmes, in *The Disappearance of Lady Francis Carfax*
Sir Arthur Conan Doyle

4.1 Introduction

Preceding analyses of the collisional shear instability (see section 2.4) were revealing but insufficiently realistic for definitive conclusions about ESF behavior in nature. They were carried out in either one or two physical dimensions under idealized background conditions in which shear flow was forced rather than generated self consistently. Also, the CSI and gRT instabilities were treated separately and never together. Does the shear flow required by the former stabilize the latter, as linear, nonlocal theory predicts *Guzdar et al.* (1983); *Satyanarayana et al.* (1987); *Hassam* (1992); *Chakrabarti and Lakhina* (2003)? Does the former merely seed the latter? Do the two instabilities act independently, or can emergent phenomena result from their combination?

In this chapter, we undertake a fully three-dimensional numerical analysis of ESF in a realistic background sheared flow. A numerical simulation is developed which is able to reproduce transient and asymptotic growth of CSI as

*This chapter is based on the original published work, *Aveiro and Hysell* (2010*a*). Reproduced by permission of the American Geophysical Union.

well as gRT. The two instabilities are considered first independently and then together. The viability of the coupled system in producing the intermediate- and large-scale plasma density depletions that characterize ESF is then assessed.

4.2 Numerical model

Below, we describe a numerical simulation of plasma instabilities in the post-sunset equatorial ionosphere. The simulation is cast in three spatial dimensions and updates only the plasma density and electrostatic potential in time based on the requirements of quasineutrality and momentum conservation. Inertia is neglected in the present incarnation. The characteristics of the neutral atmosphere are imported from empirical models and remain unchanged during the simulation. The background electric field and neutral wind profile are specified and control the forcing. For the sake of expediency, we assume that the fractional composition of the ions included in the model (O^+, NO^+, and O_2^+) remains invariant, i.e., that the ion mobility at a given point in space is fixed in time. This limitation, as well as the absence of photochemistry, will be rectified in subsequent section of the thesis.

The growth of CSI depends strongly on the height of the vertical shear node and where this falls with respect to the background vertical plasma density gradient. Accurate background configuration and flow modeling in the bottomside and valley regions are therefore essential. The background number density profiles used for initial conditions are meant to reproduce measurements from Jicamarca and ALTAIR, including the F region peak height and peak density, the bottomside density scale height, and the density in the valley region. Accu-

racy is guaranteed by the incorporation of validated empirical model densities (see below). Just as important is the background ionospheric circulation, which is known to be dominated by vortex flow around twilight (*Kudeki and Bhattacharyya*, 1999). That our initial vortex flow, generated self-consistently from initial background conductivity profiles, is a good match for recent sounding rocket electric field measurements argues that the flow regime we are simulating is geophysically representative.

4.2.1 Model description

The simulation algorithm performs two computations. First, the self-consistent electrostatic potential is found by solving Equation 2.10 using the BiConjugate Gradient Stabilized (BiCGSTAB) method (e.g. *van der Vorst* (1992)) using the algorithms described by *Saad* (1990). Under this scheme, the system of equations is preconditioned by an incomplete LU factorization with a dual truncation strategy.

The equation we advance in time is the production- and loss-free version of the continuity equation for the ions (Equation 2.1). Our approach is to solve a discretized version of Eq. 2.1 using a flux assignment scheme based on the total variation diminishing (TVD) condition of *Harten* (1983). This scheme was designed for solving conservation problems with high order accuracy in such a way as to preserve steepened structures while avoiding loss, dispersion, and non-physical oscillation. A pedagogical review and extension of the technique has been published by *Trac and Pen* (2003). That reference describes monotone upwind schemes for conservation laws (MUSCL) directly applicable to the

ion continuity problem. The method we apply combines upward differencing schemes, flux limiting (e.g. *Van-Leer* (1974)), and second order TVD schemes to minimize both diffusion and dispersion in the time advance. The basic method was extended to three dimensions using the dimensional splitting technique of *Strang* (1968). In the simulation runs shown below, we use 2nd order Runge-Kutta time advances with a 10-s step size.

4.2.2 Simulation setup

The model was constructed using tilted magnetic dipole coordinates (p, q, ϕ) as described by *Hysell et al.* (2006*b*). The tilt is matched to the magnetic declination in the zone of interest. In our terminology, p is the McIlwain parameter (L), q is a coordinate parallel to **B** related to magnetic scalar potential, and ϕ is longitude in radians. The simulation is performed on a rectangular grid with respect to these coordinates. Neumann boundary conditions on the electrostatic potential are applied at all the boundaries. At the upper boundary, the normal derivative of the potential is set so as to make the vertical electric field continuous.

Our simulation is cast on a rectangular grid 139×109×189 points wide in (p, q, ϕ) space. A cut through the equatorial plane spans altitudes between 90–510 km and longitudes between ± 10°. The flux tubes covered by the parallel coordinate all reach to the lower *E* region. The runs shown here are centered on the dip equator near Kwajalein (5.5° N latitude, 166.5° E longitude, 7.4° declination). The background conditions are modeled for August 7, 2004, the date of one of the EQUIS II NASA sounding rocket experiments. Geomagnetic conditions were quiet.

The background zonal electric field was taken to be 0.335 mV/m. This corresponds to an F region plasma ascent speed of 10 m/s over Kwajalein. Note that the total ionospheric electric field is this baseline value minus the gradient of the electrostatic potential found through the solution of Eq. 2.10. Local time dependence in the background zonal electric field is neglected in our analyses, which are intended mainly to illustrate model sensitivity to different kinds of drivers.

4.2.3 Empirical model drivers

To initialize the model runs, we derive plasma number densities from the Air Force Research Laboratory Parametrized Ionospheric Model (PIM), a parametrization of the output of several regional theoretical model outputs generated for different climatological conditions and tuned somewhat to agree with data from Jicamarca and elsewhere (*Daniell et al.*, 1995).

Plasma mobilities are calculated using neutral composition and temperature estimates from the Mass Spectrometer and Incoherent Scatter (MSISE90) model (*Hedin*, 1991) and ionospheric composition estimates from the International Reference Ionosphere (IRI2003) model (*Bilitza*, 2000). We take the ionosphere and neutral atmosphere to be in thermodynamic equilibrium after sunset. Atomic (O^+) and molecular (NO^+ and O_2^+) are included in the model, but light ions are not. For our runs, the zonal neutral winds are based on profiles measured during the EQUIS II sounding rocket campaign between 100–150 km. Lacking wind measurements above 150 km, we make use of the Horizontal Wind Model (HWM) (*Hedin et al.*, 1996) above 200 km altitude. Between 150 and 200 km,

the wind profiles are joined smoothly by a continuous function. The winds are presently taken to be functions of altitude only. Only the zonal neutral winds are considered. At present, we regard the background zonal electric field and the neutral wind profiles as drivers with which to experiment.

4.2.4 Initialization

Fig. 4.1 shows representative diagnostic information at the start of a simulation run. The top panel of Fig. 4.1 shows the background plasma number density near twilight. This initial condition is consistent with ALTAIR radar observations during EQUIS II. To seed the simulation run, we add independent Gaussian white noise to the initial number density with a 20% relative amplitude. This is meant to reflect the presence of baseline background variability.

The middle panel of Fig. 4.1 shows the zonal current density with equipotential contours superimposed. According to the legend shown, the *F* region current density is significant and mainly upward. This current is driven by the *F* region dynamo, which is limited in efficiency by conductive loading in the *E* and valley regions. Solenoidal current density is maintained in part through the production of shear flow, as indicated by the curved equipotentials and the emergent vortex, and in part by parallel currents. The vertical electric field profile shown to the right is a good match for conditions found during EQUIS II.

Finally, the bottom panel shows the meridional current density. Here, horizontal lines represent individual field lines, and a surface of constant altitude is a U-shaped arc. The raggedness is a consequence of the seed noise added. The figure shows equatorward current flowing in the bottomside region and pole-

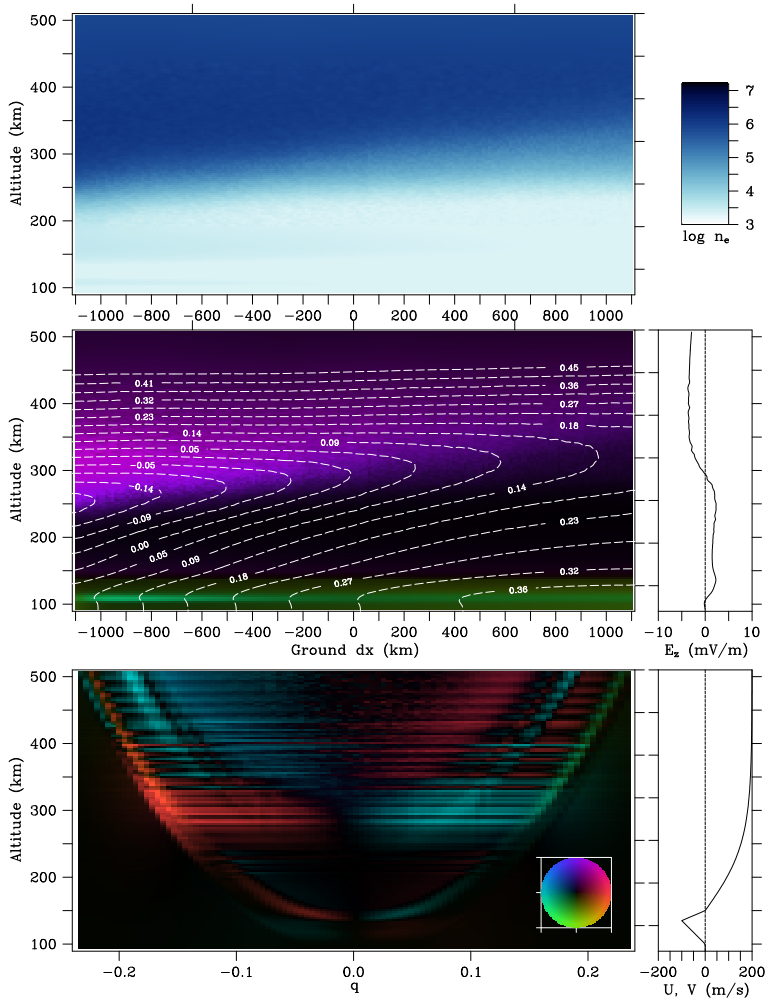

Figure 4.1: Representative initial conditions for our model runs. (top panel) Plasma number density ($\log_{10} n_e$ (cm^{-3})) in a cut through the equatorial plane. The axes span longitudes between ± 10° and altitudes between 90–510 km. (middle panel) Transverse current density and electrostatic equipotentials in kV. The current density scale maximum is 20 $\mu a/m^2$. The vertical electric field profile at the horizontal center of the simulation space is plotted to the right. (bottom panel) Parallel current density in the plane of the magnetic meridian. The current density scale maximum is 200 $\mu a/m^2$. The current density legend is given by the colored disk. The zonal wind profile is plotted to the right.

ward current flowing in the *F* region. These currents attach to the upward currents in the middle panel to satisfy the demands of quasineutrality. The zonal wind profile shown to the right of the bottom panel is the best estimate of the winds available during the EQUIS II experiment.

4.3 Model results

Here, we present results from simulation runs designed to contrast the behavior of the gRT and CSI instabilities and to examine if and how the act as a system to produce plasma irregularities found in ESF. Three runs are described. For the first, the neutral winds are switched off entirely. This suppresses shear flow, inhibits CSI, and permits only gRT to function. The behavior thus produced is found to be essentially identical to that found in previous studies such as *Zargham and Seyler* (1987). For the second, the background electric field and gravity are switched off, and the zonal neutral wind is switched on. This time, the gRT instability is suppressed, shear flow emerges, and the CSI is activated. The behavior we find here is similar to that presented by *Hysell and Kudeki* (2004), except now under much more realistic and self-consistent conditions. Finally, the winds, the background electric field, and gravity are all present in the third run, which is designed to represent the post-sunset ionosphere comprehensively.

Results for the simulation run with the neutral winds set to zero are shown in Fig. 4.2. For these runs, the background zonal electric field, which we take to be imposed from outside by the Sq current system, is held constant and fixed at 0.335 mV/m. This electric field is comparable to gravity in its ability to drive the

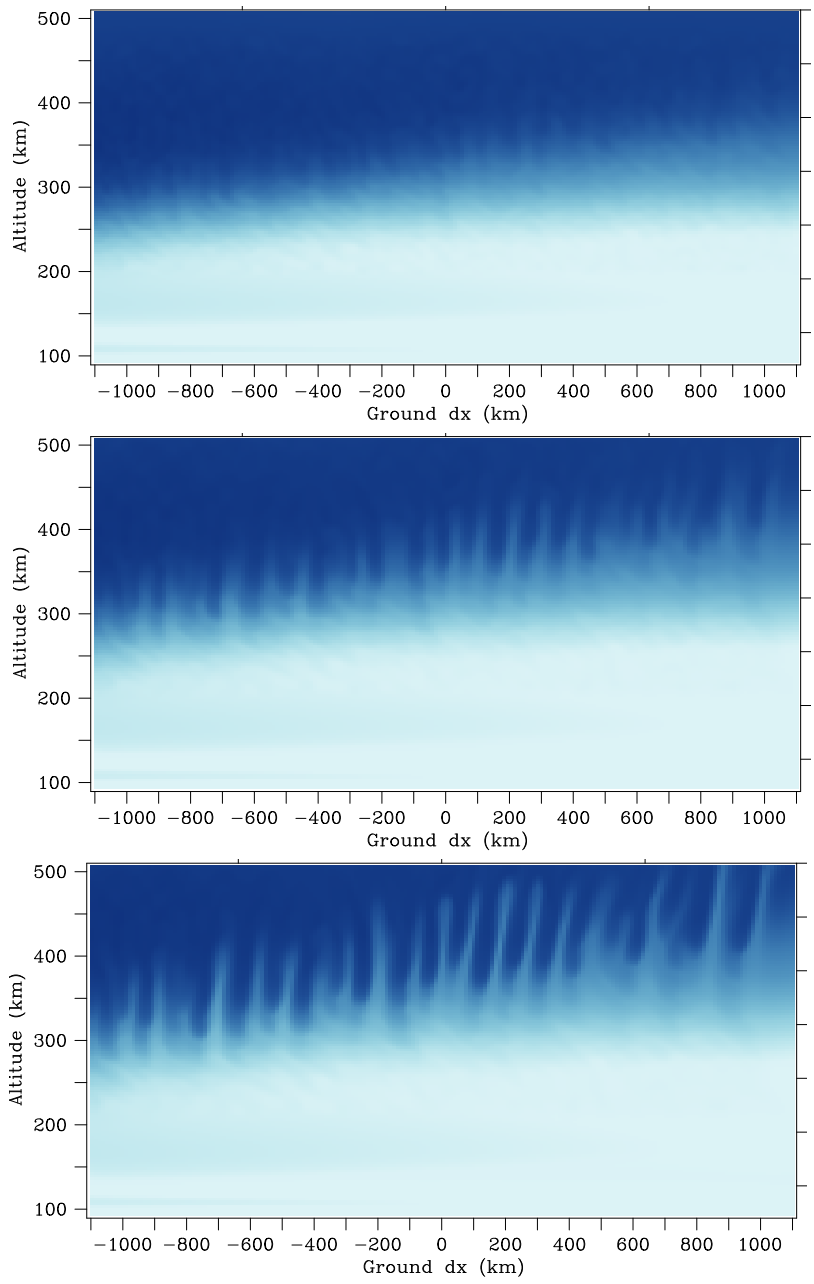

Figure 4.2: Simulated plasma densities in the equatorial plane for the case where the neutral wind is fixed at zero. The three panels show results for simulation times of 30, 60, and 85 min., respectively, after a start at $t_\circ$ = 8:45 UT (LT = UT + 11 hr at the horizontal center of the simulation).

gRT instability in the bottomside region, while gravity becomes the dominant driver near and above the *F* peak.

Fig. 4.2 depicts the well-known characteristics of a developing gRT or collisional regime ionospheric interchange instability. The waveforms that emerge are highly regular, laminar, and anisotropic (columnated). They do not appear to be very turbulent. The main action of the nonlinearity in the system is to produce highly steepened structures at the leading edges of the enhancements and depletions. The depletions and enhancements themselves are asymmetric, with depletions being narrower and moving faster with respect to the background plasma than the enhancements. Some ballooning of the depletions can be seen where they encounter the *F* peak. Bifurcation is evident in some of the waveforms. The gRT instability does not saturate but instead grows until the background vertical density gradient is restored to equilibrium, the excess free energy having been shifted to large wavenumbers via plasma steepening and there dissipated.

gRT is a universal instability, being linearly unstable at horizontal wavelengths from about 1 km, where it is diffusively damped in nature, to over 100 km, where the finite vertical density gradient extent suppresses the instability nonlocally (*Zargham and Seyler*, 1987). In these simulations, the horizontal resolution between neighboring cells is about 15 km, implying the possibility of simulating waves with 30 km or longer horizontal wavelengths. In practice, finite numerical diffusivity (lossiness) increases the minimum resolvable wavelength. The waveforms in Fig. 4.2 exhibit a wavelength of about 75 km, which persists from start to end of the simulation. This figure represents the effective minimum wavelength accessible to the simulation.

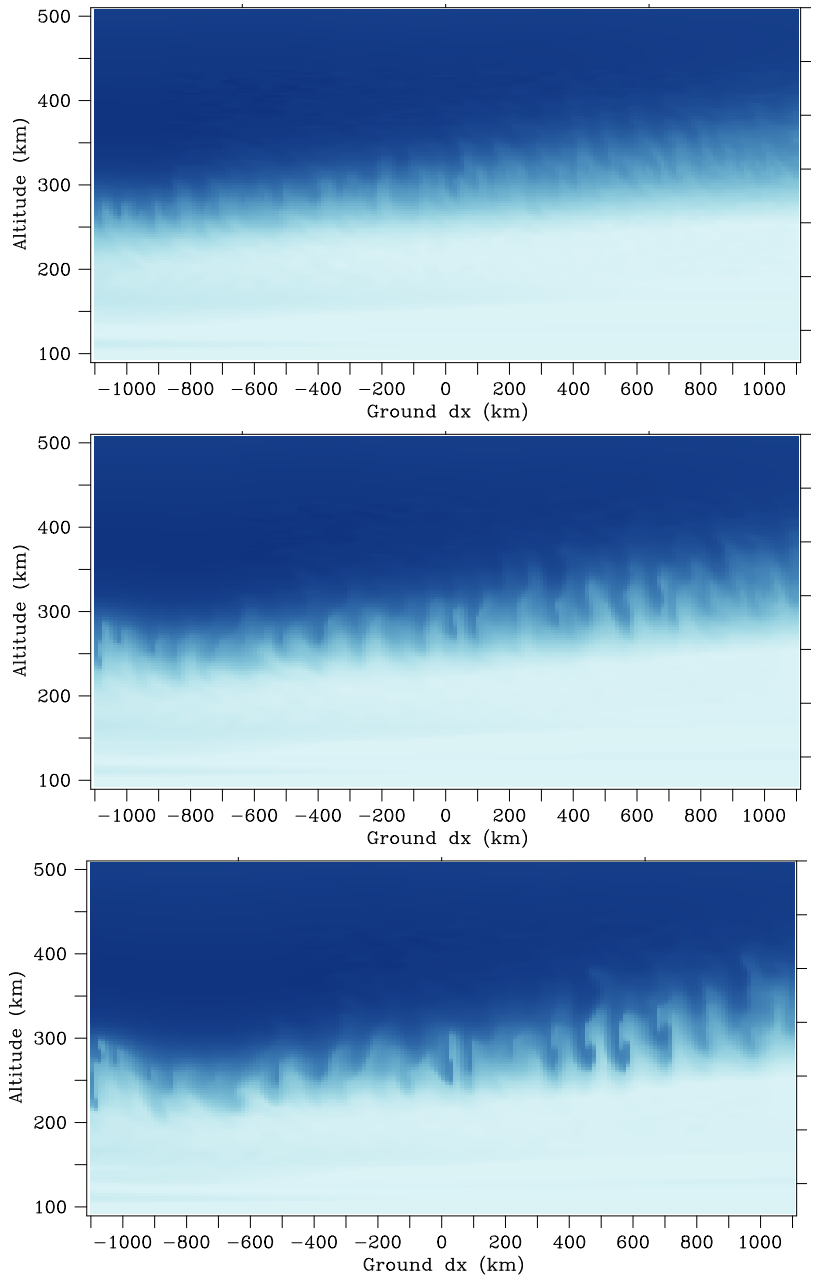

Figure 4.3: Simulated plasma densities in the equatorial plane for the case where the neutral wind is restored but the background zonal electric field and gravity are set to zero. The three panels show results for simulation times of 30, 60, and 85 min., respectively, after a start at $t_\circ$ = 8:45 UT (LT = UT + 11 hr at the horizontal center of the simulation).

Fig. 4.3 shows model runs where the zonal neutral wind is fixed according to the profile shown in Fig. 4.1 but the zonal electric field and gravity are both set to zero. The gRT is completely stable in this situation, and so the absence of irregularities might be expected. Like *Hysell and Kudeki* (2004) and *Kudeki et al.* (2007), however, we find that the sheared flow and, more specifically, the vertical current density and retrograde bottomside plasma drifts in evidence in Fig. 4.1, are ingredients for instability and rapid wave growth.

We quantify the instability growth rate below. Here, we note that the waveforms emerging after 30 min. in the CSI simulation in Fig. 4.3 are much more distinct and have larger relative amplitudes then those in the gRT simulation in Fig. 4.2. The CSI waveforms also differ in their altitude range and extent. Whereas the waves in Fig. 4.2 emerge in the bottomside and then extend into the *F* peak, the waves in Fig. 4.3 emerge and largely remain at the base of the bottomside, extending slightly into the valley. Whereas the linear growth rate of gRT maximizes essentially where the vertical density gradient scale length is shortest, the linear growth rate of CSI is also influenced by the speed of the retrograde plasma drifts, which has a maximum in the valley.

Although the waveforms in Fig. 4.3 emerge rapidly, they do not experience much vertical development and remain confined in altitude to the zone where retrograde plasma drifts exist. At 30 min., the first waveforms visible are clearly tilted, with depletions (enhancements) directed upward and westward (downward and eastward). The tilt is approximately one part in five, which is nearly the ratio of the horizontal to the vertical extent of the simulation space, measured in kilometers. Waveforms tilted at approximately 45° to the vertical is an important characteristic of the CSI. Over time, the tilt becomes less prevalent.

Given enough time, the tilted waveforms evolve into rolls that are reminiscent of Kelvin-Helmholtz rolls. This can be seen in the simulation results at 90 min. The resemblance arises from the similar objectives of Kelvin-Helmholtz and CSI, which is to mix stratified material and momentum.

At 30 min., the dominant horizontal wavelength of the waves is about 75 km. As before, this likely represents the minimum achievable wavelength for this simulation. However, as time progresses, the waveforms compete, with weaker waveforms absorbed into stronger ones. By the 90 min. timestep, the dominant horizontal wavelength has approximately doubled. This progression represents the disappearance of the initial transient response of the instability and the onset of the steady-state response, with a wavelength close to that predicted by normal mode analysis. Similar behavior was not evident in Fig. 4.2.

The most realistic simulation of the three is shown in Fig. 4.4, which predicts the outcome when the zonal neutral wind, zonal electric field, and gravity are all in place. The outcome appears to be essentially different from either the gRT or the CSI acting separately. While the morphology of the waveforms produced in the first 30 min. of the simulation is similar to the CSI, the relative amplitude of the waves is significantly larger by that time. Vertical development proceeds rapidly thereafter, with depletions reaching the *F* peak and enhancements reaching into the valley by the 60 min. mark. By this time, the relative density perturbation amplitude is nearly 100%. Secondary wind-driven instabilities can be seen to be contributing structure to the westward walls of the largest depletions, while the eastward walls appear to be steepening.

By 85 min., the *F* region is inundated with structure spanning nearly all altitudes and scale sizes present within the system. Some depletions have pene-

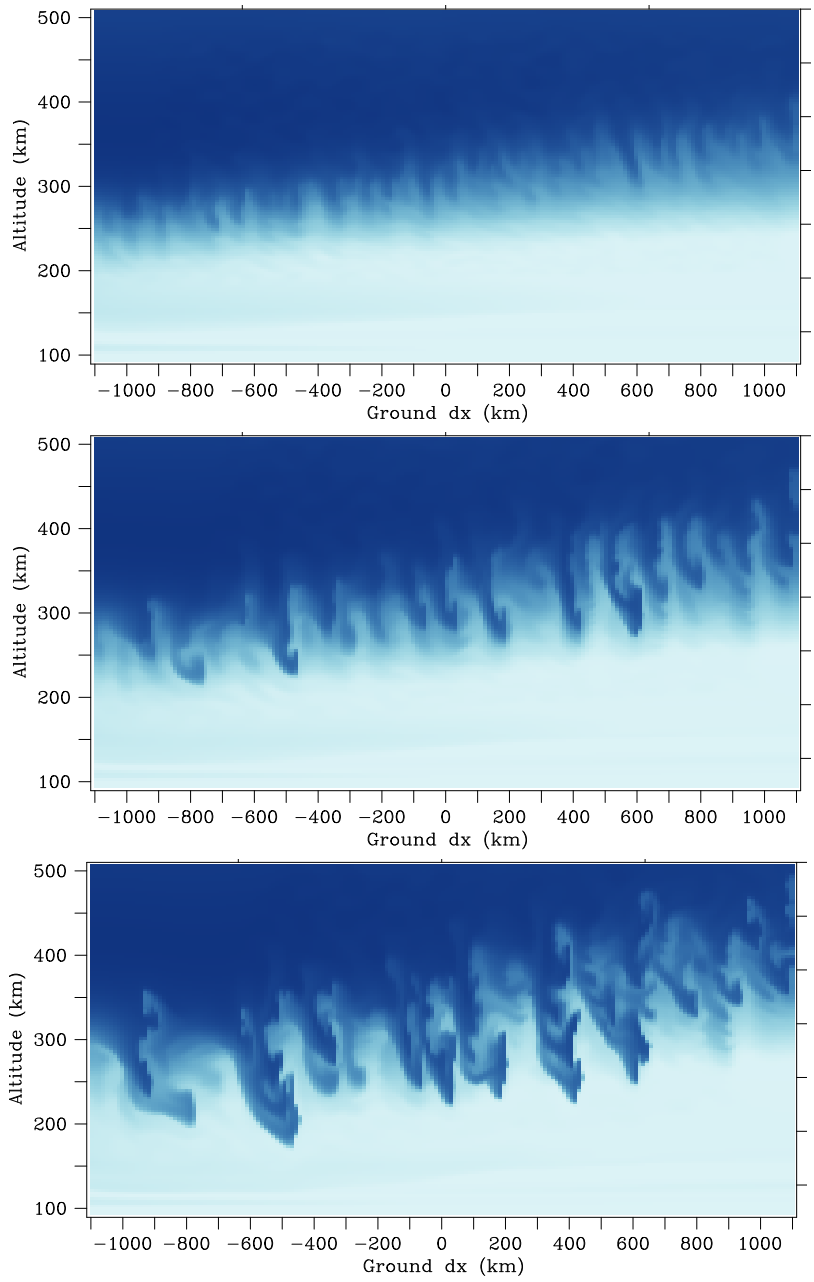

Figure 4.4: Simulated plasma densities in the equatorial plane for the case where the zonal neutral wind, zonal electric field, and gravity are all resent. The three panels show results for simulation times of 30, 60, and 85 min., respectively, after a start at $t_\circ$ = 8:45 UT (LT = UT + 11 hr at the horizontal center of the simulation).

trated the F peak, moved into the topside, and encountered the upper boundary of the simulation (although these have mainly drifted out of the simulation space by timestep 85). Some roll-like features have emerged at low altitudes, although these are obscured by secondary instabilities and not really a salient feature of the resulting morphology. While the inter-waveform spacing at 30 min. was once again about 75 km, that figure has increased to about 200 km by 85 min., as smaller waveforms are incorporated into larger ones. The end result is a series of wedge-shaped, westward-tilting depletions separated by ~200 km+ distances and penetrating into the topside. The drastic redistribution of plasma by this time has altered the background circulation in such a way that the irregularities all drift eastward together.

4.3.1 Energy analysis

An ideal invariant of the simulation (in the limit of no dissipation) is the total scalar variance, which can be expressed in terms of the sum of the density Fourier modes $I = \sum_k |n(\mathbf{k})/n(0)|^2$ (see e.g. *Zargham and Seyler* (1987).) At the start of the simulation, the modes contributing to I are concentrated at small wavenumbers and constitute the background density configuration. Instability-driven waves act to remove free energy from the background and redistribute it to higher wavenumbers. Eventually, diffusive dissipation evacuates high wavenumbers, returning scalar variance to the origin. A metric describing the energy in the waves at a given time is I calculated with contributions near the origin excluded. Fig. 4.5 shows wave energy versus time calculated this way for the three simulation runs. (Wavenumbers in an solid elliptical region centered on the origin and with a semininor (semimajor) width of $2\pi/280$ km^{-1} ($2\pi/100$

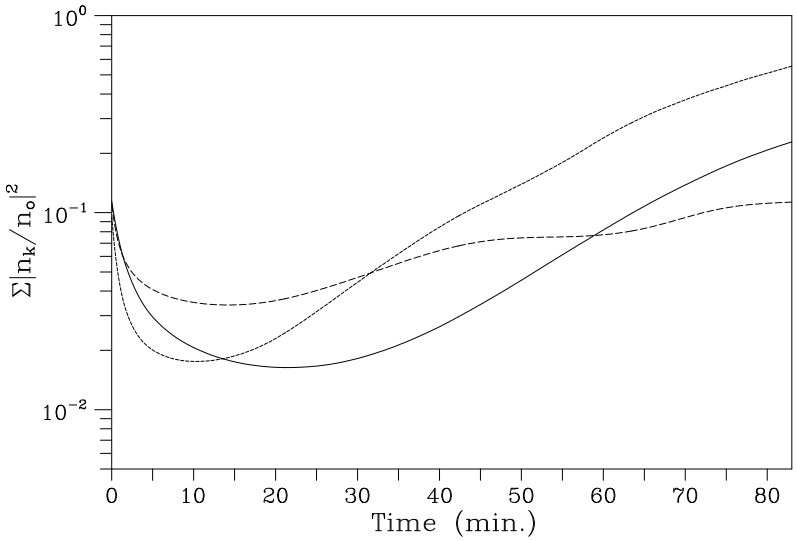

Figure 4.5: Wave energy versus time for the three simulation runs. The solid, long dashed, and dashed lines represent the gRT, CSI, and combined instability runs (see text).)

km^{-1}) in the zonal (radial) direction were excluded in calculating *I* here.) For the first few minutes of each run, most energy shown is contained mostly in the random density perturbations used to seed instability.

The solid curve in Fig. 4.5 shows the wave energy for the gRT. After about 20 min., the energy in the initial random perturbations has been dissipated, and it becomes possible to distinguish energy accumulating in the primary wave modes. Wave growth is almost linear throughout the simulation. The e-folding time for the instability amplitude is about 30 min. *Zargham and Seyler* (1987) showed that the gRT does not saturate but continues to grow until the free energy in the background density gradient is extinguished. That begins to happen in simulation after about 60 min.

The long dashed line in Fig. 4.5 shows the results for the CSI. In the pure

CSI case, the rapid initial, transient growth of the waves is concealed by the concurrent decay of the energy in the initial perturbations. The configuration-space simulation results in Fig. 4.3 show how the random initial perturbations are replaced by fast-growing coherent waveform, but that information is lost in the energy metric. The CSI energy saturates early in the simulation and is matched by that of the gRT after about 60 min. The altitudinal confinement of the instability plays a role in the early saturation.

Finally, the dashed line in Fig. 4.5 shows the results of the combined simulation. Linear wave growth is discernable after about 20 min., when the e-folding time of the waves is about 20 min. The wave energy overtakes that of the pure CSI instability after about 30 min., and the instability does not experience the low-amplitude saturation inherent in CSI. By 40 min., the growth rate of the instability approximately matches that of gRT. By that time, however, the energy advantage over gRT is nearly an order of magnitude. The advantage is nearly maintained until the end of the simulation. By that time, the relative density perturbation amplitude for the combined instability is close to 100%.

The combined instability shares attributes of CSI, which can act at low altitudes in the valley region, and gRT, which can act at high altitudes, near the *F* peak. The mixing depth of the combined instability is therefore extensive, and so its ability to generate large-amplitude density fluctuations exceeds that of either CSI or gRT acting alone. This is ultimately what makes it possible for the post-sunset *F* region ionosphere to become deeply mixed 60–90 min. after the onset of instability.

4.4 Summary and discussions

Previous studies have considered the viability of the collisional shear instability acting by itself in the post-sunset equatorial F region ionosphere using eigenvalue analysis, linear initial value analysis in one dimension, and nonlinear initial value analysis in two dimensions. These predicted a rapid, transient response at wavelengths comparable to a few times L (the vertical density gradient scale length) and a somewhat more slowly growing steady-state waves with wavelengths of the order of $4\pi L$ with a linear growth rate still several times that of the Generalized Rayleigh-Taylor instability.

With this study, we have reproduced the earlier results using a fully three-dimensional nonlinear initial value numerical approach and and gone on to evaluate how the two instabilities might function together in nature. The CSI appears neither to suppress gRT nor to simply seed it. Instead, the combined instability grows and develops faster than either acting alone, exhibits a greater mixing depth, and produces apparently emergent phenomena in its morphology and evolution. Simulated waveforms are rather similar to those observed with incoherent scatter radar, both in terms of their gross morphology and rates of development. Furthermore, the CSI seems to be able to account for bottom-type and bottomside layers, common equatorial ionospheric phenomena associated with ESF but not usually addressed in theoretical and modeling studies. That the CSI requires vertical F region currents to function suggests that an imperfectly efficient F region dynamo may actually enhance ionospheric instability (within limits).

Our simulations using background conditions consistent with sounding

rocket data at a start time corresponding to the rocket flight time. White noise was used as a seed. Outstanding questions in this discipline include the actual starting time for the instabilities that produce ESF, the appropriate parametrization for the irregularity seed, and the source of the underlying geophysical variability. Additional satellite and sounding rocket data acquired prior to the onset of ESF are required to address these questions. Specification of the initial plasma density profile, zonal electric field, and neutral wind profile throughout the evolution of ESF meanwhile appears to be crucial for predicting how gRT and CSI will interact and develop.

CHAPTER 5

NUMERICAL SIMULATIONS OF EQUATORIAL SPREAD *F*: RESULTS AND OBSERVATIONS IN THE PACIFIC SECTOR

It doesn't matter how beautiful your theory is, it doesn't matter how smart you are. If it doesn't agree with experiment, it's wrong.

–Richard P. Feynman, in *Surely You're Joking, Mr. Feynman!*

5.1 Introduction

The numerical simulations developed in Chapter 4 incorporated a number of non-essential simplifications. The model included time-invariant neutral atmosphere and background forcing. Also, the simulations were based on a single ion fluid model which did not take recombination into account. Here, we present the results of a multi-ion simulation which includes recombination, Coulomb collisions, a time-varying neutral atmosphere, and variable forcing, inferred from data from the C/NOFS satellite. The results are compared to incoherent scatter radar observations made by the ALTAIR radar in the Pacific sector.

Key attributes of our simulation included (a) its sensitivity to the background circulation, (b) its sensitivity to event sequencing, and (c) its inclusion of parallel electric fields. The main issue we address below is the degree to which it is possible to predict, quantitatively, the behavior of ESF given an appropriate specification of the initial conditions and the forcing.

*This chapter is based on the original published work, *Aveiro et al.* (2012). Reproduced by permission of the American Geophysical Union.

5.2 Radar observations

We begin with a presentation of the radar observations that will ultimately be used to motivate and validate the numerical simulations. The ARPA Long-Range Tracking and Instrumentation Radar (ALTAIR) is a VHF/UHF radar located at Kwajalein Atoll (8.8°N, 167.5°E) (*Tsunoda et al.*, 1979). Figure 5.1 displays ALTAIR UHF (422 MHz) data for the night of April 29, 2009. ALTAIR observations made perpendicular to the geomagnetic field at *F* region heights represent a combination of coherent and incoherent scatter, whereas off-perpendicular scans reflect only incoherent scatter. Some coherent scatter can be informative in datasets like these because it highlights fine structure that might otherwise be difficult to perceive.

The top panel of Figure 5.1 shows an ALTAIR scan made pointing perpendicular to the geomagnetic field around 09:45 UT (LT ≈UT+11 hr in the radar longitudinal sector). By this time, irregularities had formed at the base of the *F* region as bottom-type layers. These were patchy and spaced by about 35 km. They are common precursors of fully-developed ESF, whereas bottom-type layers tend to be more continuous (beam-filling) or absent on nights when topside ESF does not develop (*Hysell et al.*, 2004).

ALTAIR scans made pointing off-perpendicular to the geomagnetic field at 10:30 UT and 11:26 UT are shown in the middle and bottom panels of Figure 5.1, respectively. By about 10:30 UT, the irregularities were still confined to the base of the *F* region, but the predominant horizontal scale had increased to 100-200 km. Between about 10:30 and 11:26 UT, the bottomside depletions underwent strong vertical development. Depleted channels penetrated to the topside while

retaining their 100-200 km horizontal spacing. The depletions had characteristic tilts and showed evidence of bifurcation and secondary instabilities. Wedges of enhanced plasma also appeared to be driven downward in between ascending depletions.

5.3 Satellite observations

To drive simulations of the April 29, 2009 ESF event, *in situ* electric field measurements from the Ion Velocity Meter (IVM) and Vector Electric Field Instrument (VEFI) on board the Communications/Navigation Outage Forecasting System (C/NOFS) satellite were used. This satellite was launched in April, 2008, to investigate and forecast ambient plasma density and irregularities in the equatorial *F* region ionosphere (*de La Beaujardiere*, 2004). IVM is comprised of an ion drift meter and an ion-retarding potential analyzer that together provide measurements of the ion drift vector, the ion temperature, and the major ion composition. The VEFI instrument consists of an electric field meter, a fluxgate magnetometer, an optical lightning detector, and a fixed-bias Langmuir probe. Among its products are measurements of DC, quasi-DC, and AC electric fields.

Figure 5.2 shows the zonal electric field (based on IVM ion drift and VEFI magnetometer measurements) and (IVM) ion density measurements with the respective orbital information tabulated below (geographic and magnetic coordinates, altitude, and universal and solar local times). The results correspond to C/NOFS passes during the post-sunset period on April 29, 2009, centered at the Kwajalein longitudinal sector. For comparison, satellite passes at (top pan-

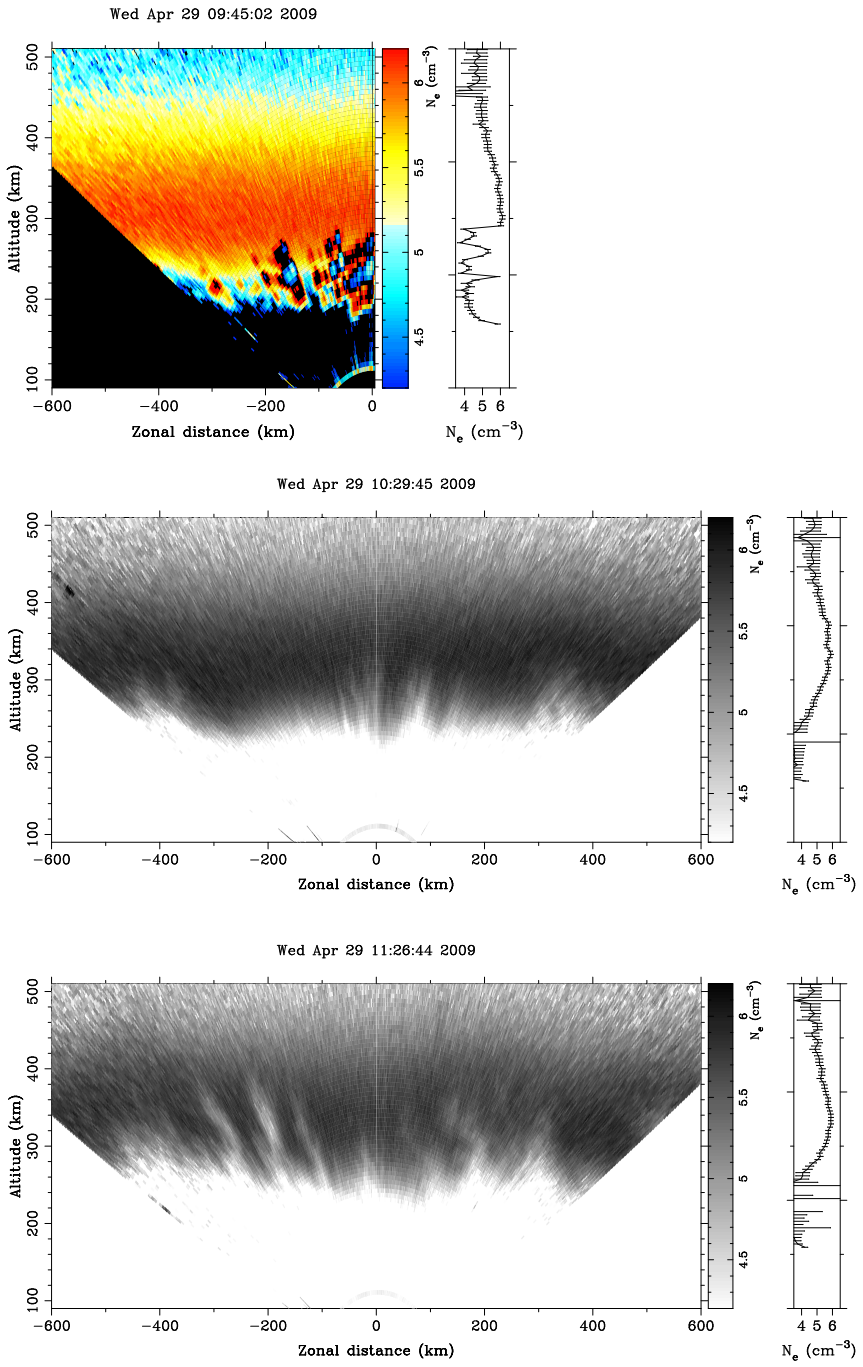

Figure 5.1: ALTAIR radar scans for April 29, 2009, showing backscatter power, range corrected and scaled to electron density on a logarithmic scale: (top) perpendicular scan at 09:45 UT, off-perpendicular scans at (middle) 10:30 UT and (bottom) 11:26 UT. The rightmost panels depict vertical electron density profiles. Note that LT ≈ UT + 11 hr.

els) ~ 09:03 UT, (middle panels) ~ 10:47 UT and (bottom panels) ~ 12:31 UT are shown.

During the first C/NOFS pass at about 09:03 UT, the zonal electric field was essentially zero, and no density or electric field perturbations were detected in the altitude range between 495-520 km. By the time of the next pass at about 10:47 UT, the zonal electric field had increased to 0.5-0.75 mV/m, and small electric field irregularities were emerging between 435-450 km altitude. That the background plasma density increased as the satellite altitude decreased suggests that it was flying in the topside, which is consistent with the evidence of Figure 5.1.

By the time the satellite passed through the Kwajalein sector again at about 12:30 UT, the electric field irregularities had become large (up to about 4 mV/m). Modest plasma density irregularities were also present at altitudes near 400 km. In view of Figure 5.1, however, the satellite most likely flew just above the most intense plasma density irregularities.

5.4 Numerical model

Below, we describe a numerical scheme for the simulation of the plasma density irregularities in the equatorial spread *F* event. The 3-D simulation updates the plasma density and electrostatic potential in time assuming quasineutrality (Equation 2.1) and momentum balance (Equation 2.2). Equation 2.1 is not in conservation form, since it includes chemical processes. However, it can be converted to conservative form through variable transformation. Two simplifications are applied to Equation 2.1 and Equation 2.2: (a) the neglect of diag-

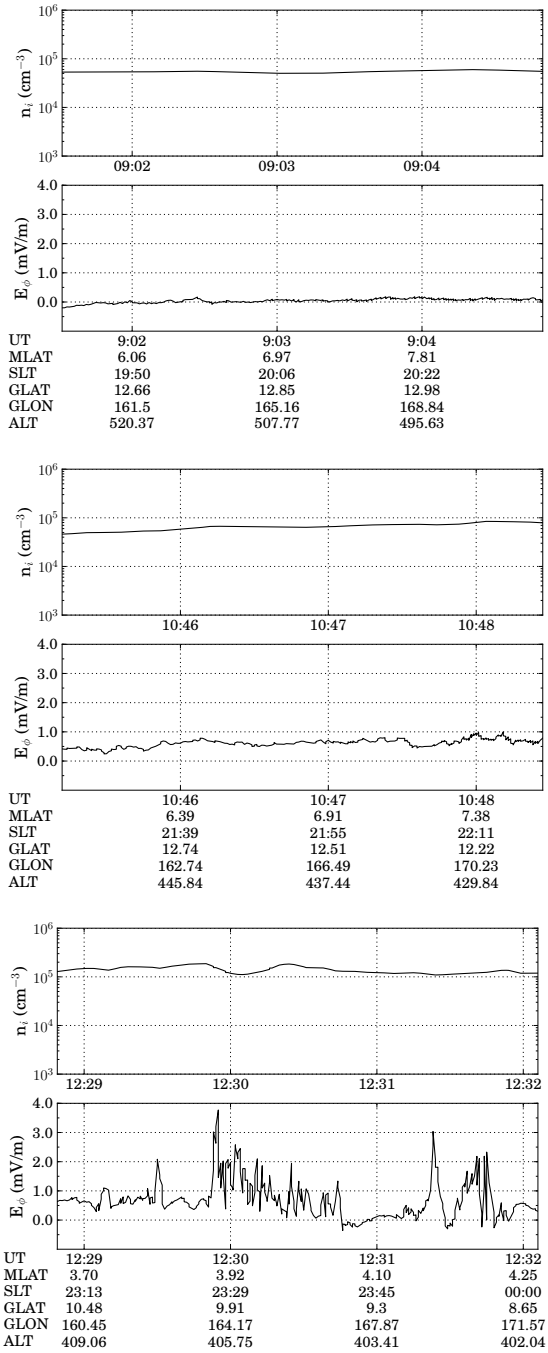

Figure 5.2: Ion density (cm^{-3}) and zonal electric field (mV/m) at three different passes through the Kwajalein sector: (top panel) ~ 0903 UT, (middle panel) ~ 1047 UT, and (bottom panel) ~ 1230 UT. The tabulated entries are universal time (UT), magnetic latitude (MLAT), solar local time (SLT), geographic latitude (GLAT), longitude (GLON), and altitude (ALT) in km.

magnetic drifts ($\nabla n_\alpha \times \mathbf{B}$), since their associated flux divergence is very small when compared to the other terms, and (b) Coulomb collisions (the last term in the RHS of Equation 2) are treated implicitly and only included in the parallel direction.

The simulation algorithm performs two computations. First, the self-consistent electric field is found using a 3-D potential solver (Equation 2.9). Second, we solve a discretized version of Equation 2.1 for each ion species using a monotone upwind scheme for conservation laws (MUSCL) (a pedagogical review can be found in *Trac and Pen* (2003)). The characteristic of the neutral atmosphere (densities, temperature, and wind velocity) are updated in time on the basis of inputs from climatological models. The background electric field is specified and partly controls the forcing. The ion composition includes O^+, NO^+, and O_2^+. The model was constructed using tilted magnetic dipole coordinates (p, q, ϕ), where the tilt is matched to the magnetic declination in the longitude of interest. In our terminology, p represents the McIlwain parameter (L), q is the magnetic co-latitude, and ϕ is longitude (see e.g., *Hysell et al.* (2004)).

5.4.1 Empirical model drivers

To initialize the model runs, we derive plasma number densities from the Parametrized Ionospheric Model (PIM), a parametrization of the output of several regional theoretical model outputs generated for different climatological conditions and tuned somewhat to agree with data from Jicamarca and elsewhere (*Daniell et al.*, 1995). PIM reproduces electron density profiles from Kwajalein and Jicamarca fairly closely if scaled slightly to account for day-to-day

variability (*Aveiro and Hysell*, 2010*a*). The background number density profiles used for initial conditions are intended to reproduce measurements from ALTAIR, including the *F* region peak height and peak density, the bottomside density scale height, and the density in the valley region.

Plasma mobilities are calculated using neutral composition and temperature estimates from the Mass Spectrometer and Incoherent Scatter (NRL-MSISE00) model (*Picone et al.*, 2002) and ionospheric composition estimates from the International Reference Ionosphere (IRI-2007) model (*Bilitza and Reinisch*, 2008). We take the ionosphere and neutral atmosphere to be in thermodynamic equilibrium after sunset ($T_n = T_e = T_i$). Expressions for the ion-neutral and electron-neutral collision frequencies used to compute conductivities can be taken from *Richmond* (1972). For our runs, the zonal neutral winds are obtained from the Horizontal Wind Model (HWM-07) (*Drob*, 2008). As with PIM, these may be tuned slightly to account for day-to-day variability. The model is sensitive to the wind speeds throughout the thermosphere, since the growth rate of the collisional shear instability depends on the counter streaming flow of the neutrals and plasma. Meridional and vertical winds were neglected in the simulations presented here.

5.4.2 Simulation setup

Our simulation was cast on a rectangular grid 139×133×189 points wide in (p, q, ϕ) space constructed using a tilted magnetic dipole coordinate system. A cut through the equatorial plane spans altitudes between 90–510 km and longitudes between ± 6°. The flux tubes covered by the parallel coordinate all reach

to the lower E region. The runs shown in this section are centered on the dip equator near Kwajalein (5.5° N latitude, 166.5° E longitude, 7.4° declination) with background conditions modeled for April 29, 2009. To seed the simulation run, we added independent Gaussian white noise to the initial number density with a 20% relative amplitude. The local time dependence of the background zonal electric field (E_ϕ) was estimated using measurements from IVM and VEFI on board the C/NOFS satellite. E_ϕ was taken to be constant in the F region but its amplitude is reduced below the valley to avoid the growth of electrojet gradient-drift instabilities. Based on the C/NOFS measurements E_ϕ was modeled as 0 mV/m before 21:00 LT, and 0.75 mV/m after 22:00 LT with a gradual transition using a hyperbolic tangent function in between. For example, E_ϕ=34 μV/m on the western boundary and 0.75 mV/m on the eastern boundary of the simulation by 10:40 UT, since those locations represent 21:22 LT and 22:10 LT, respectively.

5.5 Simulation results

The initial conditions of our simulation at t_0=9:30 UT (≈20:30 LT for the Kwajalein sector) are shown in Figure 5.3. The top panel shows the background plasma density. The initial conditions are consistent with ALTAIR radar observations for April 29, 2009, at that time. The middle panel of Figure 5.3 shows the perpendicular current density with the magnitude and direction indicated by the color disc in the lower panel. There are two major components to the current density that are combined in this depiction. First, a zonally eastward current driven by gravity exists throughout the region, showing a maximum at the F peak near 330 km altitude. In addition, a zonally eastward F region wind

drives a vertical upward current in the region above about 200 km. The empirically modeled wind is almost constant with altitude, and thus the vertical current scales like the background ion density, showing a peak near 330 km and a strong vertical gradient in the bottomside between 280 km and 240 km altitude. Below 150 km, the current is influenced by both the local zonal winds and the enhancement of the zonal current in the electrojet.

The divergence in the vertical current density is supported by a vertical electric field shown to the right of the middle panel. Above the bottomside, the field is directed downward, consistent with an eastward $\mathbf{E} \times \mathbf{B}$ drift in the same direction as the dynamo wind. Across the bottomside, the vertical electric field changes direction, producing a sheared zonal $\mathbf{E} \times \mathbf{B}$ drift, which provides free energy for the CSI below the shear node due to the differential velocity between plasma and neutrals.

The bottom panel of Figure 3 shows equatorward currents in both hemispheres on field lines that thread the bottomside in the altitude range from 250 km to 280 km. These currents feed the upward current driven by the *F* region zonal wind seen in the middle panel. Above the bottomside, the meridional current is distributed across all the field lines and is poleward in both hemispheres, serving to close the current loop driven by the *F* region dynamo.

Figure 5.4 shows the results for times matching, roughly, the three ALTAIR scans and C/NOFS passes. Note that the vertical axes indicate the apex altitude, i.e., the altitude mapped to the magnetic equator. For example, the magnetic field line that crosses over Kwajalein at 380 km altitude maps to 400 km altitude at the magnetic equator.

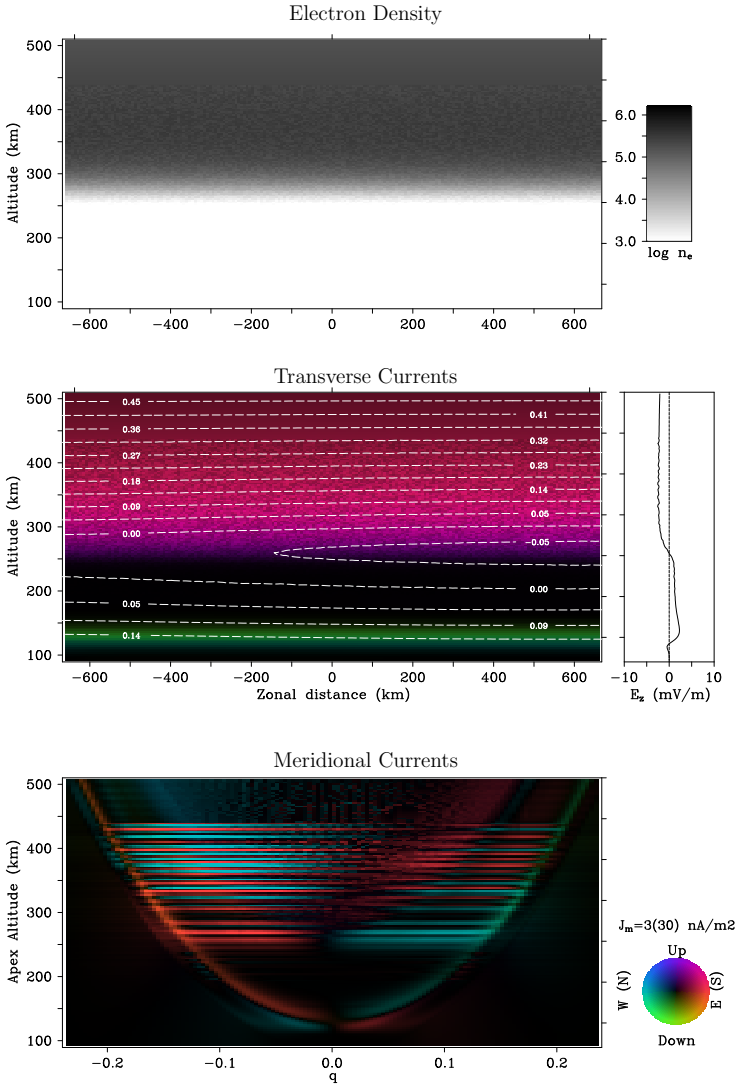

Figure 5.3: Initial conditions for ESF model run (i.e., at t_0 = 9:30 UT). Top: Plasma number density. Middle: Transverse current density in the equatorial plane with equipotential contours (in kV) superimposed in white. Middle right: vertical electric field. Bottom: current density in the meridional plane. The current densities are vector quantities with magnitudes and directions indicated by the color wheel at the bottom right. Information outside and inside brackets characterize currents in the equatorial (middle panel) and meridional plane (bottom panel), respectively. The maximum scale is 3 nA/m^2 in the equatorial plane and 30 nA/m^2 in the meridional plane. Note that diamagnetic currents are not represented in this diagnostic figure.

The top panel of Figure 5.4 depicts the evolution of ionospheric irregularities in the absence of a background electric field due entirely to the collisional shear instability. The spatial scales of the irregularities forming at the base of the bottomside range between 30–50 km. These irregularities cannot undergo vertical development and remain confined to altitudes where the plasma flow is retrograde.

By the time of the second panel in Figure 5.4, the transient phase of the CSI was ending, and the asymptotic phase was underway. The 30–50 km waves at the base of the bottomside have coalesced into large-scale waves with scale sizes between 100-200 km. Under the action of an increasing background zonal electric field, the bottomside irregularities begin to exhibit vertical development, more so on the eastern side of the simulation volume, which has experienced an eastward background electric field for more time.

In the final panel of the simulation, under the influence of a significant background electric field, the irregularities penetrate to the topside where gravity-driven currents can contribute further to growth. Some of the original intermediate scale structure from the first panel in the simulation survive, contributing to the overall fine structure. Bifurcation is evident, as well as secondary instabilities growing mainly on the western walls of the primaries. Some descending, wedge-shaped plasma enhancements accompany the ascending depletions. The characteristic westward tilt of the irregularities is associated with the combination of vertical and zonal currents and the combined CSI and gRT instabilities. As the simulation was initialized with white noise, and as gRT is a universal instability (nearly scale-size independent), the scale sizes of the irregularities evident here are a consequence of CSI.

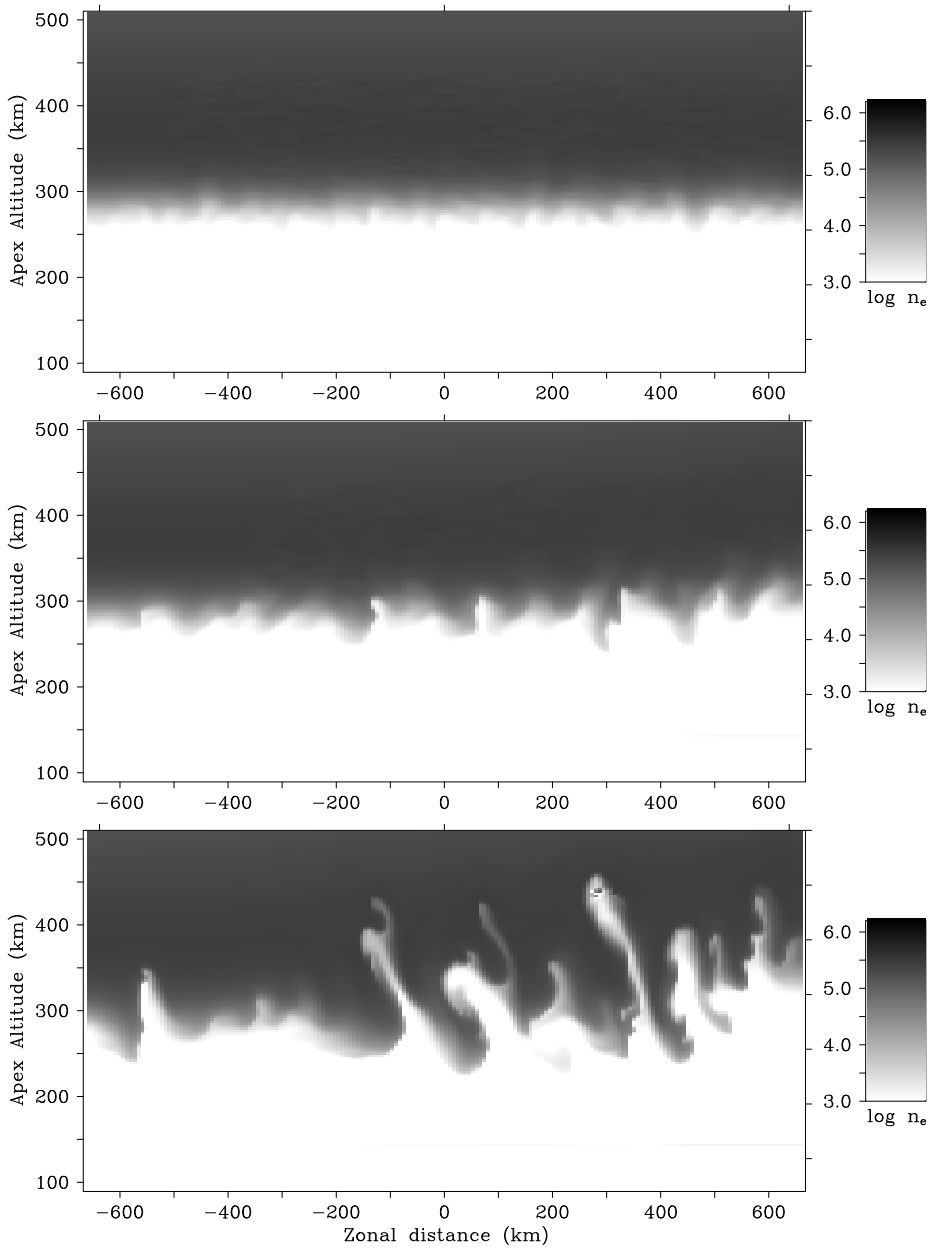

Figure 5.4: Simulated plasma densities in a cut through the Kwajalein latitudinal plane. The three panels show results for simulation times of 0h35m, 1h10m, and 1h43m, respectively, after a start time t_0 = 9:30 UT (LT = UT + 11 hr at the horizontal center of the simulation).

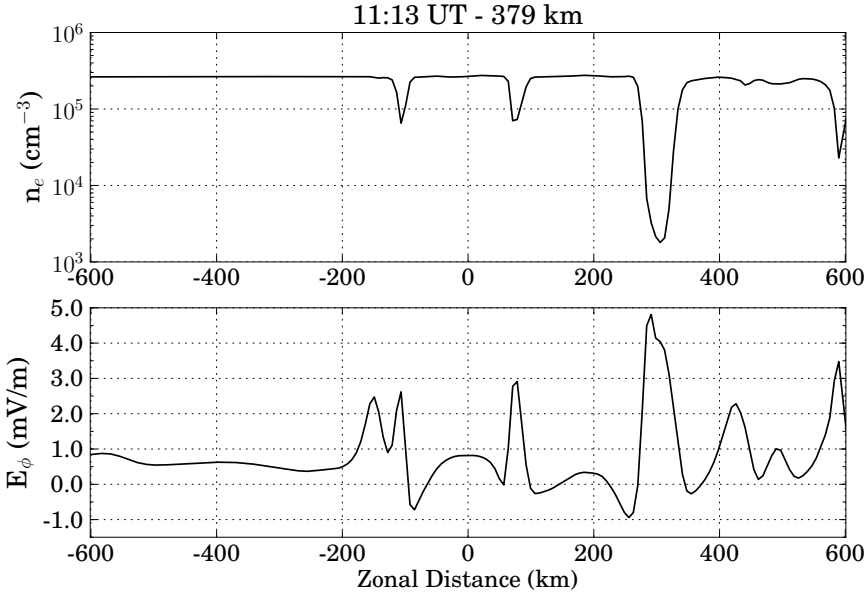

Figure 5.5: Electron density (cm^{-3}) and zonal electric field (mV/m) at 11:13 UT obtained from a longitudinal cut through the simulation at 379 km altitude over the Kwajalein sector (~400 km apex altitude).

Had a satellite passed through the simulated ionosphere at 379 km altitude over the Kwajalein sector (~400 km apex altitude) at about 11:13 UT, the electron density and electric field perturbations would have appeared as shown in Figure 5.5. Plasma depletions are present preferentially in the eastern half of the simulation grid. The western walls of the irregularities have steeper density gradients than the eastern walls. Perturbations in the zonal electric fields of the order 3-5 mV/m are present, collocated with large and small plasma depletions alike. Since the pass is a few kilometers above the top of most of the plasma depletions, relative perturbations in the density are small in all but one case, but the fringing fields penetrate to higher altitudes and are detectable in all cases.

5.6 Discussions

In simulation, the combination of CSI and gRT produced growing waveforms with characteristics that matched the observations made by ALTAIR radar. The dominant plasma irregularities with (initially) decakilometric-scale took approximatelly 100min to evolve from the bottomside up to the *F* peak. By the time they reached the *F* peak, they have coalesced into waveforms with 100 km+ scale sizes. This behavior was observed in ALTAIR scans and simulation results.

The transient response of CSI explained ~ 30-50 km wave observations, a feature commonly observed by backscatter scatter radars in the form of patchy bottom-type ESF. These intermediate-scale irregularities were observed initially in both the simulations and the radar observations but did not reappear after they coalesced into emergent 100 km+ scale irregularities. This result agrees with observations made at other longitudinal sectors, e.g., at Jicamarca (*Hysell*, 2000).

During the asymptotic growth phase, when intermediate-scale depletions dominated the scenario, some of the irregularities remained confined to the bottomside, while others experienced more vertical development. Had these irregularities been observed with coherent scatter, e.g., by the Jicamarca radar, they would have been labeled bottomside ESF. The irregularities in the middle panels of the simulation (Figure 5.4b) and radar data (Figure 5.1b) are comparable in terms of scale sizes and altitude spans.

The last stage of development of ESF occurred when the vertical extension of the plasma depletion was large enough that the irregularities crossed through

the peak into the topside. Similar features are observed in both the simulation (Figure 5.4c) and the radar data (Figure 5.1c). Depletions that reached the *F* peak were spaced by hundreds of km and displayed tilts close to 30° westward from zenith.

Measurements made by IVM showed that electric field perturbations of the order of a few mV/m were sometimes observed even when depletions in the densities were not detected. Similar features were present in the simulation and seemed to be a natural characteristic of the ESF morphology. The simultaneous measurements of small relative perturbations in the density and large zonal electric field perturbations seems to be a consequence of a satellite pass near the top of a plasma depletion. Since the depletion itself was not intercepted, it was not observed, but the fringing fields penetrated to higher altitudes and were detected.

Zonal neutral winds in the bottomside and valley regions exerted control over initial irregularity formation. This sensitivity to the winds was expected, since the growth rate of the collisional shear instability depends on the counter streaming flow of the neutrals and plasma (*Hysell et al.*, 2006*a*). As wind measurements in the lower thermosphere and mesosphere show considerable variability (*Larsen*, 2002), sensitivity tests to winds at those altitudes need to be performed to evaluate their effects on ESF initiation.

5.7 Summary

The combination of generalized Rayleigh-Taylor and collisional shear instability produced growing waveforms with characteristics matching satellite and radar

observations in terms of their gross morphology and rates of development. Growing intermediate- (~30 km) and large-scale (100+ km) waves resulted from the nonlocal and non-normal characteristics of the system and were not imposed a priori. The transient response of CSI explained rapid intermediate-scale wave emergence at the base of the *F* region, whereas the steady-state behavior seemed to account for the large-scale waves that ultimately dominated. The three different types of ESF (bottom-type, bottomside, and topside) appeared to be a result of the time sequencing of the transient and steady-state response of CSI in relation to the zonal electric field.

CHAPTER 6

EQUATORIAL SPREAD *F*-RELATED CURRENTS: 3-D SIMULATIONS AND OBSERVATIONS

Measure what is measurable, and make measurable what is not so.

–Galileo Galilei

6.1 Introduction

In the last two decades, experimental evidence of magnetic perturbations associated with ESF has been shown by magnetometers onboard the San Marco-D and AE-2 (*Aggson et al.*, 1992), CRRES (*Koons et al.*, 1997), CHAMP (*Lühr et al.*, 2002), and DEMETER satellites (*Pottelette et al.*, 2007). *Bhattacharyya and Burke* (2000), using a transmission line analogy, explained those magnetic perturbations in terms of field-aligned currents (FAC) generated by equatorial *F* region irregularities. Experimental observations made by the DEMETER satellite support this idea (*Pottelette et al.*, 2007).

To evaluate how the electric current loop closes in the presence of those plasma depletions, we perform three-dimensional simulations of ESF under realistic conditions. We then compute the magnetic perturbations due to currents in the presence of well-developed depletions with the help of a diagnostic code based on Ampère's law. ESF development and morphology are validated against ALTAIR radar data, and the magnetic perturbations are compared to

*This chapter is based on the original published work, *Aveiro et al.* (2011). Reproduced by permission of the American Geophysical Union.

CHAMP satellite data. The simulation is based on an electrostatic potential solver which enforces the divergence-free current constraint. The scheme does not include any electromagnetic features (i.e., Alfvén waves are not part of the system).

The main issue we address here is the degree to which it is possible to predict the current densities related to ESF and their relative contributions to space-based magnetometer measurements given an appropriate specification of the initial conditions and the forcing.

6.2 Radar observations

We begin with a presentation of radar observations in the Pacific sector that will ultimately be used to motivate and validate the numerical simulations. The ARPA Long-Range Tracking and Instrumentation Radar (ALTAIR) is a VHF/UHF radar located at Kwajalein Atoll (8.8°N, 167.5°E). ALTAIR observations made perpendicular to the geomagnetic field at *F* region heights represent a combination of coherent and incoherent scatter, whereas off-perpendicular scans reflect only incoherent scatter. Both can be useful ESF diagnostics.

The radar observations described below were used to guide the numerical simulations in terms of ESF development and morphology. Figure 6.1 displays ALTAIR UHF (422 MHz) data for the night of August 11, 2004, acquired during the EQUIS II rocket campaign (*Hysell et al.*, 2006*b*). By 10:39 UT (top panel), a meridional scan revealed the presence of multiple depleted flux tubes. Note how one of the anomaly crests interacted with the plasma depletions north of the radar site. By 10:50 UT (bottom panel), a perpendicular (to the geomagnetic

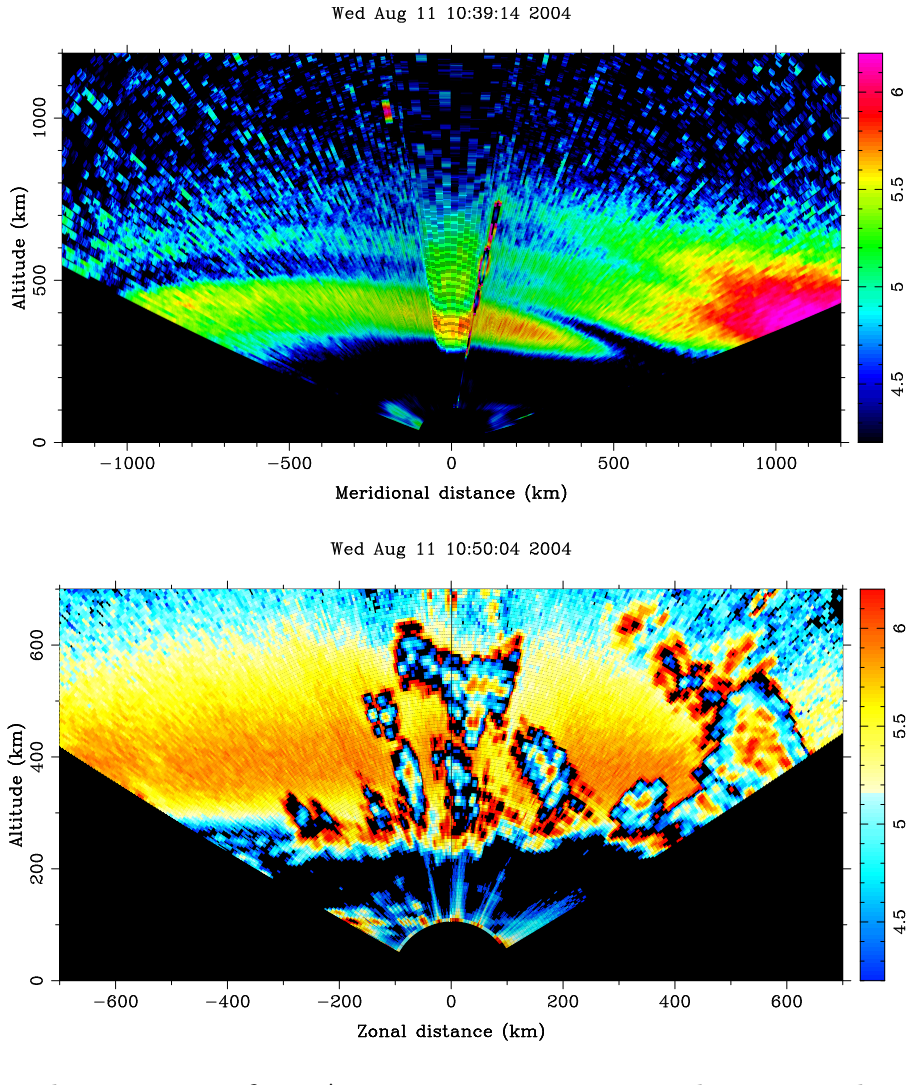

Figure 6.1: ALTAIR radar scans for August 11, 2004, showing backscatter power, range corrected and scaled to electron density on a logarithmic scale: (top panel) meridional scan by 10:39 UT and (bottom panel) perpendicular scan by 10:50 UT. (LT ≈ UT + 11 hr for the Kwajalein sector).

field) scan showed a quasi-periodic train of large-scale depletions spaced by 100-200 km and tilted westward.

6.3 Numerical simulations

The simulation described here is cast on a coordinate system based on the mean magnetic field: "ϕ" and "L" denote directions perpendicular to the magnetic meridian and point eastward (zonal) and outward (meridional), respectivelly, whereas "||" represents quantities along the mean field. The model uses a rectangular grid 139×189×133 points wide in $(L, \phi, ||)$ space. A cut through the equatorial plane spans altitudes between 90–510 km and longitude excursions between ± 6°. The flux tubes covered by the parallel coordinate all extend to the lower E region. The simulation updates ion density and electrostatic potential in time based on the requirements of quasineutrality, continuity equation and momentum conservation. Inertia is neglected in the present incarnation. We take the ionosphere and neutral atmosphere to be in thermodynamic equilibrium after sunset ($T_n = T_e = T_i$). The runs shown below are centered on the dip equator near Kwajalein (5.5° N latitude, 166.5° E longitude, 7.4° declination) with background conditions modeled for August 11, 2004. To seed the simulation run, we added independent Gaussian white noise to the initial number density.

6.3.1 Model description

The simulation algorithm performs two computations. First, the self-consistent ionospheric potential is solved using the BiConjugate Gradient Stabilized (BiCGStab) method using the algorithms described by *Saad* (1990). We neglect diagmagnetic currents here, since their associated flux divergence is very small compared to the other terms (see, e.g., *Aggson et al.* (1992)). Second, ion velocities are obtained from the momentum equation (inertia is neglected in the

present incarnation) and we solve a discretized version of continuity equation (Equation 2.1) for each ion species using a monotone upwind scheme for conservation laws (MUSCL) (e.g. *Trac and Pen* (2003)).

To initialize the model runs, densities and temperatures were derived from empirical models (see Chapter 4 for a more complete description of the inputs). We took the ionosphere and neutral atmosphere to be in thermodynamic equilibrium after sunset. The forcing due to the zonal background electric field was based on the Scherliess-Fejer model (*Scherliess and Fejer*, 1999). For our runs, only the zonal neutral winds were considered. These were based on profiles measured during the EQUIS II sounding rocket campaign (August 7, 2004) between 100-150 km. Lacking wind measurements above 150 km, we made use of the Horizontal Wind Model (HWM-07) above 200 km altitude. For altitudes in between, the wind profiles were joined smoothly by a continuous function.

To compute the magnetic induction due to ionospheric currents, we used Ampère's law ($\nabla \times \mathbf{B} = \mu_0 \mathbf{J} + \dot{\mathbf{E}}/c^2$). Contributions from the Earth's magnetic field can be neglected since the simulations were built on a magnetic dipole field, which is irrotational. Note that, despite being neglected during the computation of the electrostatic potential, diamagnetic currents ($=\sum_\alpha d_{H\alpha} \nabla n_\alpha \times \hat{\mathbf{q}}$, where α=O^+, NO^+, O_2^+, and electrons) are included in the diagnostic computation of the magnetic field perturbations (see *Shume et al.* (2005) for an explicit definition of the Hall diffusion coefficient $d_{H\alpha}$). Neglecting displacement currents and applying the curl operator to Ampère's law gives:

$$\nabla^2 \mathbf{B} = -\mu_0 \nabla \times \mathbf{J}. \tag{6.1}$$

Equation 6.1 represents a set of three independent partial differential equations for B_L, B_ϕ, and $B_\parallel$. These were solved by applying Neumann boundary condi-

tions and using the BiCGStab method in a manner similar to the electrostatic potential described above. After the computation of the magnetic field, a consistency check with the current system was performed using Equation 6.1 to verify agreement.

6.3.2 Model results

Figure 6.2 shows representative diagnostic information for 10:24 UT. Figure 6.2a shows the plasma number density. By this time, plasma irregularities, spaced by 100-200 km, had reached the top of the simulation.

The right-top color scale is used to indicate the magnitude and direction of the transverse current densities (scale maximum is 20 nA/m^2) and transverse magnetic induction (scale maximum is 3 nT). Figure 6.2c shows the tranverse current density in the equatorial plane. Diamagnetic currents are observed flowing on the external walls of the plasma depletions in a clockwise direction. If evaluated together with Figure 6.2d, which indicates parallel magnetic inductions due to ionospheric currents, it can be seen that the currents caused northward deflections of $B_{\parallel}$ inside the plasma irregularities.

Figure 6.2e and 6.2g displays the parallel currents at conjugate points ±4° mag. latitude, respectivelly, north and south of the magnetic equator. The panels next to the parallel currents indicate the associated transverse magnetic inductions. FAC flow poleward (equatorward) on the external west (east) walls of the plasma depletions. Transverse magnetic induction showed a downward (upward) deflection inside the depletions north (south) of the magnetic equator. Transverse magnetic perturbations were negligible in the equatorial plane due

to very small FAC and are not shown. The parallel current pattern observed in the simulations agrees with the schematic view in Figure 12 of *Stolle et al.* (2006).

6.3.3 Simulation vs. satellite comparisons

Had a satellite passed through the simulated ionosphere at 380 km altitude over the Kwajalein sector at about 10:24 UT, the electron density and magnetic field perturbations would have appeared as shown in the left panels of Figure 6.3. Magnetic field data were high-pass filtered by a median filter (~ 700 km) to remove large-scale variations. The simulated results show a plasma depletion at ~ -5° mag. latitude, collocated with an upward/westward $\Delta B_{\perp}$ of ~1.4 nT and a northward $\Delta B_{\parallel}$ of ~0.7 nT. A smaller transverse perturbation in the opposite direction (downward/eastward) was also detected next to the eastern wall of the plasma depletion.

To compare the computed magnetic field inductions with observations, we used *in situ* magnetic field and plasma density measurements made by a Fluxgate Magnetometer (cross-calibrated with an Overhauser Magnetometer) and a Plasma Langmuir Probe on board the Challenging Mini-satellite Payload (CHAMP). The satellite operated from July, 2000, to September, 2010, for studies related to the gravity field, geomagnetic field, and the atmosphere (*Lühr et al.*, 2002). The satellite orbit altitude was about 380 km in 2004, inclined by 87.3° with respect to the equatorial plane, i.e., the orbit track was nearly parallel to the geographic meridian.

Following the *Park et al.* (2009) and *Stolle et al.* (2006) methodology, non-ionospheric contributions were removed from magnetic field measurements.

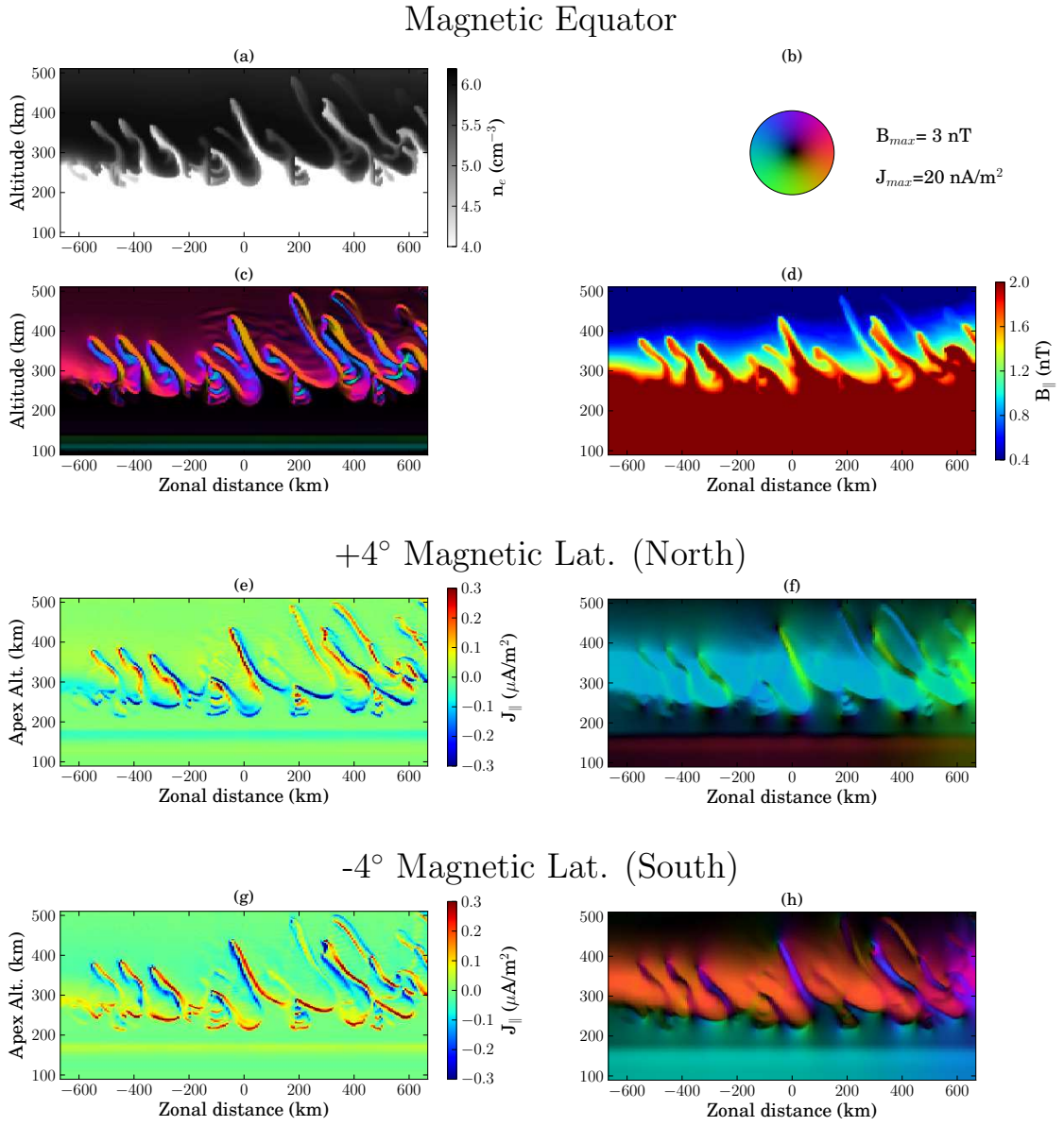

Figure 6.2: Diagnostic at 10:24 UT: (a) Plasma density in a cut through the equatorial plane on a log scale, (b) color scale of the magnitude and direction of the tranverse current densities (scale maximum is 20 nA/m^2) and transverse magnetic inductions (scale maximum is 3 nT), (c) Tranverse current densities and (d) parallel magnetic induction in the equatorial plane, (e) parallel current density and (f) transverse magnetic induction at 4° mag. latitude, and (g) parallel current density and (h) transverse magnetic induction at -4° mag. latitude.

The residual fields were further filtered by a 91-point median filter (~ 700 km) to remove large-scale variations. The final results represent short-scale deviations from the average magnetic field. The right panels of Figure 6.3 display CHAMP observations for August 11, 2004, by 10:00 UT, approximatelly at 178° geographic longitude. Since the satellite flew northward, when crossing a plasma depletion, the eastern wall is sampled first (due to the orbit inclination angle with respect to the magnetic flux tube in this longitude sector). The measurements indicated three main depletions in the plasma density (at magnetic latitudes ~ -4°, 2°, and 10°). The depletion south of the magnetic equator (-4° mag. latitude) is collocated with magnetic perturbations in both the meridional and zonal components. The large upward deflection of the magnetic field inside the plasma depletion indicates a poleward (equatorward) current flowing on the external edge of the western (eastern) wall. The westward deflection of the magnetic field inside the depletion may be due to westward tilt of the ESF (as shown in Figure 6.2e and 6.2g). Finally, collocated with the plasma depletions, northward deflections of the magnetic field were detected. Note that the magnetic perturbation pattern observed by CHAMP is similar to the result obtained by the satellite pass simulation.

6.4 Summary

A three-dimensional numerical simulation of plasma density irregularities in the postsunset equatorial *F* region ionosphere leading to equatorial spread *F* (ESF) was performed to investigate the closure of ionospheric currents in the presence of plasma depletions. The simulation produced growing waveforms with characteristics that matched the observations made by ALTAIR radar, both

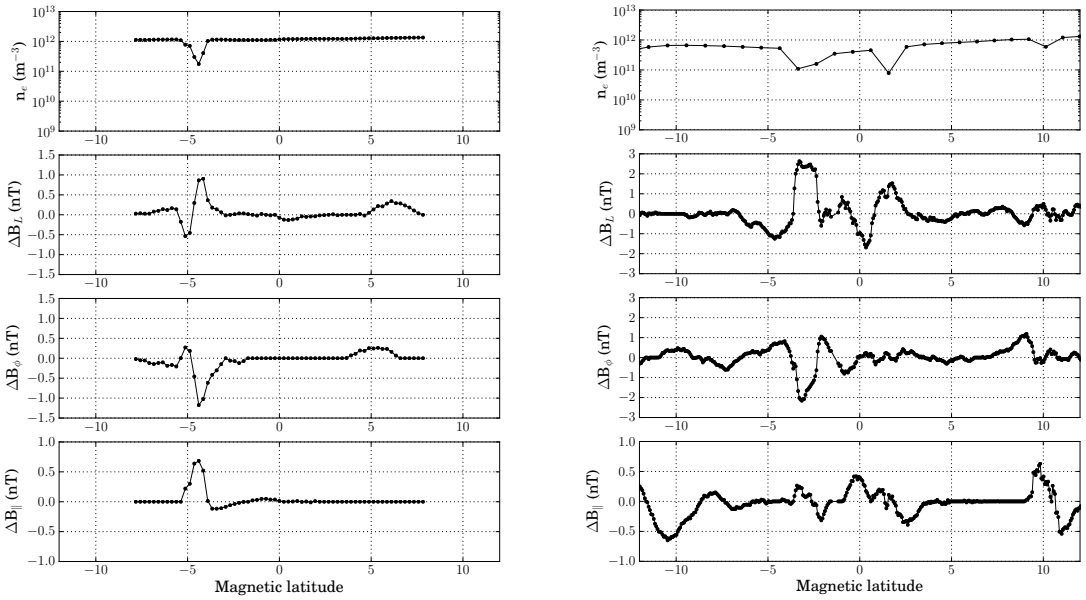

Figure 6.3: (Left) Simulated satellite observations for August 11, 2004 at 10:24 UT, and (right) CHAMP observations for August 11, 2004, 10:00 UT: (top panel) plasma density, (middle-top panel) meridional, (middle-bottom panel) zonal, and (bottom panel) parallel magnetic field perturbations.

in terms of their gross morphology and their rates of development.

Overall, the simulated magnetic field perturbations show good qualitative with the CHAMP measurements. The simulation reproduces the main features of the plasma depletions as derived in a statistical study by *Park et al.* (2009), e.g. upward (downward) currents on their external western (eastern) edges. The field-aligned currents (FAC) showed large amplitudes associated with the divergence of the (mainly gravity-driven) zonal current at *F* region altitudes in the presence of ESF. FAC flow poleward (equatorward) on the external edges of the western (eastern) walls of the plasma depletions, i.e., strong FAC are associated with transverse currents closing around deep density depletions.

We find that the transverse magnetic field perturbations are due almost entirely to FAC, whereas the parallel perturbations are due almost entirely to diamagnetic currents. Other currents (e.g., Pedersen and Hall) seem to make only minor contributions. That the simulation is electrostatic argues against an Alfvénic interpretation of all of the CHAMP magnetic field observations in ESF.

CHAPTER 7

NUMERICAL SIMULATIONS OF EQUATORIAL SPREAD *F*: RESULTS AND DIAGNOSTICS IN THE PERUVIAN SECTOR

Facts which at first seem improbable will, even on scant explanation, drop the cloak which has hidden them and stand forth in naked and simple beauty.

–Galileo Galilei

7.1 Introduction

In this chapter, we perform numerical simulations of equatorial spread *F*, assessing the roles of CSI & gRT and comparing the results with different kinds of space weather diagnostics. The diagnostics in question include magnetometers onboard satellites, airglow imagers, and coherent/incoherent scatter radar. The main issue we address here is the degree to which the simulations can reproduce the salient features in remote sensing and in situ measurements of the plasma irregularities in ESF, such as tilting, spacing, layer thickness, altitude range, onset time, and rate of development.

7.2 Numerical model

Below, we describe a numerical scheme for the simulation of the plasma density irregularities in equatorial spread *F*. The 3-D simulation updates the plasma density and electrostatic potential in time assuming quasineutrality and momentum balance. Inertia is neglected in the present incarnation. The charac-

teristics of the neutral atmosphere are imported from empirical models. The background electric field is specified and controls the forcing. Simulations are performed with realistic background conditions including bottomside plasma shear flow and the attendant vertical current.

The simulation algorithm performs two computations. First, the self-consistent electrostatic potential is found by solving Equation 2.10 using the BiConjugate Gradient Stabilized (BiCGSTAB) method (e.g. *van der Vorst* (1992)) using the algorithms described by *Saad* (1990). Under this scheme, the system of equations is preconditioned by an incomplete LU factorization with a dual truncation strategy. The equation we advance in time is the production- and loss-free version of the continuity equation for the ions (Equation 2.1). Our approach is to solve a discretized version of Eq. 2.1 using the Monotone Upwind Scheme for Conservation Laws (MUSCL) (see description of the method in Appendix A).

7.2.1 Empirical model drivers

To initialize the model runs, we derive plasma number densities from the Parametrized Ionospheric Model (PIM), a parametrization of the output of several regional theoretical model outputs generated for different climatological conditions and tuned somewhat to agree with data from Jicamarca and elsewhere (*Daniell et al.*, 1995). The background number density profiles used for initial conditions are intended to reproduce measurements from Jicamarca, including the *F* region peak height and peak density, the bottomside density scale height, and the density in the valley region.

Plasma mobilities are calculated using neutral composition and temperature estimates from the Mass Spectrometer and Incoherent Scatter (NRL-MSISE00) model (*Picone et al.*, 2002) and ionospheric composition estimates from the International Reference Ionosphere (IRI-2007) model (*Bilitza and Reinisch*, 2008). We take the ionosphere and neutral atmosphere to be in thermodynamic equilibrium after sunset ($T_n = T_e = T_i$). The zonal neutral winds are obtained from the Horizontal Wind Model (HWM-07) (*Drob*, 2008). As with PIM, these may be tuned slightly to account for day-to-day variability. The model is sensitive to the wind speeds throughout the thermosphere, since the growth rate of the collisional shear instability depends on the counter streaming flow of the neutrals and plasma. Meridional and vertical winds were neglected in the simulations presented here.

7.2.2 Simulation setup

Our simulation was cast on a rectangular grid 139×133×189 points wide in (p, q, ϕ) space constructed using a tilted magnetic dipole coordinate system. A cut through the equatorial plane spans altitudes between 90–510 km and longitudes between ± 6°. The flux tubes covered by the parallel coordinate all extend to the lower *E* region. The runs shown below are centered on the dip equator near Jicamarca (-12.2° N latitude, 283.1° E longitude) with background conditions modeled for F10.7=100. To seed the simulation runs, we added independent Gaussian white noise to the initial number density with a 20% relative amplitude. The local time dependence of the background zonal electric field (E_ϕ) was taken to be a symmetric triangular function that was zero for times before 18h LT and after 21h LT, with a peak of 0.8 mV/m at 19h30m LT. This zonal

electric field time history approximates Jicamarca radar observations made on 8 June, 2011 (not shown here). E_ϕ was taken to be constant througout the F region, but its amplitude is reduced below the valley to suppress the growth of gradient-drift instabilities in the electrojet.

The initial conditions of our simulation at t_0=0:15 UT ($\approx$19:15 LT for the Peruvian sector) are shown in Figure 7.1. The top panel shows the background plasma density. The middle panel of Figure 7.1 shows the perpendicular current density with the magnitude and direction indicated by the color disc in the lower panel. There are two major components to the current density that are combined in this depiction. First, a small eastward current driven by gravity exists throughout the region and increases with altitude. In addition, the eastward F-region wind drives a vertical current in the region above about 200 km. The vertical current shows a maximum near 300 km and a strong vertical gradient in the bottomside between 280 km and 340 km altitude. Below 150 km, the current is influenced by both the local zonal winds and the enhancement of the zonal current in the electrojet. Above the bottomside, the electric field is directed downward, consistent with an eastward $\mathbf{E} \times \mathbf{B}$ drift in the same direction as the dynamo wind. Across the bottomside, the vertical electric field changes direction, producing a sheared zonal $\mathbf{E} \times \mathbf{B}$ drift.

The bottom panel of Figure 7.1 shows equatorward currents in both hemispheres on field lines that thread the bottomside in the altitude range from 200 km to 250 km. These currents feed the upward current driven by the F region zonal wind seen in the middle panel. Above the bottomside, the meridional current is distributed across all the field lines and is poleward in both hemispheres, serving to close the current loop driven by the F region dynamo.

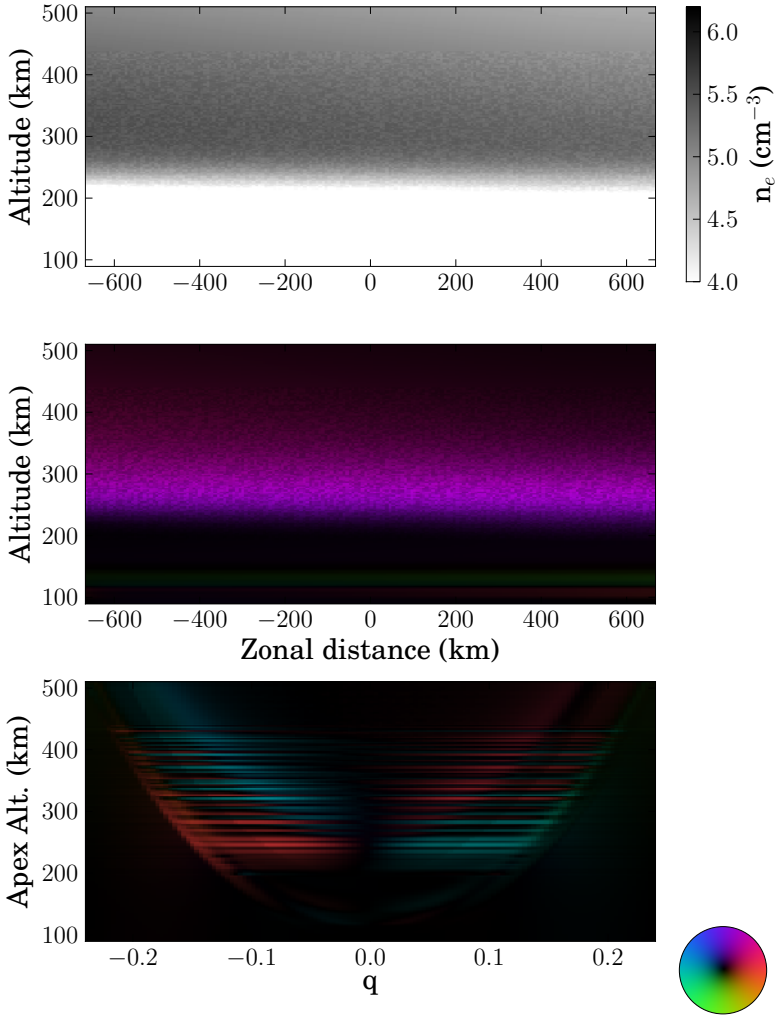

Figure 7.1: Initial conditions for ESF model run (i.e., at t_0 = 0:15 UT). Top: Plasma number density. Middle: Transverse current density in the equatorial plane with equipotential contours (in kV) superimposed in white. Middle right: vertical electric field. Bottom: current density in the meridional plane. The current densities are vector quantities with magnitudes and directions indicated by the color wheel at the bottom right. The maximum scale is 10 nA/m^2 in the equatorial plane and 200 nA/m^2 in the meridional plane. Note that diamagnetic currents are not represented in this diagnostic figure.

7.2.3 Coherent/incoherent scatter radar simulation

Simulated plasma densities in a cut through the magnetic equator are a good proxy for the types of ESF observations made by the ALTAIR radar in the Pacific sector (*Aveiro et al.*, 2012). Figure 7.2 shows the results for times ranging from 0h25 to 2h05 after the start of the simulation. Figure 7.2a depicts the action of the collisional shear instability. The spatial scales of the irregularities forming at the base of the bottomside range between 30–50 km. The wave fronts are not completely vertical but are tilted (westward). These irregularities were confined to altitudes where the plasma flow is retrograde. Figure 7.2b shows the vertical development of the irregularities. The plasma depletions had roll-like shapes, but the strong zonal electric field displaced them vertically by ~50 km. Figure 7.2c depicts the irregularities after they crossed the *F* peak. Bifurcation on the top of the plasma depletions is often evident above the peak. Secondary wind-driven instabilities appear to grow on the western walls of the plasma irregularities. The spatial scales of the irregularities that transcended the *F* peak range between 100–200 km. Had they been observed using a fixed beam coherent scatter radar, the plasma irregularties in Figure 7.2 would be labeled as bottom-type, bottomside, and topside spread *F*, respectively.

The Jicamarca 50 MHz radar is not fully steerable like ALTAIR. This limitation has been overcome to some extent with the advent of ionospheric radar imaging (*Hysell*, 1996; *Woodman*, 1997). However, coherent scatter measured by Jicamarca is still most often presented in a slit camera-like format called range-time-intensity (RTI) maps, which show the temporal behavior of the measured parameter for a span of altitudes. Had the simulated ionosphere been sounded by the Jicamarca radar, the resultant RTI map would have been similar to Fig-

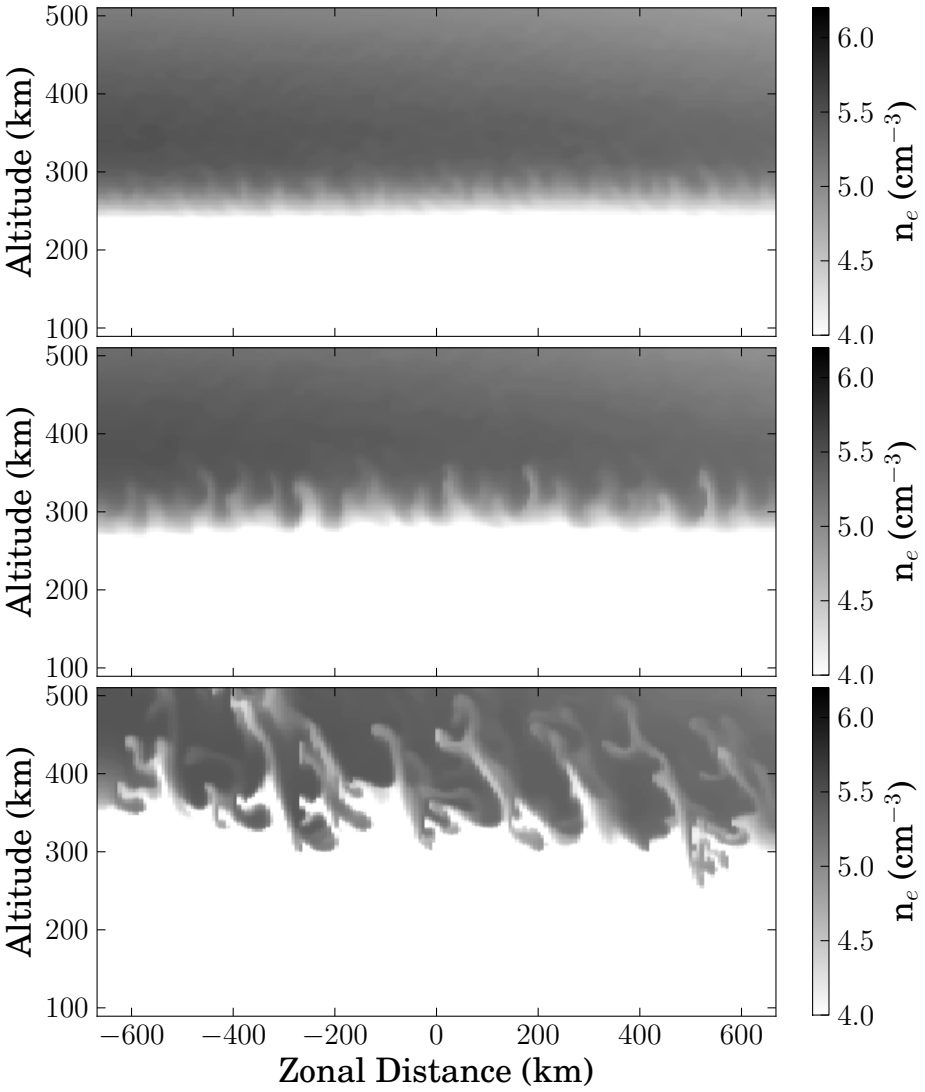

Figure 7.2: Simulated plasma densities in a cut through the Jicamarca latitudinal plane. The three panels show results for simulation times of 0h25m, 0h50m, and 2h05m, respectively, after a start time t_0 = 0:25 UT (LT = UT - 5 hr at the horizontal center of the simulation).

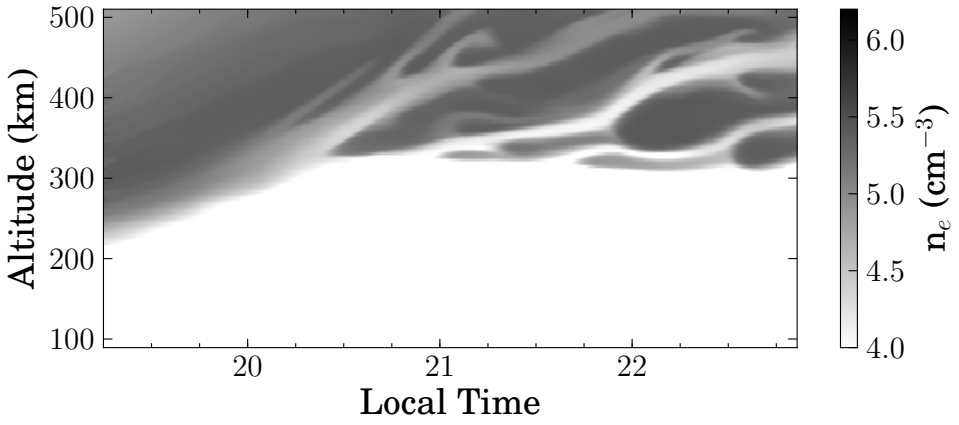

Figure 7.3: Simulated range-time-intensity maps of electron density observations. In a real observation, incoherent scatter would be contaminated by enhanced coherent scatter from regions of depleted densities.

ure 7.3 only with enhanced coherent scatter highlighting the regions of depleted density. During the initial hours of the simulation (before 20h30 LT), the bottomside rose up from ~220 km to ~300 km altitude in ~1h, i.e., at an average ~22 m/s vertical drift. At the same time, the 50 km thick layer (located between the *F* peak and valley) created by the collisional shear instability drifted upward with the background ionosphere. Subsequently, irregularities crossed through the *F* peak and reached the top boundary of the simulation. Some of the topside irregularities formed a "C-shape", a feature commonly observed by coherent scatter radars.

7.2.4 Airglow imagery simulation

Airglow emissions corresponding to the simulation runs were computed for the 6300- (or oxygen red) line. The volume emission rate (in photons cm^{-3} s^{-1})

is given by (*Link and Cogger*, 1988)

$$V_{6300} = \frac{0.76\beta k_1 n_{O^+} n_{O_2}}{1 + (k_2 n_{N_2} + k_3 n_{O_2} + k_4 n_e + k_5 n_O)/A_{1D}} \tag{7.1}$$

where n_α represents the densities for species α and A_{1D} is the Einsten transition coefficient for the O(^{1}D) state (A_{1D}=A_{6300}+A_{6364}+A_{6392}=7.45×10^{-3} s^{-1}, A_{6300}=5.63×10^{-3}, A_{6364}=1.82×10^{-3}, A_{6392}=8.92×10^{-7}) (*Link and Cogger*, 1989). Also, β is the production efficiency of O(^{1}D) from dissociative recombination of O_2^+ and was obtained from the Frank-Condon distribution (Table 13) in *Bates* (1990). The reactions involving the coefficients k_i are given in Table 7.1.

A simulated airglow image was obtained through the integration of the volume emission rates along the camera line of sight. For the present computation, the camera was placed virtually in Chilean territory looking north, i.e., observing the airglow emissions and depleted flux tubes due to *F* region plasma irregularities near Jicamarca. The location of the virtual camera is close to the airglow imaging system at the Cerro Tololo InterAmerican Observatory near La Serena (*Makela and Miller*, 2008). We do not assume a virtual altitude of emission (see *Tinsley* (1982) for a more complete explanation of the geometry involved in the airglow imagery) and use coordinates representing scanning angles in elevation and azimuth. Since typical camera exposure times are longer than a minute (see e.g., *Makela and Miller* (2008)), the simulated airglow emissions represent 2-min averages.

Figure 7.4 shows the postsunset airglow imagery simulation. During the first hours after sunset (Figure 7.4), stronger emissions appeared on the western half of the image due to recombination. Intermediate-scale irregularities (30-50 km) were barely detectable in the bottomside of the *F* region. At t_0+

0h50m, airglow depletions were present almost everywhere. Large-scale airglow depletions were spaced apart by 100-200 km, but smaller ones were also detectable. At t_0+ 2h05m, the emission layers appeared to have drifted upward (i.e., stronger emissions occurred away from the equator). Wide, large-scale depletions were evident with zonal width of tens of kilometers. The last panel (t_0+ 3h20m) shows stronger emissions compared to the previous one (t_0+ 2h05m). Enhanced brightness close to midnight is similar to what has been shown by *Makela and Miller* (2008). Bifurcations and secondary instabilities growing on the western walls of the plasma depletions were also evident; however, the waveforms observed in airglow appeared distorted and fine structure has been lost when compared to the electron density maps in Figure 7.2. Finally, the apparent zonal drift of the irregularities computed based on the frame-to-frame displacement is ~22 m/s. Since the background was drifting at ~60 m/s, this indicates how the irregularities (as measured by airglow) drifted slower than the background ionosphere. This scenario occurs during the first hours after sunset, but as the *E* region density declines, the *F* region dynamo becomes more efficient and both the plasma irregularities and the background plasma drift zonally at the neutral wind speed.

7.2.5 In situ satellite probe simulations

To compute the magnetic induction due to ionospheric currents, we used Ampère's law. Note that, despite being neglected during the computation of the electrostatic potential, diamagnetic currents are included in the diagnostic computation of the magnetic field perturbations. Following *Aveiro et al.* (2011), we neglected the displacement currents and applied the curl operator to Ampère's

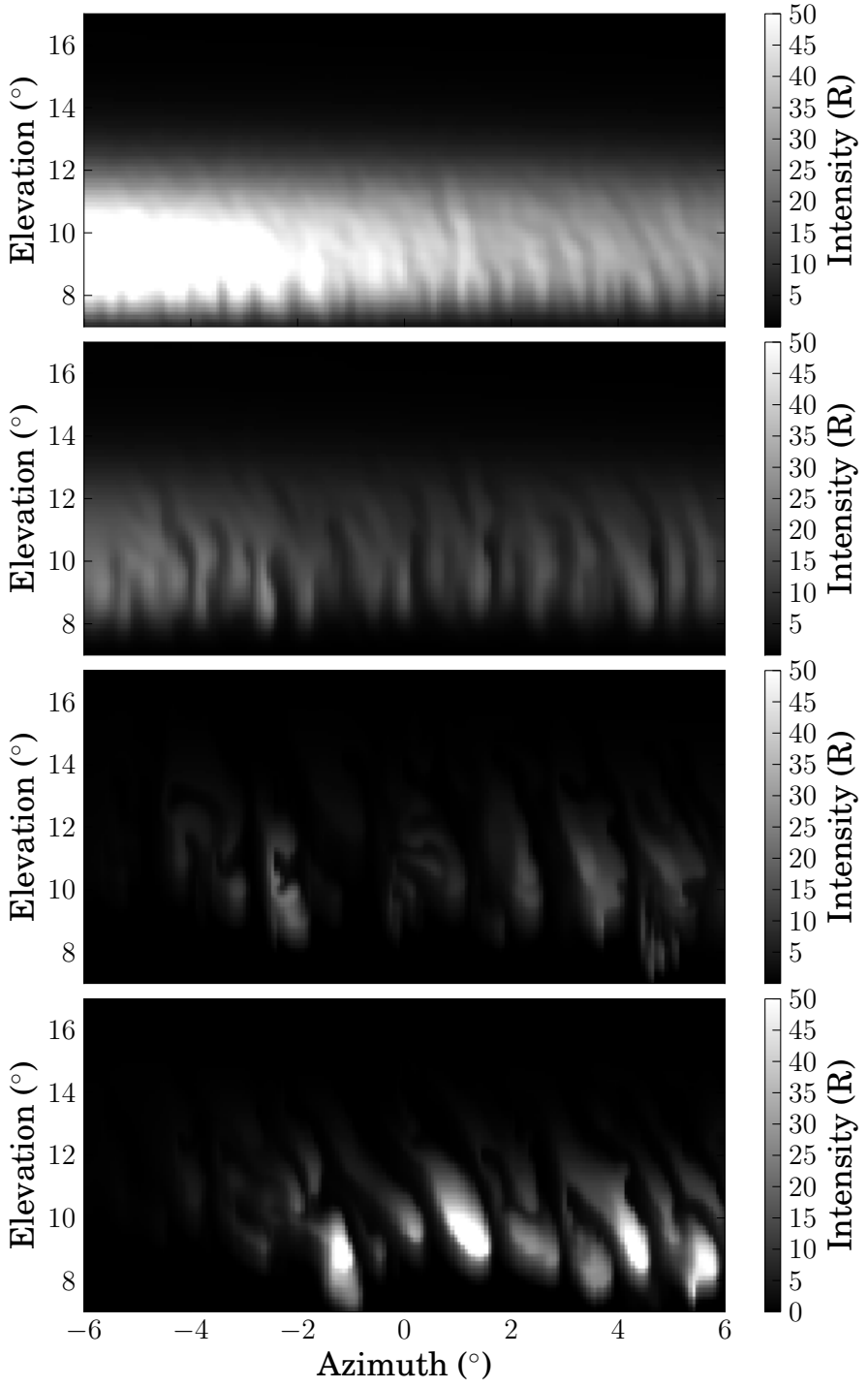

Figure 7.4: Simulated airglow (in Rayleighs) observed by a camera located south of Jicamarca (looking north). The four panels show results for simulation times of 0h25m, 0h50m, 2h05m, and 3h20, respectively, after a start time t_0 = 9:30 UT (LT = UT + 11 hr at the horizontal center of the simulation).

Table 7.1: Chemistry of $O(^1D)$ in the nightglow

Reaction	Rate coefficient [cm^3s^{-1}]*	References
$O^+ + O_2 \rightarrow O_2^+ + O$	$k_1 = 3.23 \times 10^{-12} e^{3.72/\tau_i - 1.87/\tau_i^2}$	*Link and Cogger* (1988)
$O(^1D) + N_2 \rightarrow O(^3P) + N_2$	$k_2 = 2.0 \times 10^{-11} e^{111.8/T_n}$	
$O(^1D) + O_2 \rightarrow O(^3P) + O_2$	$k_3 = 2.9 \times 10^{-11} e^{67.5/T_n}$	
$O(^1D) + e \rightarrow O(^3P) + e$	$k_4 = 1.60 \times 10^{-12} T_e^{0.91}$	
$O(^1D) + O \rightarrow O(^3P) + O$	$k_5 = 2.55 \times 10^{-12}$	*Sobral et al.* (1993)

*$\tau_i = T_i/300$

law, giving $\nabla^2 \mathbf{B} = -\mu_0 \nabla \times \mathbf{J}$., which represents a set of three independent partial differential equations for B_L, B_ϕ, and $B_\parallel$. These were solved by applying Neumann boundary conditions and using the BiCGStab method in a manner similar to the electrostatic potential solution described above. After the computation of the magnetic field, a consistency check with the current system was performed using Ampère's law for magnetostatics to verify agreement.

Figure 7.5 shows representative diagnostic information for 3:35 UT. Figure 7.5a shows the plasma number density. By this time, plasma irregularities, spaced by 100-200 km, had reached the top of the simulation.

The right-top color scale is used to indicate the magnitude and direction of the transverse current densities (scale maximum is 20 nA/m^2) and transverse magnetic induction (scale maximum is 2.5 nT). Figure 7.5c shows the tranverse current density in the equatorial plane. Diamagnetic currents are observed flowing on the external walls of the plasma depletions in a clockwise direction. If evaluated together with Figure 7.5d, which indicates parallel magnetic inductions due to ionospheric currents, it can be seen that the currents caused north-

ward deflections of $B_{\parallel}$ inside the plasma irregularities.

Figure 7.5e and 7.5g display the parallel currents at conjugate points ±4° mag. latitude, respectivelly, north and south of the magnetic equator. The panels next to the parallel currents indicate the associated transverse magnetic inductions. FAC flow poleward (equatorward) on the external west (east) walls of the plasma depletions. Transverse magnetic induction showed a downward (upward) deflection inside the depletions north (south) of the magnetic equator. Transverse magnetic perturbations were negligible in the equatorial plane due to very small FAC and are not shown. The parallel current pattern observed in the simulations agrees with the numerical simulations described by *Aveiro et al.* (2011) and the statistical results of *Stolle et al.* (2006) and *Park et al.* (2009) based on CHAMP satellite data.

Had a satellite passed through the simulated ionosphere at 380 km altitude over the Jicamarca sector at about 10:35 UT, the electron density and magnetic field perturbations would have appeared as shown in Figure 7.6. Magnetic field data were high-pass filtered by a median filter (~ 700 km) to remove large-scale variations. The simulated results show a plasma depletion at ~ ±6° mag. latitude, collocated with a northward $\Delta B_{\parallel}$ and an upward/westward (downward/eastward) $\Delta B_{\perp}$ south (north) of the magnetic equator.

7.3 Summary and discussions

A three-dimensional numerical simulation of plasma density irregularities in the postsunset equatorial *F* region ionosphere leading to equatorial spread *F* (ESF) was performed to investigate plasma irregularity signatures in different

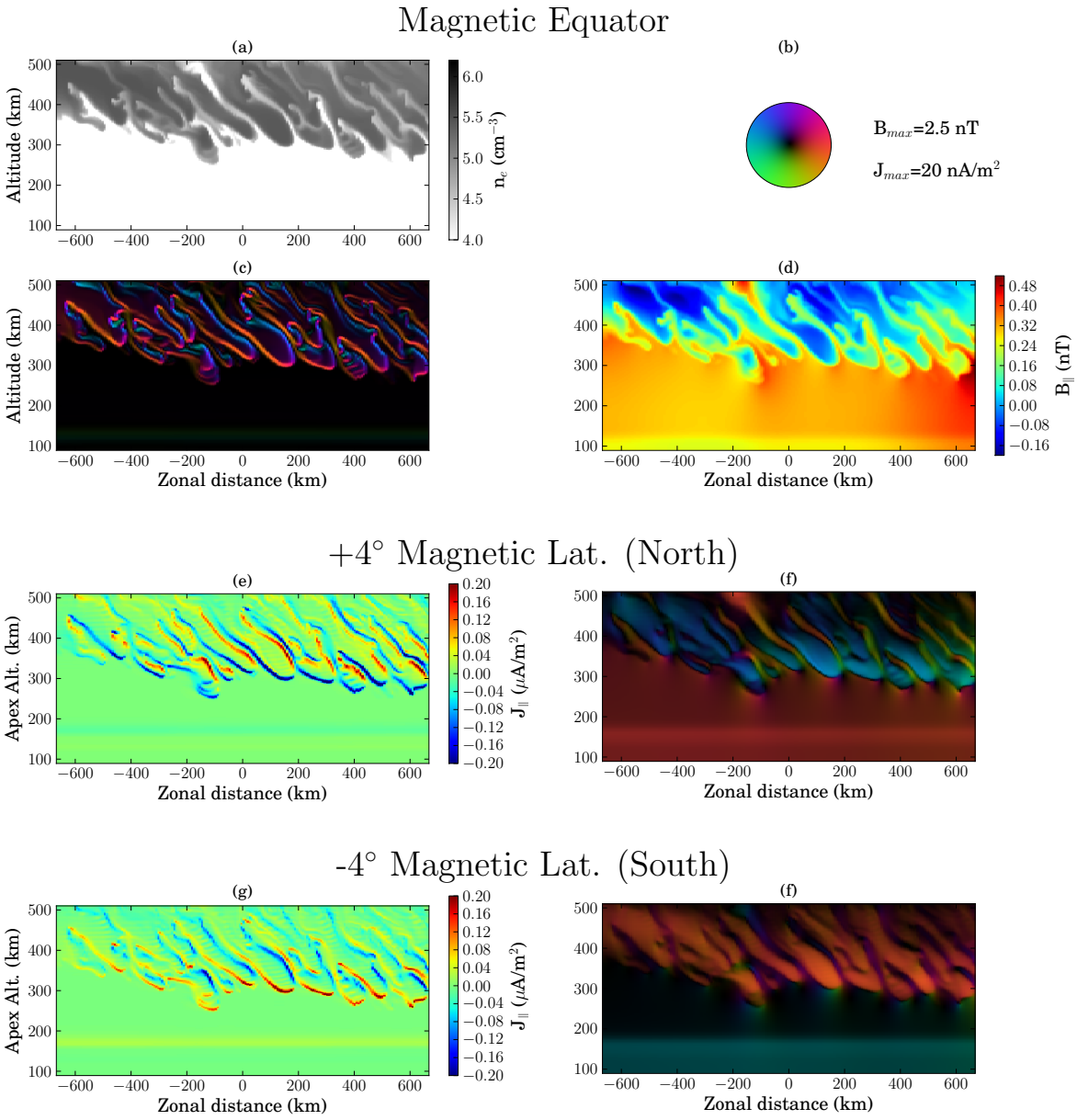

Figure 7.5: Diagnostic at 3:35 UT: (a) Plasma density in a cut through the equatorial plane on a log scale, (b) color scale of the magnitude and direction of the tranverse current densities (scale maximum is 20 nA/m^2) and transverse magnetic inductions (scale maximum is 2.5 nT), (c) Tranverse current densities and (d) parallel magnetic induction in the equatorial plane, (e) parallel current density and (f) transverse magnetic induction at 4° mag. latitude, and (g) parallel current density and (h) transverse magnetic induction at -4° mag. latitude.

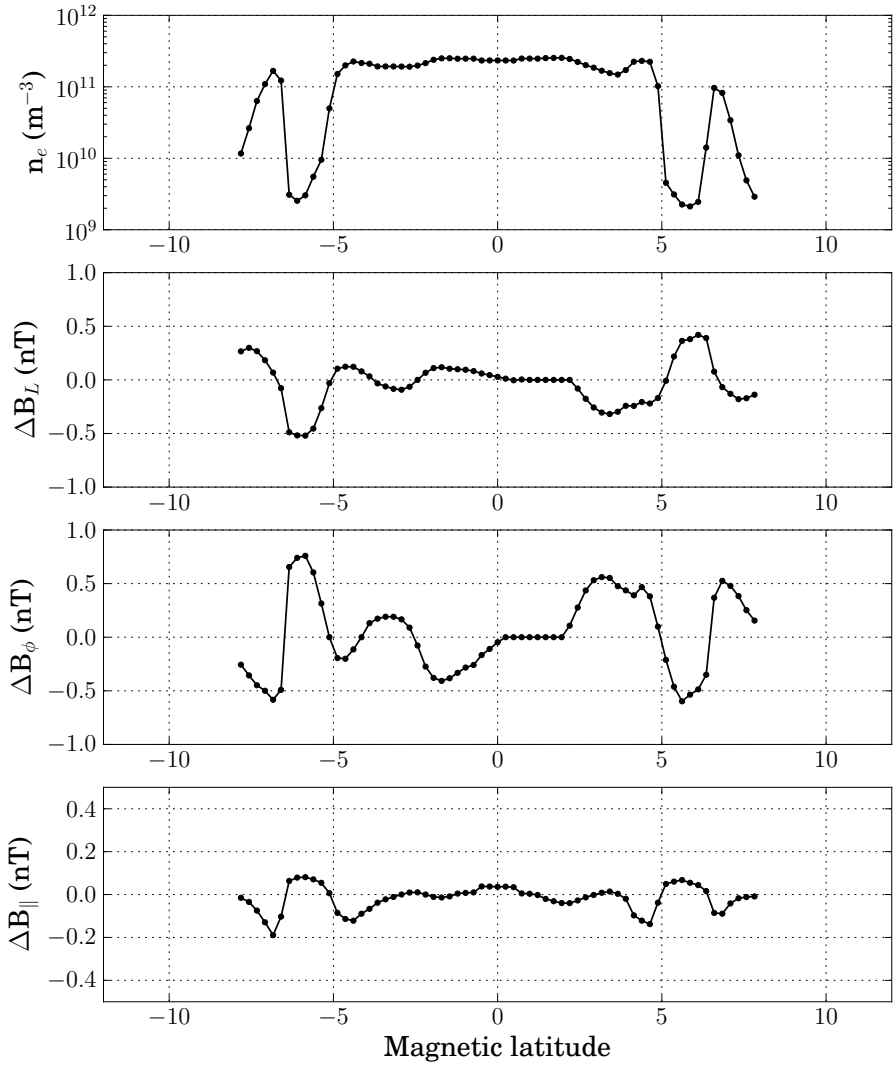

Figure 7.6: Simulated satellite observations during a meridional pass: (top panel) plasma density, (middle-top panel) meridional, (middle-bottom panel) zonal, and (bottom panel) parallel magnetic field perturbations.

space plasma diagnostics. The simulation of coherent/incoherent scatter observations showed the typical three stages of ESF evolution, from bottom-type to bottomside to topside spread *F*. Some of the features that the simulated electron density maps share with ALTAIR scans include westward tilted ascending depletions connected to the bottomside, periodic spacing of 100-200 km in the zonal direction, bifurcation, secondary instabilities growing on the western walls of the primaries, and rates of development (see e.g., *Aveiro et al.* (2012)). Also, the simulated range-time-intensity map recovered the "C-shape" structures detected by fixed-beam coherent scatter radars such as the Jicamarca radar. However, the zonal drift of the irregularities seem to be slower than typical observations made by the Jicamarca radar, which may indicate an underestimation of the *F* region dynamo efficiency in the simulation. Simulations based on field-line integrated electrostatic potential using SAMI3 model showed irregularities drifting zonally approximatelly at the zonal wind speeds (*Huba and Joyce*, 2010). Their result suggests an overestimation of the dynamo efficiency due to the absence of secondary instabilities on the western walls of the *F* region plasma irregularities.

Using simulated plasma and empirical neutral atmosphere composition information, we computed the airglow emission for the 6300-(or O^+ red) line. A simulation of airglow observations by a hypothetical camera located a few degrees south of Jicamarca was performed. The results presented here show for the first time simulated ground-based airglow observations for the red line emission. Simulations of ground-based airglow measurements for the 5577-(or O^+ green) line were described by *Retterer* (2010) and showed bifurcation and tilting of *ESF* plasma irregularities. Strong emissions were observed on the western half of the image due to recombination during the earliest hours of the night and

again close to midnight, similar to what has been reported by *Makela and Miller* (2008). Intermediate scale (~ 30-50 km) irregularities were barely detectable during the first hours after sunset in the simulation; however, those do not seem to be observed in nature by airglow cameras. The comparison between the simulated radar scans (Figure 7.2) and airglow simulations (Figure 7.4) showed that details of the plasma irregularities has been lost and waveforms appeared distorted in airglow observations.

Magnetic perturbations parallel to the main field were mainly due to diamagnetic currents flowing on the external walls of the plasma depletions and transverse magnetic perturbations were mainly due to field-aligned currents. the simulated magnetic field perturbations show good qualitative with the CHAMP measurements. The ionospheric circulation results agreed with earlier simulations by *Aveiro et al.* (2011) based on CHAMP satellite data. Also, the simulation reproduces the main features of the plasma depletions as derived in a statistical study by *Park et al.* (2009), as e.g. upward (downward) currents on their external western (eastern) edges.

Overall, the diagnostic codes showed that the numerical simulation scheme described here is able to reproduce many of the most salient characteristics of ESF as observed by a number of different instruments. For the validation of current densities (or magnetic field perturbations), the computation of electrostatic potential must be done in 3-D. Quasi-three-dimensional simulations based on the equipotential field line approach do not provide parallel current information, and thus cannot be compared to satellite-borne magnetometer data; however, they can still be validated against backscatter radar data and airglow images. Validating simulations against specific observations is difficult since em-

pirical models do not capture day-to-day variability. Thus, simulations can be validated mainly in terms of their ability to reproduce the characteristic behavior of the plasma irregularities, e.g., tilting, spacing, layer thickness, altitude range, onset time, and rate of development.

CHAPTER 8

IMPLICATIONS OF THE EQUIPOTENTIAL FIELD LINE APPROXIMATION FOR EQUATORIAL SPREAD *F* ANALYSIS

There is a computer disease that anybody who works with computers knows about. It's a very serious disease and it interferes completely with the work. The trouble with computers is that you 'play' with them!

–Richard P. Feynman, in *Surely You're Joking, Mr. Feynman!*

8.1 Introduction

In this chapter, we evaluate the role of potential variations along the magnetic field and the parallel currents in ESF development. To evaluate how the current loops close in the presence of plasma depletions, we use three different approaches: analytical theory for a simplified ionosphere, numerical computation of the electrostatic potential for an idealized ionosphere, and initial boundary value simulations of ESF under realistic ionospheric conditions. The numerical studies are performed for both the equipotential field line approximation and the three-dimensional computation of the electrostatic potential. The main issue we address here is the degree to which it is possible to describe the ionospheric current circulation with the equipotential field line (EFL) approximation and how the approximation affects ESF simulations.

8.2 Analytical approach

The three-dimensional equation for the electrostatic potential (Φ) of a warm, single-ion plasma irregularity in a uniform magnetic field ($\mathbf{B} = B\hat{\mathbf{z}}$) and background neutral wind ($\mathbf{U} = U\hat{\mathbf{x}}$) is given by (*Drake et al.*, 1985):

$$\frac{1}{B}\nabla_\perp \cdot (n\nabla_\perp \Phi) + \frac{\nu_{in}}{\Omega_i}\frac{T}{eB}\nabla_\perp^2 n + \frac{\nu_{in}}{\Omega_i}\hat{\mathbf{z}} \times \mathbf{U} \cdot \nabla n + \frac{\partial}{\partial z}\left[\frac{ne}{m_e \nu_e}\left(\frac{\partial \Phi}{\partial z} - \frac{T}{ne}\frac{\partial n}{\partial z}\right)\right] = 0, \quad (8.1)$$

where ν_{in} and Ω_i are the ion collision frequency and gyrofrequency, respectively, and ν_e is the electron collision frequency. We assumed thermodynamical equilibrium ($T_e = T_i = T$). The terms $\mathbf{U}$ and B represent the wind velocity and magnetic field. Equation 1 neglects background electric fields, Hall terms, gravity, and ion parallel and electron perpendicular diffusion. We can define a plasma irregularity length along the magnetic field L_z such that $L_z = r_c(\Omega_e\Omega_i/\nu_e\nu_{in})^{1/2}$, where r_c is the radius of the circular irregularity in the perpencicular plane. The parallel diffusion is scaled to $\Gamma = 2T/eBUr_c$ and we obtain a residual potential of the form $\psi = [\Phi + T\ln(n)/e]/Br_cU$. The remaining dimesionless variables are $r_c\nabla_\perp \rightarrow \nabla_\perp$, $L_z\partial/\partial z \rightarrow \partial/\partial z$, and $n/n_b \rightarrow n$, where n_b represents the background density. With this new set of dimensionless variables, Equation 8.1 can be rewritten as (*Drake and Huba*, 1987)

$$\nabla \cdot [n\nabla_\perp \psi] + \frac{\partial n}{\partial y} - \Gamma\frac{\partial^2 n}{\partial z^2} = 0. \quad (8.2)$$

We examine the potential solution of a waterbag plasma irregularity which is a sphere of unity radius in the the dimensionless units, i.e., $n(r) = 1 + MH(1-r)$, where H is the Heaviside step function and the constant M represents the ratio $n(r)/n_b$ inside the sphere.

The potential is linearly separated into two parts ($\psi = \psi_a + \psi_w$): (a) the po-

larization potential (ψ_w) of the plasma due to the neutral winds and (b) the ambipolar potential (ψ_a) due to gradients in the plasma pressure.

The solution of the polarization potential in the drifting frame of reference is given by

$$\psi_w = \frac{M}{M+3} r \sin(\theta)\sin(\phi)(1 - r^{-3})H(r-1). \tag{8.3}$$

The solution of the ambipolar potential gives

$$\begin{aligned} \psi_a &= a_2^+ P_2(\cos\theta)/r^3, \qquad r > 1 \\ \psi_a &= a_0 + a_2^- P_2(\cos\theta)/r^2, \quad r < 1 \end{aligned} \tag{8.4}$$

where P_2 is the second-order Legendre polynomial and the coefficients are given by

$$\begin{aligned} a_2^+ &= -\Gamma\left[M + \frac{2}{3}(M+1)\ln(M+1)\right]/(M+\frac{5}{2}), \\ a_2^- &= -\Gamma\left[M - \ln(M+1)\right]/(M+\frac{5}{2}), \\ a_0^- &= (\Gamma/3)\ln(M+1). \end{aligned} \tag{8.5}$$

A similar set of solutions was derived by *Drake and Huba* (1987) for ionospheric plasma clouds and applied to plasma cloud stability studies. Here, we analyze the potential around a plasma irregularity elongated along the magnetic field direction. We assume a 90% depletion to the background density (M=-0.9) and compute the ambipolar and polarization potential.

Figure 8.1 (top left) shows the ambipolar potential in the y-z (vertical-parallel) plane and (top right) polarization potential in the x-y (zonal-vertical) plane for a spherical (in normalized coordinates) plasma irregularity embbedded in a homogeneous plasma. The ambipolar potential shows a quadrupole

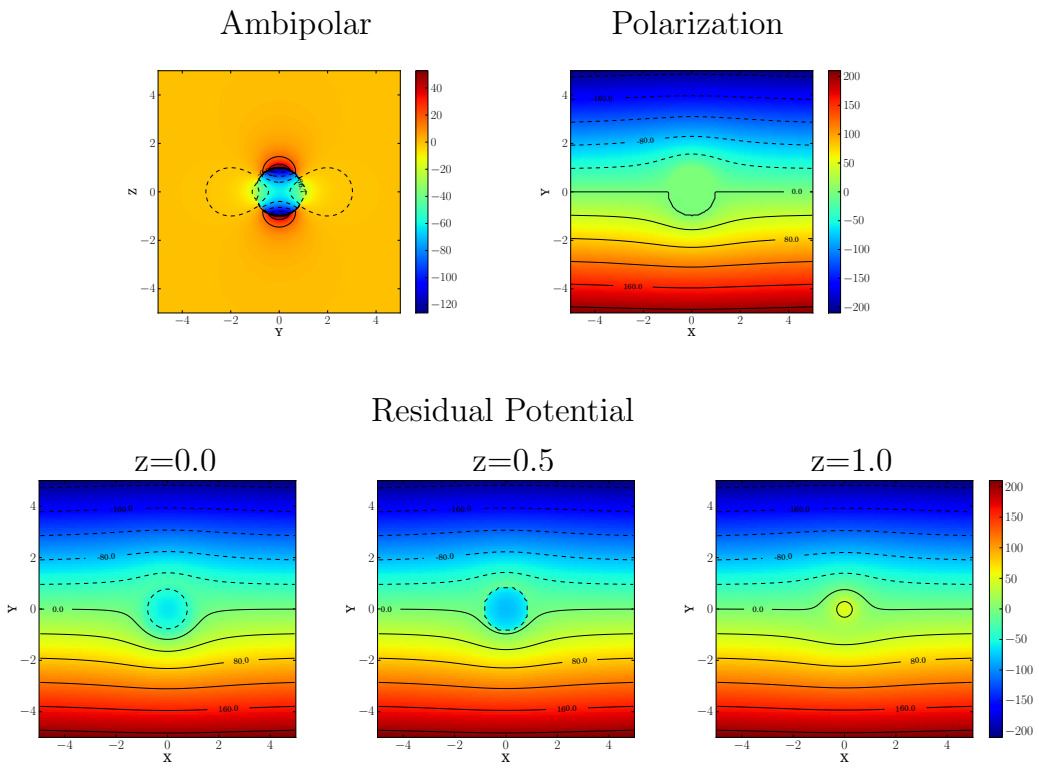

Figure 8.1: (Top) Ambipolar and polarization potential. (Bottom) Residual potential at three different latitudinal cuts: z=0.0, 0.5, and 1.0.

structure, with larger gradients along the magnetic field (z-direction). The polarization potential shows a dipolar structure with null potential inside the sphere in the frame of reference that moves with the plasma irregularity.

Figure 8.1 (bottom) depicts the combination of the two potentials into the residual potential in the x-y plane at three zonal cuts: z=0.0, 0.5, and 1.0. Variation in the residual potential inside and in the vicinity of the plasma irregularity along the magnetic field is evident. In a realistic ionosphere at *F*-region altitudes, the direct conductivity is 10^4–10^5 times larger than the Pedersen conductivity. Thus, even for small electric fields along **B**, parallel currents will present large amplitudes.

8.3 Numerical approach

Below, we solve the electrostatic potential using two different approaches: (a) equipotential field line assumption (EFL) and (b) full three-dimensional (3-D) solution. The model was constructed using tilted magnetic dipole coordinates (p, q, ϕ), where the tilt is matched to the magnetic declination in the longitude of interest. In our terminology, p represents the McIlwain parameter (L), q is the magnetic co-latitude, and ϕ is longitude (see Appendix A).

The EFL approach consist in using the fact that parallel conductivities are much larger than transverse terms and assume no variations in the electrostatic potential along **B**. The partial differential equation that describes the instantaneous behavior of the electrostatic potential based on the solenoidal current density ($\nabla \cdot \mathbf{J} = 0$) for the EFL approach is given by

$$\left(\frac{\partial}{\partial p}\Sigma_{Pp} + \frac{\partial}{\partial \phi}\Sigma_H\right)\frac{\partial \Phi}{\partial p} + \left(-\frac{\partial}{\partial p}\Sigma_H + \frac{\partial}{\partial \phi}\Sigma_{P\phi}\right)\frac{\partial \Phi}{\partial \phi} = \frac{\partial j_{0p}}{\partial p} + \frac{\partial j_{0\phi}}{\partial \phi} \tag{8.6}$$

where

$$\Sigma_{Pp} = \int \sigma_P \frac{h_p}{h_\phi} h_q d_q, \quad \Sigma_{P\phi} = \int \sigma_P \frac{h_\phi}{h_p} h_q d_q, \quad \Sigma_H = \int \sigma_H h_q d_q, \text{ and} \tag{8.7}$$

$$j_{0p} = \int J_{0p} h_\phi h_q d_q, \quad j_{0\phi} = \int J_{0\phi} h_p h_q d_q. \tag{8.8}$$

The partial differential equation obtained for the computation of the electrostatic potential in 3-D (also from $\nabla \cdot \mathbf{J} = 0$) is given by Equation 2.10. Both Equation 8.6 and Equation 2.10 are solved using the BiConjugate Gradient Stabilized (BiCGStab) method (e.g. *van der Vorst* (1992)) using the algorithms described by *Saad* (1990). The resultant current density is the combination of the background

($\mathbf{J}_0$), the polarization ($\hat{\Sigma} \cdot \nabla\Phi$), and the (divergence-free) diamagnetic ($\mathbf{J}_d$) current densities (i.e., $\mathbf{J} = \mathbf{J}_0 + \hat{\Sigma} \cdot \nabla\Phi + \mathbf{J}_d$).

To compute the potential, we derive plasma density and composition from the International Reference Ionosphere (IRI-007) Model (*Bilitza and Reinisch*, 2008), and neutral composition and temperature estimates from the Mass Spectrometer and Incoherent Scatter (NRL-MSISE00) model (*Picone et al.*, 2002). Zonal neutral winds are obtained from the Horizontal Wind Model (HWM-07) (*Drob*, 2008). We take the ionosphere and neutral atmosphere to be in thermodynamic equilibrium after sunset ($T_n = T_e = T_i$). The background electric field is specified and partly controls the forcing. The ion composition includes O^+, NO^+, and O_2^+. The simulation is cast on a rectangular grid 139×133×189 points wide in (p, q, ϕ) space constructed using a tilted magnetic dipole coordinate system. A cut through the equatorial plane spans altitudes between 90–510 km and longitudes between ± 6°. The flux tubes covered by the parallel coordinate all reach to the lower *E* region.

8.3.1 Solution for a cylindrical plasma depletion

Using a symmetrial ionosphere in relation to the magnetic equator, we compute the background ionospheric conditions. Figure 8.2 shows the electrostatic potential results for the EFL (middle panels) and full 3-D solution (bottom panels). Panels on the left indicate transverse currents, and meridional currents are displayed on the right. The top panels depict electron density in (left) transverse and (right) meridional cuts.

The electrostatic potential obtained using the equipotential field line ap-

proach showed vertical currents on the bottomside of the *F* region. Above the bottomside, gravity-driven and Pedersen currents flow eastward. Residual field-aligned currents due to gradients in the electron density along the magnetic field flow equatorward at the topside and poleward near the *F* peak.

The bottom panels of Figure 8.2 show the electrostatic potential computed using the full 3-D solution. Again, gravity-driven and Pedersen currents exist above the bottomside, but large vertical currents flowing from the bottomside to the *F* peak dominate the scenario. The meridional current panel shows that the vertical currents are partially supplied by equatorward currents connecting the *F* region bottomside to the off-equatorial *E* region. In order to close the loop, poleward currents connect the topside to the low latitude ionosphere.

Using the same initially symmetric ionosphere, we added a cylindrical plasma irregularity aligned with the magnetic field and computed the electrostatic potential (Figure 8.3). In the transverse plane for both the EFL and 3-D solutions, the zonal electric field is enhanced inside the irregularity. Diamagnetic currents flowing around the plasma depletion are evident. The main difference is in the meridional plane, where the 3-D solution shows a complicated current system flowing poleward (equatorward) at the bottom (upper) edge of the plasma depletion. At the meridional borders of the irregularity, a competition between ambipolar currents and parallel currents are evident. In the EFL scenario, only localized ambipolar currents are detected at the meridional edges of the irregularities.

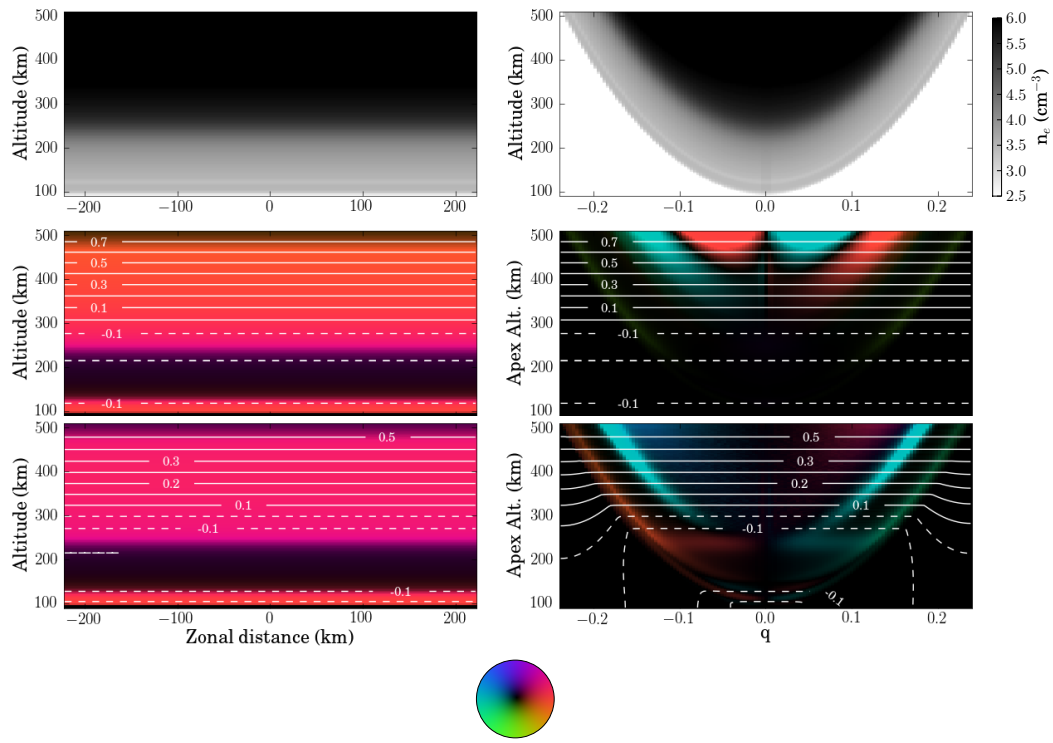

Figure 8.2: Top: Plasma number density in two cuts: (left) transverse cut at the magnetic equator and (right) meridional cut at the center of the zonal grid. Middle: Transverse current density in the equatorial plane for the EFL approach with equipotential contours (in kV) superimposed in white. Middle right: current density in the meridional plane. Bottom and bottom right: same as middle panel but for the full 3-D solution. The current densities are vector quantities with magnitudes and directions indicated by the color wheel at the bottom. The maximum scale is 3 nA/m^2 in the equatorial plane and 30 nA/m^2 in the meridional plane.

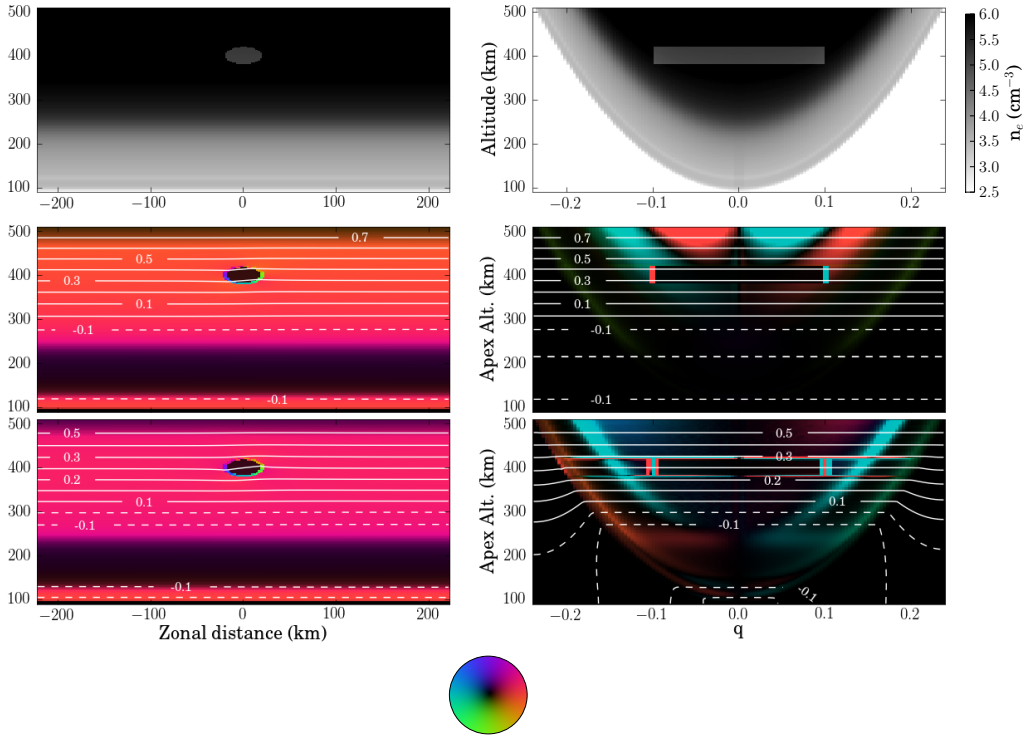

Figure 8.3: Same as Figure 2, but for a cylindrical shape irregularity aligned along **B**.

8.3.2 Initial boundary-value simulation

Next, we consider an initial boundary-value simulation applied to a realistic ionosphere. The runs shown below are centered on the dip equator near Kwajalein (5.5° N latitude, 166.5° E longitude, 7.4° declination) with background conditions modeled for August 11, 2004. To seed the simulation run, we added independent Gaussian white noise to the initial number density. We solve a discretized version of the continuity equation for each ion species using a monotone upwind scheme for conservation laws (MUSCL) (a review can be found in *Trac and Pen* (2003)) directly applicable to the ion continuity problem (see Appendix B). The characteristic of the neutral atmosphere (densities, temperature,

and wind velocity) are updated in time on the basis of inputs from climatological models.

Figure 8.4 shows the results for the (left) EFL approximation and (right) the 3-D solution. The time evolution of the simulation (for t=0h30, 1h15, and 2h00 after an initial t_0=0.25 UT) is organized from top to bottom.

The top panel of Figure 8.4 depicts the evolution of ionospheric irregularities due to the collisional shear instability (CSI) (*Hysell and Kudeki*, 2004; *Kudeki et al.*, 2007). The spatial scales of the irregularities forming at the base of the bottomside range between 30–50 km. These irregularities cannot undergo vertical development and remain confined to altitudes where the plasma flow is retrograde.

By the time of the second panel in Figure 8.4 (t_0+1h), the transient phase of the CSI was ending, and the asymptotic phase was underway. In the EFL approximation, the plasma flows nearly at the neutral speed and the irregularities are damped by diffusion. In the 3-D solution, the 30–50 km waves at the base of the bottomside coalesced into large-scale waves with scale sizes between 100-200 km. Under the action of the background zonal electric field, the bottomside irregularities start to exhibit vertical development.

In the final panel of the the 2-D solution, damping of the irregularities by diffusion is still observed. In the 3-D solution, the irregularities penetrate to the topside where gravity-driven currents can contribute further to growth. Some of the original intermediate scale structure from the first panel in the simulation survives, contributing to the overall fine structure. Bifurcation is evident, as well as secondary instabilities growing mainly on the western walls of the

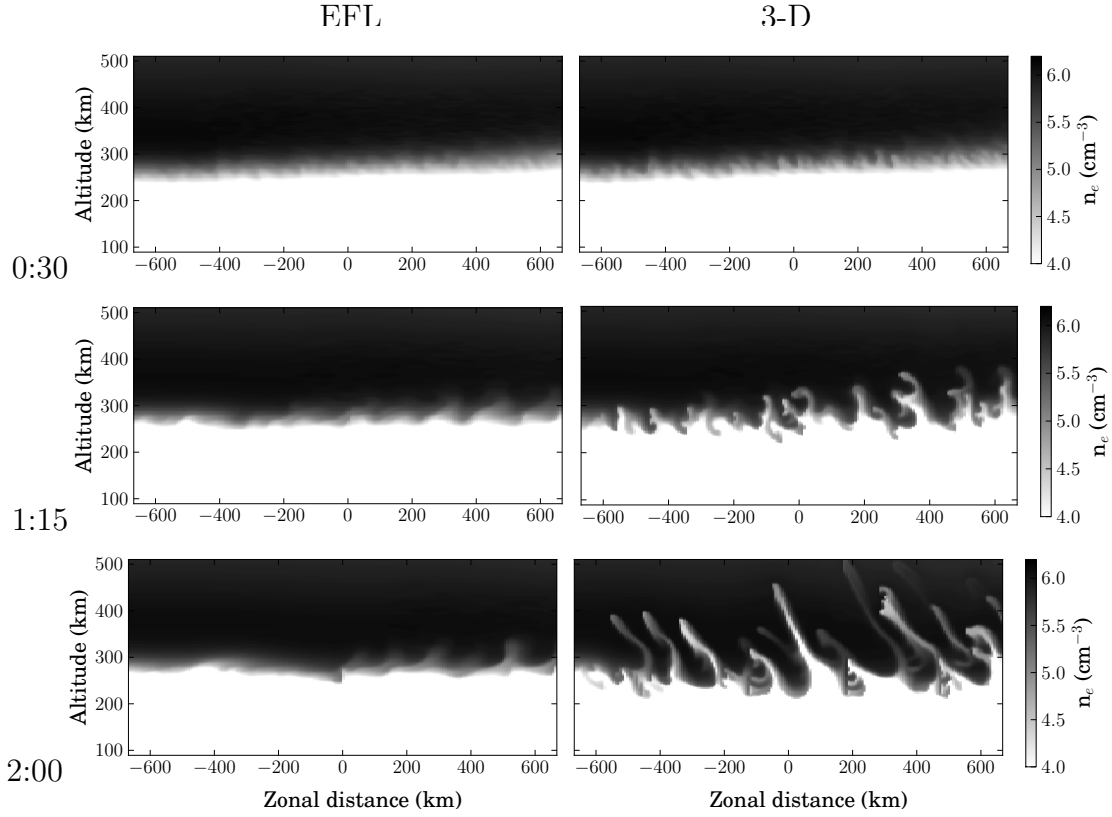

Figure 8.4: Simulated plasma densities in a cut through the latitudinal plane. The four panels show results for simulation times of 0h30m, 1h15m, and 2h00, respectively, after a start time t_0 = 0:25 UT (LT = UT - 11 hr at the horizontal center of the simulation).

primaries. Some descending, wedge-shaped plasma enhancements accompany the ascending depletions.

8.4 Summary

Three different approaches have been used to evaluate the role of the parallel currents in equatorial spread *F*. Using an idealized ionosphere, analytical re-

sults show that parallel electric fields (and currents) are an inherent feature of ionosphere flows. In the second approach, we computed the background current circulation in a simplified ionosphere both with and without irregularity. One of the main results is the inability of the equipotential field line approximation to describe the three-dimensional structure of the currents. The EFL approach underestimates the vertical current flowing through the equatorial *F* region. Our final approach used an initial boundary value simulations in a realistic postsunset equatorial *F* region ionosphere. The result show that the supression of the vertical current flowing throughout the *F* region and associated differential speed between ions and neutrals seemed to play a major role in the underestimation of the growth rate of equatorial spread *F* irregularities in the numerical simulations based on the EFL approximation.

CHAPTER 9

CONCLUSIONS AND FUTURE STUDIES

I can live with doubt, and uncertainty, and not knowing. I think it's much more interesting to live not knowing than to have answers which might be wrong.

–Richard P. Feynman, in *The pleasure of finding things out*

This dissertation described a series of numerical studies of plasma density irregularities in the post-sunset ionosphere applied to the equatorial spread *F* (ESF) problem. The model is valid for the ionosphere in the collisional regime and uses the electrostatic approximation, i.e., it does not support electromagnetic wave modes, as e.g. Alfvén waves.

A comparative analysis of three-dimensional and quasi-three-dimensional (using field line-integrated quantities) approaches showed that the latter is unable to describe the three-dimensional structure of the ionospheric currents accurately. The quasi-three-dimensional approximation underestimates the vertical current flowing throughout the equatorial *F* region and leads to an underestimation of the growth rate of equatorial spread *F* irregularities in numerical simulations. The results suggest that an upgrade of the quasi-three-dimensional models, as e.g. SAMI3 (*Huba et al.*, 2008) and PBMOD (*Retterer*, 2010), may lead to an improvement of their equatorial spread *F* forescasting capabilities.

The results of the 3-D numerical simulations showed that the combination of the generalized Rayleigh-Taylor and the collisional shear instabilities produced growing waveforms with characteristics matching satellite, airglow camera, and radar observations, as e.g. tilting, spacing, layer thickness, altitude range, onset time, and rate of development. The transient response of CSI explains rapid in-

termediate (~30 km) scale wave emergence at the base of the *F* region, whereas the steady-state behavior seems to account for the large (100+ km) scale waves that ultimately dominated. The three different types of ESF (bottom-type, bottomside, and topside) appeared to be a result of the time sequencing of the transient and steady-state response of CSI in relation to the zonal electric field. The comparison between the simulated radar scans and airglow emission for the 6300-(or O^+ red) line showed that details of the plasma irregularities are lost and waveforms are distorted in airglow observations. The analysis of the magnetic perturbations parallel to the main field showed that they are mainly due to diamagnetic currents flowing on the external walls of the plasma depletions and that transverse magnetic perturbations are mainly due to field-aligned currents. The simulated magnetic field perturbations reproduced the main features of the plasma depletions as derived in a statistical study by *Park et al.* (2009), as e.g. upward (downward) currents on their external western (eastern) edges. That the simulation is electrostatic argues against an Alfvénic interpretation of all of the CHAMP magnetic field observations in ESF.

As mentioned in the Introduction chapter, the studies presented in the dissertation supply hints towards a better understanding of the phenomenology behind ESF, but they do not provide a final explanation for questions like: what triggers topside ESF? My interpretation is given as follows. Large upward vertical currents are commonly detected between 1700–2100 LT (*Park et al.*, 2010), indicating that the plasma drifts slower than the neutrals in the zonal direction. The differential speed between plasma and neutrals during the earliest hours after sunset has been confirmed by the comparison between thermospheric wind observations made by Fabry-Perot and plasma drifts observations made by the Jicamarca radar (John Meriwether, personal communication, March 13, 2012).

After ~ 2100 LT, the low latitude *E* region conductivity becomes very small and the layer does not behave as an efficient load for the *F* region dynamo. This leads to a reduction of both the vertical currents and the differential velocity between plasma and neutrals. If the eastward electric field was very intense during the hours preceding the reduction in the vertical currents, collisional shear instability-driven irregularities will be propelled (upward) from the bottomside to the topside of the *F* region. If the plasma irregularities are still confined to the bottomside of the *F* region after the ceasing of the vertical currents, the collisional shear instability becomes inoperative and the plasma irregularities will be damped. In this interpretation, topside irregularities will occurr whenever there is a good temporal match between significant eastward electric fields and upward vertical currents with the appearance of plasma irregularities at the bottomside of the *F* region.

Then, what controls the day-to-day variability of topside spread *F*? Or what seeds it? One of the proposed mechanisms is the large-scale perturbation of plasma density at the postsunset *F* region bottomside due to gravity waves (*Röttger*, 1973; *Kelley et al.*, 1981; *Singh et al.*, 1997; *McClure et al.*, 1998). Since gravity waves are not directly measured in the ionosphere, this hypothesis is difficult to be tested experimentally. Numerical simulations have shown that gravity waves can penetrate into the lower thermosphere, however the associated horizontal wavelengths for the surviving waves was about 50–150 km, which does not favor the scales of the plasma perturbations observed in the *F* region bottomside (~30 km or the 200+ km) at Jicamarca and Kwajalein.

The numerical simulations analyzed throughout the dissertation were seeded by adding independent Gaussian white noise to the initial number den-

sity. In the ionosphere, those perturbations may be caused by a number of sources, as e.g. plasma waves or deposition of metallic ions by meteor ablation. That the simulation did not include any perturbations to the wind fields argues against the idea that gravity waves are required to seed ESF. Moreover, the day-to-day variability of topside ESF may be connected to variations in the low-latitude *E* region characteristics. The largely variable neutral wind motions (see e.g. *Larsen* (2002)) added to local enhancements of the electron density (known as sporadic *E* layers) at low-latitudes may change the background circulation and control the growth of the CSI, the primary process behind topside ESF. This scenario can be tested using the numerical model presented in the dissertation. If this proves to be true, new strategies may be designed for topside ESF forecasting, as e.g. operation of a radar network along the magnetic meridian for multi-latitudinal ionospheric sounding.

Finally, a list of future studies is described:

- *E* region irregularities: the 3-D numerical model presented here for the study of equatorial *F* region plasma irregularities is very robust. Initial analysis has shown that the model can be applied to simulations of plasma irregularities in the equatorial electrojet, the (unnamed) upper *E* region echoes (~130 km), and mid-latitude quasi-periodic echoes;
- global current circulation in 3-D: the ionospheric dynamo has been investigated by several quasi-three-dimensional ionospheric models, as e.g., the Thermosphere Ionosphere Mesosphere Electrodynamic General Circulation Model (TIME-GCM) (*Roble and Ridley*, 1994) and SAMI3 (Sami3 is Also a Model of the Ionosphere) (*Huba et al.*, 2008). As shown in the previous chapters, only 3-D models provide a good description of the currents in

the ionosphere. Thus, the implementation of 3-D ionospheric potential solvers would show, for the first time, how the dynamo currents close, leading to a better understanding of the current circulation throughout the low-latitude ionosphere;

- large-scale perturbations at the bottomside of the *F* region and gravity waves (GWs): the predominance of large-scale waves in the the postsunset equatorial ionosphere has been attributed to GWs (*Röttger*, 1973; *Kelley et al.*, 1981; *Singh et al.*, 1997; *McClure et al.*, 1998). Initial studies of those large-scale perturbations have been performed using a 3-D numerical model and have shown that those waves can be recovered with no need to cast GW-like perturbations to the background (tidal) neutral winds if appropriate initial conditions are set in the simulation (not shown here). Also, the role of the GWs may be assessed by the 3-D model if realistic wind fields can be specified;

- triggering of ESF by Mesoscale Traveling Ionospheric Disturbances (MSTIDs): numerical studies using a quasi-three-dimensional ionospheric model (SAMI3) show that when the MSTID affects affects the low latitude ionosphere that is mapped along the magnetic field lines to the bottomside of the equatorial *F* (i.e., same L-shell), the disturbances may trigger ESF (*Krall et al.*, 2011). Since the process envolves the propagation of perturbations along the magnetic field lines, parallel currents may play a major role. Therefore, quasi-three-dimensional models do not seem to be adequate to assess the ESF triggering by MSTIDs, but full 3-D models (as the one described in the dissertation) should be;

- magnetic pressure effects: magnetic pressure is often neglected in the force balance equation studies since the plasma beta ($\beta \equiv \frac{n\kappa_b T}{B^2/2\mu_o}$) is much smaller

than unity for normal ionospheric conditions. The numerical studies of the magnetic field perturbations in Chapter 5 and Chapter 6 showed variations of ~ 1 nT over length scales of a few kilometers in the transverse direction during equatorial spread *F*. The inclusion of the magnetic pressure forcing term in Equation 2.2 may shed some light on unexplained magnetic perturbations, as e.g. reports of double peaks in the parallel direction on the walls of ESF plasma irregularities (Robert Pfaff, personal communication, March 12, 2012);

- forecast assessment of ESF using satellite-borne magnetometers: *Park et al.* (2010)) describes a comprehensive study of *F* region vertical currents infered by CHAMP magnetometer observations. They report local time variations of the vertical current for the equinoxes and June and December solstices. Although not addressed in their paper, an analysis of the upward vertical current time span (Figure 3 in *Park et al.* (2010)) indicates a high correlation with the statistical observations of ESF in the Peruvian sector (see Chapter 3). Since the growth rate of the primary mechanism behind ESF, the collisional shear instability, is proportional to the vertical current flowing upward throughout the equatorial *F* region during the postsunset hours, such a relationship is intuitive. Thus, a detailed study may be performed to assess the use of satellite-borne magnetometer data for ESF forecasting.

APPENDIX A

DIPOLE COORDINATE SYSTEM

The model was constructed using tilted magnetic dipole coordinates (p, q, ϕ). The tilt is matched to the magnetic declination in the zone of interest (D). In our terminology, p is the McIlwain parameter (L), q is a coordinate parallel to the magnetic field, and ϕ is the longitude. Following *Huba et al.* (2000), the axis of a magnetic dipole coordinate system are given by:

$$p = \frac{r_e}{R}\frac{1}{\sin^2\theta_e}, \tag{A.1}$$

$$q = \frac{R^2}{r_e^2}\cos\theta_e, \tag{A.2}$$

$$\phi = \phi_e, \tag{A.3}$$

where R is the Earth's radius. The terms with the subscripts "e" represent spherical eccentric coordinates and can be computed using the following expression:

$$q^2\left(\frac{r_e}{R}\right)^4 + \frac{1}{p}\left(\frac{r_e}{R}\right) = 1. \tag{A.4}$$

The geographic latitude (x), longitude (y), and altitude (z) are obtained from

$$x = t_0 + (\pi/2 - \theta_e)\cos(D) - \cos(t_0)\phi_e\sin(D), \tag{A.5}$$

$$y = p_0 + \phi_e\cos(D) + (\pi/2 - \theta_e)\sin(D)/\cos(t_0), \tag{A.6}$$

$$z = R + r_e. \tag{A.7}$$

where t_0 and p_0 are the geographic latitude and longitude at the center of the simulation. For instance, $t_0 = -12.20°$ and $p_0 = 283.15°$ at the Jicamarca Radio Observatory, Peru. Additional conversion from geocentric to geodetic coordinates can be applied to altitudes and latitudes.

Finally, the curvilinear factors for a magnetic dipole coordinate system are given by:

$$h_p = \frac{r_e^3}{R^3} \frac{1}{(1 + 3\cos^2\theta_e)^{1/2}}, \tag{A.8}$$

$$h_q = \frac{R \sin^3\theta_e}{(1 + 3\cos^2\theta_e)^{1/2}}, \tag{A.9}$$

$$h_\phi = r_e \sin\theta. \tag{A.10}$$

APPENDIX B

TRANSPORT SCHEME

Following *Trac and Pen* (2003), the 1-D scalar continuity equation in vector differential form is expressed as

$$\frac{\partial n}{\partial t} + \frac{\partial F}{\partial x} = 0, \tag{B.1}$$

where F represents the flux term and is defined as nv. The discretized solution for the cell-averaged quantity n is given by:

$$n_i^{t+\Delta t} = n_i^t - \left(\frac{F_{i+1/2}^t - F_{i-1/2}^t}{\Delta x} \right) \Delta t. \tag{B.2}$$

Using a first-order upwind flux assigment, given as:

$$F_{i+1/2}^t = \begin{cases} F_i^t & \text{if } v > 0 \\ F_{i+1}^t & \text{if } v < 0 \end{cases} \tag{B.3}$$

and second-order flux corrections, given as:

$$\Delta F_{i+1/2}^{L,t} = \begin{cases} \frac{F_i^t - F_{i-1}^t}{2} & \text{if } v > 0 \\ -\frac{F_{i+1}^t - F_i^t}{2} & \text{if } v < 0 \end{cases} \tag{B.4}$$

and

$$\Delta F_{i+1/2}^{R,t} = \begin{cases} \frac{F_{i+1}^t - F_i^t}{2} & \text{if } v > 0 \\ -\frac{F_{i+2}^t - F_{i+1}^t}{2} & \text{if } v < 0 \end{cases} \tag{B.5}$$

which means that if the advective velocity is positive we make our evaluation at the neighboors of i cell, otherwise (if negative), around $i + 1$ cell. A flux limiter ϕ is imposed to the second order corrections in the form:

$$F_{i+1/2}^t = \phi(\Delta F_{i+1/2}^{L,t}, \Delta F_{i+1/2}^{R,t}) \tag{B.6}$$

.

The second-order correction when added to the first-order upwind scheme is called *Monotone Upwind Scheme for Conservation Laws* (MUSCL) (*Trac and Pen*, 2003). In the studies presented here, either superbee or sweby flux limiter were implemented and used. The sweby limiter chooses between the larger correction and β times the smaller correction, where $1 \leq \beta \leq 2$ (*Sweby*, 1984). The superbee limiter represent the special case when $\beta = 2$ (*Roe*, 1986).

Finally, a second-order Runge-Kutta is used for time integration of the conservation law in two parts:

- first, a half-step iteration with first-order upwind scheme

$$n_i^{t+\Delta t/2} = n_i^t - \left(\frac{F_{i+1/2}^t - F_{i-1/2}^t}{\Delta x} \right) \frac{\Delta t}{2}, \tag{B.7}$$

- second, a full time sted with MUSCL

$$n_i^{t+\Delta t} = n_i^t - \left(\frac{F_{i+1/2}^{t+\Delta t/2} - F_{i-1/2}^{t+\Delta t/2}}{\Delta x} \right) \Delta t. \tag{B.8}$$

APPENDIX C

SYSTEM OF EQUATIONS

1. Consider the steady state force equation:

$$0 = n_\alpha q_\alpha(\mathbf{E} + \mathbf{v}_\alpha \times \mathbf{B}) - \kappa_B T_\alpha \nabla n_\alpha + n_\alpha m_\alpha[\mathbf{g} - \sum_{\beta \neq \alpha} \nu_\alpha(\mathbf{v}_\alpha - \mathbf{v}_\beta)] \tag{C.1}$$

First, I will change the coordinate system to the wind frame, where $\mathbf{v}_{\alpha\mathbf{n}} = \mathbf{v}_\alpha - \mathbf{U}$ and $\mathbf{E_n} = \mathbf{E} + \mathbf{U} \times \mathbf{B}$ are in the wind frame. $\mathbf{E}$ and $\mathbf{U} \times \mathbf{B}$ are measured with respect to the Earth's frame.

$$0 = n_\alpha q_\alpha(\mathbf{E} + \mathbf{v}_\alpha \times \mathbf{B}) - \kappa_B T_\alpha \nabla n_\alpha + n_\alpha m_\alpha[\mathbf{g} - \sum_{\beta \neq \alpha} \nu_\alpha(\mathbf{v}_\alpha - \mathbf{v}_\beta)] \tag{C.2}$$

$$0 = n_\alpha q_\alpha[\mathbf{E_n} - \mathbf{U} \times \mathbf{B} + (\mathbf{v}_{\alpha\mathbf{n}} + \mathbf{U}) \times \mathbf{B}] - \kappa_B T_\alpha \nabla n_\alpha + n_\alpha m_\alpha[\mathbf{g} - \sum_{\beta \neq \alpha} \nu_\alpha(\mathbf{v}_\alpha - \mathbf{v}_\beta)] \tag{C.3}$$

$$0 = n_\alpha q_\alpha[\mathbf{E_n} - \mathbf{U} \times \mathbf{B} + \mathbf{v}_{\alpha\mathbf{n}} \times \mathbf{B} + \mathbf{U} \times \mathbf{B}] - \kappa_B T_\alpha \nabla n_\alpha + n_\alpha m_\alpha \mathbf{g} - n_\alpha m_\alpha \sum_{\beta \neq \alpha} \nu_\alpha(\mathbf{v}_\alpha - \mathbf{v}_\beta) \tag{C.4}$$

Using the condition of $n_\alpha \ll n_n \Rightarrow \nu_{ei} \ll \nu_{e,in}$:

$$0 = n_\alpha q_\alpha \mathbf{E_n} + n_\alpha q_\alpha \mathbf{v}_{\alpha\mathbf{n}} \times \mathbf{B} - \kappa_B T_\alpha \nabla n_\alpha + n_\alpha m_\alpha \mathbf{g} - n_\alpha m_\alpha \nu_\alpha(\mathbf{v}_\alpha - \mathbf{U}) \tag{C.5}$$

$$0 = n_\alpha q_\alpha \mathbf{E_n} + n_\alpha q_\alpha \mathbf{v}_{\alpha\mathbf{n}} \times \mathbf{B} - \kappa_B T_\alpha \nabla n_\alpha + n_\alpha m_\alpha \mathbf{g} - n_\alpha m_\alpha \nu_\alpha \mathbf{v}_{\alpha\mathbf{n}} \tag{C.6}$$

2. Now, we use Eqn. C.6 to derive the perpendicular velocity component, $\mathbf{v}_{\alpha\mathbf{n}\perp}$ and $\mathbf{v}_{\alpha\mathbf{n}\parallel}$. $\Omega_\alpha = \frac{q_\alpha|\mathbf{B}|}{m_\alpha}$ is a gyrofrequency of the species α and $\hat{\mathbf{b}} = \mathbf{B}/|\mathbf{B}|$. $d_\alpha = \frac{\kappa_B T_\alpha}{m_\alpha \nu_\alpha}$ is a parallel diffusion coefficient.

$$0 = n_\alpha q_\alpha \mathbf{E}_\mathbf{n} + n_\alpha q_\alpha \mathbf{v}_{\alpha\mathbf{n}} \times \mathbf{B} - \kappa_B T_\alpha \nabla n_\alpha + n_\alpha m_\alpha \mathbf{g} - n_\alpha m_\alpha \nu_\alpha \mathbf{v}_{\alpha\mathbf{n}} \tag{C.7}$$

$$n_\alpha(q_\alpha \mathbf{v}_{\alpha\mathbf{n}} \times \mathbf{B} - m_\alpha \nu_\alpha \mathbf{v}_{\alpha\mathbf{n}}) = \kappa_B T_\alpha \nabla n_\alpha - n_\alpha m_\alpha \mathbf{g} - n_\alpha q_\alpha \mathbf{E}_\mathbf{n} \tag{C.8}$$

We take "$\times\hat{\mathbf{b}}$" on both sides:

$$n_\alpha(q_\alpha \mathbf{v}_{\alpha\mathbf{n}} \times \mathbf{B} - m_\alpha \nu_\alpha \mathbf{v}_{\alpha\mathbf{n}}) \times \hat{\mathbf{b}} = (\kappa_B T_\alpha \nabla n_\alpha - n_\alpha m_\alpha \mathbf{g} - n_\alpha q_\alpha \mathbf{E}_\mathbf{n}) \times \hat{\mathbf{b}} \tag{C.9}$$

$$n_\alpha[q_\alpha|\mathbf{B}|(-\mathbf{v}_{\alpha\mathbf{n}} + \mathbf{v}_{\alpha\mathbf{n}\parallel}) - m_\alpha \nu_\alpha \mathbf{v}_{\alpha\mathbf{n}} \times \hat{\mathbf{b}}] = (\kappa_B T_\alpha \nabla n_\alpha - n_\alpha m_\alpha \mathbf{g} - n_\alpha q_\alpha \mathbf{E}_\mathbf{n}) \times \hat{\mathbf{b}} \tag{C.10}$$

$$-n_\alpha(q_\alpha|\mathbf{B}|\mathbf{v}_{\alpha\mathbf{n}\perp} + m_\alpha \nu_\alpha \mathbf{v}_{\alpha\mathbf{n}} \times \hat{\mathbf{b}}) = (\kappa_B T_\alpha \nabla n_\alpha - n_\alpha m_\alpha \mathbf{g} - n_\alpha q_\alpha \mathbf{E}_\mathbf{n}) \times \hat{\mathbf{b}} \tag{C.11}$$

Noting that $\mathbf{v}_{\alpha\mathbf{n}} \times \hat{\mathbf{b}} = \mathbf{v}_{\alpha\mathbf{n}\perp} \times \hat{\mathbf{b}}$, we obtain:

$$q_\alpha|\mathbf{B}|\mathbf{v}_{\alpha\mathbf{n}\perp} + m_\alpha \nu_\alpha \mathbf{v}_{\alpha\mathbf{n}\perp} \times \hat{\mathbf{b}} = \left(-\kappa_B T_\alpha \frac{\nabla n_\alpha}{n_\alpha} + m_\alpha \mathbf{g} + q_\alpha \mathbf{E}_\mathbf{n}\right) \times \hat{\mathbf{b}} \tag{C.12}$$

$$m_\alpha(\Omega_\alpha \mathbf{v}_{\alpha\mathbf{n}\perp} + \nu_\alpha \mathbf{v}_{\alpha\mathbf{n}\perp} \times \hat{\mathbf{b}}) = \left(-\kappa_B T_\alpha \frac{\nabla n_\alpha}{n_\alpha} + m_\alpha \mathbf{g} + q_\alpha \mathbf{E}_\mathbf{n}\right) \times \hat{\mathbf{b}} \tag{C.13}$$

$$\Omega_\alpha \mathbf{v}_{\alpha\mathbf{n}\perp} + \nu_\alpha \mathbf{v}_{\alpha\mathbf{n}\perp} \times \hat{\mathbf{b}} = \left(-d_\alpha \nu_\alpha \frac{\nabla n_\alpha}{n_\alpha} + \mathbf{g} + \frac{\Omega_\alpha}{|\mathbf{B}|}\mathbf{E}_\mathbf{n}\right) \times \hat{\mathbf{b}} \tag{C.14}$$

Defining $\mathbf{A}$ as the right hand side of Eqn. C.14, we have:

$$\Omega_\alpha \mathbf{v}_{\alpha \mathbf{n}_\perp} + \nu_\alpha \mathbf{v}_{\alpha \mathbf{n}_\perp} \times \hat{\mathbf{b}} = \mathbf{A} \tag{C.15}$$

Separating the $\hat{\mathbf{x}}$ and $\hat{\mathbf{y}}$ directions and noting that $\mathbf{v}_{\alpha \mathbf{n}_\perp} \times \hat{\mathbf{b}} = v_{\alpha n y}\hat{\mathbf{x}} - v_{\alpha n x}\hat{\mathbf{y}}$, $\mathbf{A} = A_x\hat{\mathbf{x}} + A_y\hat{\mathbf{y}}$ (since A_z is null), and $\mathbf{A} \times \hat{\mathbf{b}} = A_y\hat{\mathbf{x}} - A_x\hat{\mathbf{y}}$, where $\hat{\mathbf{x}} \times \hat{\mathbf{y}} = \hat{\mathbf{b}}$, we obtain the linear system of equations:

$$\Omega_\alpha v_{\alpha n x} + \nu_\alpha v_{\alpha n y} = A_x$$
$$\Omega_\alpha v_{\alpha n y} - \nu_\alpha v_{\alpha n x} = A_y$$

Solving it, we obtain:

$$v_{\alpha n x} = \frac{\Omega_\alpha A_x - \nu_\alpha A_y}{\Omega_\alpha^2 + \nu_\alpha^2}$$
$$v_{\alpha n y} = \frac{\Omega_\alpha A_y + \nu_\alpha A_x}{\Omega_\alpha^2 + \nu_\alpha^2}$$

So:

$$\mathbf{v}_{\alpha \mathbf{n}_\perp} = \hat{\mathbf{x}}\frac{\Omega_\alpha A_x - \nu_\alpha A_y}{\Omega_\alpha^2 + \nu_\alpha^2} + \hat{\mathbf{y}}\frac{\Omega_\alpha A_y + \nu_\alpha A_x}{\Omega_\alpha^2 + \nu_\alpha^2} \tag{C.16}$$

$$\mathbf{v}_{\alpha \mathbf{n}_\perp} = \frac{\Omega_\alpha (A_x\hat{\mathbf{x}} + A_y\hat{\mathbf{y}})}{\Omega_\alpha^2 + \nu_\alpha^2} + \frac{\nu_\alpha (A_x\hat{\mathbf{y}} - A_y\hat{\mathbf{x}})}{\Omega_\alpha^2 + \nu_\alpha^2} \tag{C.17}$$

$$\mathbf{v}_{\alpha\mathbf{n}\perp} = \frac{\Omega_\alpha}{\Omega_\alpha^2 + \nu_\alpha^2}\mathbf{A} + \frac{\nu_\alpha}{\Omega_\alpha^2 + \nu_\alpha^2}\mathbf{A} \times \hat{\mathbf{b}} \tag{C.18}$$

Substituting **A**:

$$\mathbf{v}_{\alpha\mathbf{n}\perp} = \frac{\Omega_\alpha}{\Omega_\alpha^2 + \nu_\alpha^2}\left(-d_\alpha \nu_\alpha \frac{\nabla n_\alpha}{n_\alpha} + \mathbf{g} + \frac{\Omega_\alpha}{|\mathbf{B}|}\mathbf{E}_\mathbf{n}\right) \times \hat{\mathbf{b}} + \frac{\nu_\alpha}{\Omega_\alpha^2 + \nu_\alpha^2}\left(-d_\alpha \nu_\alpha \frac{\nabla n_\alpha}{n_\alpha} + \mathbf{g} + \frac{\Omega_\alpha}{|\mathbf{B}|}\mathbf{E}_\mathbf{n}\right) \times \hat{\mathbf{b}} \times \hat{\mathbf{b}}$$

$$\mathbf{v}_{\alpha\mathbf{n}\perp} = \frac{\Omega_\alpha}{\Omega_\alpha^2 + \nu_\alpha^2}\left(-d_\alpha \nu_\alpha \frac{\nabla n_\alpha}{n_\alpha} + \mathbf{g} + \frac{\Omega_\alpha}{|\mathbf{B}|}\mathbf{E}_\mathbf{n}\right) \times \hat{\mathbf{b}} + \frac{\nu_\alpha}{\Omega_\alpha^2 + \nu_\alpha^2}\left(-d_\alpha \nu_\alpha \frac{\nabla n_\alpha}{n_\alpha} + \mathbf{g} + \frac{\Omega_\alpha}{|\mathbf{B}|}\mathbf{E}_\mathbf{n}\right)_\perp \tag{C.19}$$

$$\begin{aligned}\mathbf{v}_{\alpha\mathbf{n}\perp} = \frac{\Omega_\alpha \nu_\alpha}{|\mathbf{B}|(\Omega_\alpha^2 + \nu_\alpha^2)}(\mathbf{E} + \mathbf{U} \times \mathbf{B})_\perp + \frac{\Omega_\alpha^2}{|\mathbf{B}|(\Omega_\alpha^2 + \nu_\alpha^2)}(\mathbf{E} + \mathbf{U} \times \mathbf{B}) \times \hat{\mathbf{b}} \\ - \frac{\nu_\alpha^2}{\Omega_\alpha^2 + \nu_\alpha^2} d_\alpha \frac{\nabla_\perp n_\alpha}{n_\alpha} - \frac{\Omega_\alpha \nu_\alpha}{\Omega_\alpha^2 + \nu_\alpha^2} d_\alpha \frac{\nabla n_\alpha \times \hat{\mathbf{b}}}{n_\alpha} \\ + \frac{\nu_\alpha}{\Omega_\alpha^2 + \nu_\alpha^2}\mathbf{g}_\perp + \frac{\Omega_\alpha}{\Omega_\alpha^2 + \nu_\alpha^2}\mathbf{g} \times \hat{\mathbf{b}}\end{aligned}$$

Noting that $U \times B$ points in the perpendicular direction, finally:

$$\begin{aligned}\mathbf{v}_{\alpha\mathbf{n}\perp} = \frac{\Omega_\alpha \nu_\alpha}{|\mathbf{B}|(\Omega_\alpha^2 + \nu_\alpha^2)}(\mathbf{E}_\perp + \mathbf{U} \times \mathbf{B}) + \frac{\Omega_\alpha^2}{|\mathbf{B}|(\Omega_\alpha^2 + \nu_\alpha^2)}(\mathbf{E} + \mathbf{U} \times \mathbf{B}) \times \hat{\mathbf{b}} \\ - \frac{\nu_\alpha^2}{\Omega_\alpha^2 + \nu_\alpha^2} d_\alpha \frac{\nabla_\perp n_\alpha}{n_\alpha} - \frac{\Omega_\alpha \nu_\alpha}{\Omega_\alpha^2 + \nu_\alpha^2} d_\alpha \frac{\nabla n_\alpha \times \hat{\mathbf{b}}}{n_\alpha} \\ + \frac{\nu_\alpha}{\Omega_\alpha^2 + \nu_\alpha^2}\mathbf{g}_\perp + \frac{\Omega_\alpha}{\Omega_\alpha^2 + \nu_\alpha^2}\mathbf{g} \times \hat{\mathbf{b}}\end{aligned} \tag{C.20}$$

For $\mathbf{v}_{\alpha\mathbf{n}\|}(= v_{\alpha n\|}\hat{\mathbf{b}})$:

$$n_\alpha(q_\alpha \mathbf{v}_{\alpha\mathbf{n}} \times \mathbf{B} - m_\alpha \nu_\alpha \mathbf{v}_{\alpha\mathbf{n}}) = \kappa_B T_\alpha \nabla n_\alpha - n_\alpha m_\alpha \mathbf{g} - n_\alpha q_\alpha \mathbf{E}_\mathbf{n} \tag{C.21}$$

$$n_\alpha(q_\alpha \mathbf{v}_{\alpha\mathbf{n}} \times \mathbf{B} - m_\alpha \nu_\alpha \mathbf{v}_{\alpha\mathbf{n}}) \cdot \hat{\mathbf{b}} = [\kappa_B T_\alpha \nabla n_\alpha - n_\alpha m_\alpha \mathbf{g} - n_\alpha q_\alpha (\mathbf{E} + \mathbf{U} \times \mathbf{B})] \cdot \hat{\mathbf{b}} \tag{C.22}$$

$$-n_\alpha m_\alpha \nu_\alpha v_{\alpha n\|} = \kappa_B T_\alpha |\nabla_\| n_\alpha| - n_\alpha m_\alpha |\mathbf{g}_\|| - n_\alpha q_\alpha |\mathbf{E}_\|| \tag{C.23}$$

$$v_{\alpha n\|} = \frac{1}{n_\alpha m_\alpha \nu_\alpha}(-\kappa_B T_\alpha |\nabla_\| n_\alpha| + n_\alpha m_\alpha |\mathbf{g}_\|| + n_\alpha q_\alpha |\mathbf{E}_\||) \tag{C.24}$$

$$v_{\alpha n\|} = -d_\alpha \frac{|\nabla_\| n_\alpha|}{n_\alpha} + \frac{|\mathbf{g}_\||}{\nu_\alpha} + \frac{q_\alpha}{m_\alpha \nu_\alpha} |\mathbf{E}_\|| \tag{C.25}$$

3. Plugging Eq. C.20 and C.25 into the current density equation ($\mathbf{J}$):

$$\mathbf{J} = \sum_\alpha n_\alpha q_\alpha \mathbf{v}_\alpha = \sum_\alpha n_\alpha q_\alpha \mathbf{v}_{\alpha\mathbf{n}} \tag{C.26}$$

$$\mathbf{J} = \sum_\alpha n_\alpha q_\alpha \mathbf{v}_{\alpha\mathbf{n}} = \sum_\alpha n_\alpha q_\alpha (\mathbf{v}_{\alpha\mathbf{n}\|} + \mathbf{v}_{\alpha\mathbf{n}\perp}) \tag{C.27}$$

$$\mathbf{J} = \sum_\alpha n_\alpha q_\alpha \left[\frac{\Omega_\alpha \nu_\alpha}{|\mathbf{B}|(\Omega_\alpha^2 + \nu_\alpha^2)} (\mathbf{E}_\perp + \mathbf{U} \times \mathbf{B}) + \frac{\Omega_\alpha^2}{|\mathbf{B}|(\Omega_\alpha^2 + \nu_\alpha^2)} (\mathbf{E} + \mathbf{U} \times \mathbf{B}) \times \hat{\mathbf{b}} \right.$$
$$- \frac{\nu_\alpha^2}{\Omega_\alpha^2 + \nu_\alpha^2} d_\alpha \frac{\nabla_\perp n_\alpha}{n_\alpha} - \frac{\Omega_\alpha \nu_\alpha}{\Omega_\alpha^2 + \nu_\alpha^2} d_\alpha \frac{\nabla n_\alpha \times \hat{\mathbf{b}}}{n_\alpha} + \frac{\nu_\alpha}{\Omega_\alpha^2 + \nu_\alpha^2} \mathbf{g}_\perp + \frac{\Omega_\alpha}{\Omega_\alpha^2 + \nu_\alpha^2} \mathbf{g} \times \hat{\mathbf{b}}$$
$$\left. - d_\alpha \frac{\nabla_\parallel n_\alpha}{n_\alpha} + \frac{\mathbf{g}_\parallel}{\nu_\alpha} + \frac{q_\alpha}{m_\alpha \nu_\alpha} \mathbf{E}_\parallel \right]$$

$$\mathbf{J} = \sum_\alpha n_\alpha q_\alpha \left[\frac{\Omega_\alpha \nu_\alpha}{|\mathbf{B}|(\Omega_\alpha^2 + \nu_\alpha^2)} (\mathbf{E}_\perp + \mathbf{U} \times \mathbf{B}) + \frac{\Omega_\alpha^2}{|\mathbf{B}|(\Omega_\alpha^2 + \nu_\alpha^2)} (\mathbf{E} + \mathbf{U} \times \mathbf{B}) \times \hat{\mathbf{b}} + \frac{q_\alpha}{m_\alpha \nu_\alpha} \mathbf{E}_\parallel \right.$$
$$- \frac{\nu_\alpha^2}{\Omega_\alpha^2 + \nu_\alpha^2} d_\alpha \frac{\nabla_\perp n_\alpha}{n_\alpha} - \frac{\Omega_\alpha \nu_\alpha}{\Omega_\alpha^2 + \nu_\alpha^2} d_\alpha \frac{\nabla n_\alpha \times \hat{\mathbf{b}}}{n_\alpha} - d_\alpha \frac{\nabla_\parallel n_\alpha}{n_\alpha}$$
$$\left. + \frac{\nu_\alpha}{\Omega_\alpha^2 + \nu_\alpha^2} \mathbf{g}_\perp + \frac{\Omega_\alpha}{\Omega_\alpha^2 + \nu_\alpha^2} \mathbf{g} \times \hat{\mathbf{b}} + \frac{\mathbf{g}_\parallel}{\nu_\alpha} \right]$$

$$\mathbf{J} = \sum_\alpha n_\alpha q_\alpha \left[\frac{\Omega_\alpha \nu_\alpha}{|\mathbf{B}|(\Omega_\alpha^2 + \nu_\alpha^2)} (\mathbf{E}_\perp + \mathbf{U} \times \mathbf{B}) + \frac{\Omega_\alpha^2}{|\mathbf{B}|(\Omega_\alpha^2 + \nu_\alpha^2)} (\mathbf{E} + \mathbf{U} \times \mathbf{B}) \times \hat{\mathbf{b}} + \frac{q_\alpha}{m_\alpha \nu_\alpha} \mathbf{E}_\parallel \right]$$
$$- \sum_\alpha n_\alpha q_\alpha \left[\frac{\nu_\alpha^2}{\Omega_\alpha^2 + \nu_\alpha^2} d_\alpha \frac{\nabla_\perp n_\alpha}{n_\alpha} + \frac{\Omega_\alpha \nu_\alpha}{\Omega_\alpha^2 + \nu_\alpha^2} d_\alpha \frac{\nabla n_\alpha \times \hat{\mathbf{b}}}{n_\alpha} + d_\alpha \frac{\nabla_\parallel n_\alpha}{n_\alpha} \right]$$
$$+ \sum_\alpha n_\alpha q_\alpha \left[\frac{\nu_\alpha}{\Omega_\alpha^2 + \nu_\alpha^2} \mathbf{g}_\perp + \frac{\Omega_\alpha}{\Omega_\alpha^2 + \nu_\alpha^2} \mathbf{g} \times \hat{\mathbf{b}} + \frac{\mathbf{g}_\parallel}{\nu_\alpha} \right]$$

$$\mathbf{J} = \sum_\alpha n_\alpha q_\alpha \frac{\Omega_\alpha \nu_\alpha}{|\mathbf{B}|(\Omega_\alpha^2 + \nu_\alpha^2)} (\mathbf{E}_\perp + \mathbf{U} \times \mathbf{B}) + \sum_\alpha n_\alpha q_\alpha \frac{\Omega_\alpha^2}{|\mathbf{B}|(\Omega_\alpha^2 + \nu_\alpha^2)} (\mathbf{E} + \mathbf{U} \times \mathbf{B}) \times \hat{\mathbf{b}}$$
$$+ \sum_\alpha n_\alpha q_\alpha \frac{q_\alpha}{m_\alpha \nu_\alpha} \mathbf{E}_\parallel$$
$$- \sum_\alpha n_\alpha q_\alpha \frac{\nu_\alpha^2}{\Omega_\alpha^2 + \nu_\alpha^2} d_\alpha \frac{\nabla_\perp n_\alpha}{n_\alpha} - \sum_\alpha n_\alpha q_\alpha \frac{\Omega_\alpha \nu_\alpha}{\Omega_\alpha^2 + \nu_\alpha^2} d_\alpha \frac{\nabla n_\alpha \times \hat{\mathbf{b}}}{n_\alpha} - \sum_\alpha n_\alpha q_\alpha d_\alpha \frac{\nabla_\parallel n_\alpha}{n_\alpha}$$
$$+ \sum_\alpha n_\alpha q_\alpha \frac{\nu_\alpha}{\Omega_\alpha^2 + \nu_\alpha^2} \mathbf{g}_\perp + \sum_\alpha n_\alpha q_\alpha \frac{\Omega_\alpha}{\Omega_\alpha^2 + \nu_\alpha^2} \mathbf{g} \times \hat{\mathbf{b}} + \sum_\alpha n_\alpha q_\alpha \frac{\mathbf{g}_\parallel}{\nu_\alpha}$$

Defining a set of constants:

$$\sigma_P = \sum_\alpha n_\alpha q_\alpha \frac{\Omega_\alpha \nu_\alpha}{|\mathbf{B}|(\Omega_\alpha^2 + \nu_\alpha^2)};\ \sigma_H = -\sum_\alpha n_\alpha q_\alpha \frac{\Omega_\alpha^2}{|\mathbf{B}|(\Omega_\alpha^2 + \nu_\alpha^2)};\ \sigma_o = \sum_\alpha \frac{n_\alpha q_\alpha^2}{m_\alpha \nu_\alpha} \tag{C.28}$$

$$d_{P\alpha} = \frac{q_\alpha \nu_\alpha}{\Omega_\alpha^2 + \nu_\alpha^2}\frac{k_B T_\alpha}{m_\alpha};\ d_{H\alpha} = \frac{q_\alpha \Omega_\alpha}{\Omega_\alpha^2 + \nu_\alpha^2}\frac{k_B T_\alpha}{m_\alpha};\ d_{o\alpha} = \frac{q_\alpha}{\nu_\alpha}\frac{k_B T_\alpha}{m_\alpha} \tag{C.29}$$

$$\gamma_P = \sum_\alpha \frac{n_\alpha q_\alpha \nu_\alpha}{\Omega_\alpha^2 + \nu_\alpha^2};\ \gamma_H = \sum_\alpha \frac{n_\alpha q_\alpha \Omega_\alpha}{\Omega_\alpha^2 + \nu_\alpha^2};\ \gamma_o = \sum_\alpha \frac{n_\alpha q_\alpha}{\nu_\alpha}. \tag{C.30}$$

where the σ, d, and γ terms are conductivity, diffusion, and gravity coefficients, respectively. The subscripts P, H, and o indicate Pedersen, Hall, and direct (parallel to the magnetic field) quantities, respectively. This allows us to rewrite the current density equation as

$$\begin{aligned}\mathbf{J} = \sigma_P(\mathbf{E}_\perp + \mathbf{U}\times\mathbf{B}) + \sigma_H\hat{\mathbf{b}}\times(\mathbf{E}+\mathbf{U}\times\mathbf{B}) + \sigma_o E_\parallel \\ - \sum_\alpha \left(d_{P\alpha}\nabla_\perp n_\alpha + d_{H\alpha}\nabla n_\alpha \times \hat{\mathbf{b}} + d_{o\alpha}\nabla_\parallel n_\alpha\right) \\ + \gamma_P \mathbf{g}_\perp + \gamma_H \mathbf{g}\times\hat{\mathbf{b}} + \gamma_o \mathbf{g}_\parallel.\end{aligned} \tag{C.31}$$

BIBLIOGRAPHY

Aggson, T. L., W. J. Burke, N. C. Maynard, W. B. Hanson, P. C. Anderson, J. A. Slavin, W. R. Hoegy, and J. L. Saba, Equatorial bubbles updrafting at supersonic speeds, *J. Geophys. Res.*, *97*, 8,581–8,590, 1992.

Aveiro, H. C., and D. L. Hysell, Three-dimensional numerical simulation of equatorial *F*-region plasma irregularities with bottomside shear flow, *J. Geophys. Res.*, *115*, A11321, 2010*a*.

Aveiro, H. C., and D. L. Hysell, Forecast assessment of topside spread *F* at Jicamarca, *J. Geophys. Res.*, *115*, A12331, 2010*b*.

Aveiro, H. C., D. L. Hysell, J. Park, and H. Lühr, Equatorial spread *F*-related currents: Three-dimensional simulations and observations, *Geophys. Res. Lett.*, *38*, L21103, 2011.

Aveiro, H. C., D. L. Hysell, R. G. Caton, K. M. Groves, J. Klenzing, R. F. Pfaff, R. A. Stoneback, and R. A. Heelis, Three-dimensional numerical simulations of equatorial spread *F*: results and observations in the Pacific sector, *J. Geophys. Res.*, *117*, A03325, 2012.

Bates, D. R., Oxygen green and red line emission and o2+ dissociative recombination, *Planet. Space Sci.*, *38, 7*, 889–902, 1990.

Berkner, L. V., and H. W. Wells, *F*-region ionosphere - Investigation at low latitudes, *Terres. Magn.*, *39*, 215, 1934.

Bhattacharyya, A., and W. J. Burke, A transmission line analogy for the development of equatorial ionospheric bubbles, *J. Geophys. Res.*, *105, A11*, 24,941–24,950, 2000.

Bilitza, D., International Reference Ionosphere 2000, *Radio Sci.*, *36(2)*, 261, 2000.

Bilitza, D., and B. W. Reinisch, International Reference Ionosphere 2007: Improvements and new parameters, *Adv. Space Res.*, *42*, 599–609, 2008.

Brasseur, G. P., and S. Solomon, *Aeronomy of the middle atmosphere - chemistry and physics of the stratosphere and mesosphere*, 651 pp., Springer, Dordrecht, 2005.

Chakrabarti, N., and G. S. Lakhina, Collisional Rayleigh-Taylor instability and shear-flow in equatorial spread *F* plasma, *Ann. Geophys.*, *21*, 1153, 2003.

Chapagain, N. P., B. G. Fejer, and J. L. Chau, Climatology of postsunset equatorial spread f over jicamarca, *J. Geophys. Res.*, *114, A07307*, 2009.

Chau, J. L., R. F. Woodman, M. A. Milla, and E. Kudeki, Naturally enhanced ion-line spectra around the equatorial 150-km region, *Ann. Geophys.*, *27*, 933–942, 2009.

Chou, S. Y., and F. S. Kuo, A numerical study of the wind field effect on the growth and observability of equatorial spread F, *J. Geophys. Res.*, *101*, 17,137, 1996.

Daniell, R. E., L. D. Brown, D. N. Anderson, M. W. Fox, P. H. Doherty, D. T. Decker, J. J. Sojka, and R. W. Schunk, PIM: a global parameterization based on first principles models, *Radio Sci.*, *30*, 1499, 1995.

Drake, J. F., and J. D. Huba, Dynamics of three-dimensional ionospheric plasma clouds, *Phys. Rev. Lett.*, *58, 3*, 278–281, 1987.

Drake, J. F., J. D. Huba, and S. T. Zalesak, Finite temperature stabilization of the gradient drift instability in barium clouds, *J. Geophys. Res.*, *90, A6*, 5227–5234, 1985.

Drob, D. P., An empirical model of the Earth's horizontal wind fields: HWM07, *J. Geophys. Res.*, *113, A12304*, doi:10.1029/2008JA013668, 2008.

Farley, D. T., B. B. Balsley, R. F. Woodman, and J. P. McClure, Equatorial spread *F*: Implications of VHF radar observations, *J. Geophys. Res.*, *75*, 7199, 1970.

Fejer, B. G., and D. L. Hysell, Radar studies of equatorial spread *F*, in *Physics of Space Plasmas, no. 15*, MIT, Cambridge, MA, 1998.

Fejer, B. G., and M. C. Kelley, Ionospheric irregularities, *Rev. Geophys.*, *18*, 401, 1980.

Fejer, B. G., L. Scherliess, and E. R. de Paula, Effects of the vertical plasma drift velocity on the generation and evolution of equatorial spread *F*, *J. Geophys. Res.*, *104*, 19,859, 1999.

Forbes, J. M., The equatorial electrojet, *Rev. Geophys.*, *19*, 469, 1981.

Guzdar, P. N., P. Satyanarayana, J. D. Huba, and S. L. Ossakow, Influence of velocity shear on Rayleigh-Taylor instability, *Geophys. Res. Lett.*, *9*, 547, 1983.

Haerendel, G., Theory of equatorial spread *F*, Max-Planck Institute für Physik und Astrophysik, Garching, West Germany, 1973, preprint.

Haerendel, G., and J. V. Eccles, The role of the equatorial electrojet in the evening ionosphere, *J. Geophys. Res.*, *97*, 1181, 1992.

Haerendel, G., J. V. Eccles, and S. Cakir, Theory for modeling the equatorial evening ionosphere and the origin of the shear in the horizontal plasma flow, *J. Geophys. Res.*, *97*, 1209, 1992.

Hargreaves, J. K., *The solar-terrestrial environment*, 434 pp., Cambridge University Press, Cambridge, 1992.

Harten, A., High resolution schemes for hyperbolic conservation laws, *J. Com. Phys*, *49*, 357, 1983.

Hassam, A. B., Nonlinear stabilization of the Rayleigh-Taylor instability by external velocity shear, *Phys. Fluids*, *4*, 485, 1992.

Hedin, A. E., Extension of the MSIS theromspheric model into the lower and middle atmosphere, *J. Geophys. Res.*, *96*, 1159, 1991.

Hedin, A. E., E. L. Flemming, A. H. Manson, F. J. Schmidlin, S. K. Avery, R. R. Clark, S. J. Franke, G. J. Fraser, T. Tsuda, F. Vial, and R. A. Vincent, Empirical wind model for the upper, middle, and lower atmosphere, *J. Atmos. Terr. Phys.*, *58*, 1421, 1996.

Huang, C.-S., and M. C. Kelley, Nonlinear evolution of equatorial spread F – 1. on the role of plasma instabilities and spatial resonance associated with gravity wave seeding, *J. Geophys. Res.*, *101*, 283–292, 1996.

Huang, C. Y., O. de La Beaujardiere, R. F. Pfaff, J. M. Retterer, P. A. Roddy, D. E. Hunton, Y.-J. Su, S.-Y. Su, and F. J. Rich, Zonal drift of plasma particles inside equatorial plasma bubbles and its relation to the zonal drift of the bubble structure, *J. Geophys. Res.*, *A07316*, 2010.

Huba, J. D., and G. Joyce, Equatorial spread F modeling: Multiple bifurcated structures, secondary instabilities, large density 'bite-outs', and supersonic flows, *Geophys. Res. Lett.*, *34, L07105*, doi:10.1029/2006GL028519, 2007.

Huba, J. D., and G. Joyce, Global modeling of equatorial spread *F*, *Geophys. Res. Lett.*, 2010, submitted.

Huba, J. D., and S. L. Ossakow, On the generation of 3-m irregularities during

equatorial spread *F* by low-frequency drift waves, *J. Geophys. Res.*, *84*, 6697, 1979.

Huba, J. D., G. Joyce, and J. A. Fedder, Sami2 is another model of the ionosphere (SAMI2): A new low-latitude ionospheric model, *J. Geophys. Res.*, *105*, 23,035–23,054, 2000.

Huba, J. D., G. Joyce, and J. Krall, Three-dimensional equatorial spread *F* modeling, *Geophys. Res. Lett.*, *L10102*, 2008.

Hysell, D. L., Radar imaging of equatorial *F* region irregularities with maximum entropy interferometry, *Radio Sci.*, *31*, 1567, 1996.

Hysell, D. L., A review and synthesis of plasma irregularities in equatorial spread *F*, *J. Atmos. Sol. Terr. Phys.*, *62*, 1037, 2000.

Hysell, D. L., and J. Burcham, Long term studies of equatorial spread *F* using the JULIA radar at Jicamarca, *J. Atmos. Sol. Terr. Phys.*, *64*, 1,531, 2002.

Hysell, D. L., and J. L. Chau, Optimal aperture synthesis radar imaging, *Radio Sci.*, *41*, 10.1029/2005RS003383, RS2003, 2006.

Hysell, D. L., and E. Kudeki, Collisional shear instability in the eqautorial *F* region ionosphere, *J. Geophys. Res.*, *109*, (A11301), 2004.

Hysell, D. L., M. Yamamoto, and S. Fukao, Imaging radar observations and theory of type I and type II quasiperiodic echoes, *J. Geophys. Res.*, *107*, 1360, 2002.

Hysell, D. L., J. Chun, and J. L. Chau, Bottom-type scattering layers and equatorial spread *F*, *Ann. Geophys.*, *22*, 4061, 2004.

Hysell, D. L., M. F. Larsen, C. M. Swenson, A. Barjatya, T. F. Wheeler, T. W. Bullett, R. F. Woodman M. F. Sarango, J. L. Chau, and D. Sponseller, Rocket and

radar investigation of background electrodynamics and bottom-type scattering layers at the onset of equatorial spread *F*, *Ann. Geophys.*, *24*, 1387, 2006*a*.

Hysell, D. L., M. F. Larsen, C. M. Swenson, and T. F. Wheeler, Shear flow effects at the onset of equatorial spread *F*, *J. Geophys. Res.*, *111, A11317*, doi: 10.1029/2006JA011923, 2006*b*.

Kelley, M. C., *The Earth's Ionosphere*, 2009.

Kelley, M. C., and D. L. Hysell, Equatorial spread-*F* and neutral atmospheric turbulence: A review and comparative anatomy, *J. Atmos. Terr. Phys.*, *53*, 695, 1991.

Kelley, M. C., M. F. Larsen, and C. La Hoz, Gravity wave interaction of equatorial spread *F*: A case study, *J. Geophys. Res.*, *86*, 9087, 1981.

Kelley, M. C., J. J. Makela, O. de La Beaujardiere, and J. Retterer, Convective ionospheric storms: a review, *Rev. Geophys.*, *RG2003*, 2011.

Keskinen, M. J., H. G. Mitchell, J. A. Fedder, P. Satyanarayana, S. T. Zalesak, and J. D. Huba, Nonlinear evolution of the Kelvin-Helmholtz instability in the high-latitude ionosphere, *J. Geophys. Res.*, *93*, 137, 1988.

Keskinen, M. J., S. L. Ossakow, and B. G. Fejer, Three-dimensional nonlinear evolution of equatorial ionospheric spread-*F* bubbles, *Geophys. Res. Lett.*, *30*, 1855, doi:10.1029/2003GL017418, 2003.

Kil, H., and R. A. Heelis, Global distribution of density irregularities in the equatorial ionosphere, *J. Geophys. Res.*, *103*, 407, 1998.

Kivelson, M. G., and C. T. Russel, *Introduction to space physics*, 568 pp., Cambridge University Press, Cambridge, 1995.

Koons, H. C., J. L. Roeder, and P. Rodriguez, Plasma waves observed inside plasma bubbles in the equatorial *f* region, *J. Geophys. Res.*, *102*(A3), 4,577–4,583, 1997.

Krall, J., J. D. Huba, G. Joyce, and T. Zalesak, Three-dimensional simulation of equatorial spread-F with meridional wind effects, *Ann Geophys.*, *27*, 1821–1830, 2009.

Krall, J., J. D. Huba, S. L. Ossakow, G. Joyce, J. J. Makela, E. S. Miller, and M. C. Kelley, Modeling of equatorial plasma bubbles triggered by non-equatorial traveling ionospheric disturbances, *Geophys. Res. Lett.*, *L08103*, 2011.

Kudeki, E., and S. Bhattacharyya, Post-sunset vortex in equatorial *F*-region plasma drifts and implications for bottomside spread-*F*, *J. Geophys. Res.*, *28*, 28,163, 1999.

Kudeki, E., B. G. Fejer, D. T. Farley, and H. M. Ierkic, Interferometer studies of equatorial *F* region irregularities and drifts, *Geophys. Res. Lett.*, *8*, 377, 1981.

Kudeki, E., A. Akgiray, M. A. Milla, J. L. Chau, and D. L. Hysell, Equatorial spread-F initiation: post-sunset vortex, thermospheric winds, gravity waves, *J. Atmos. Sol. Terr. Phys.*, *69 (17–18)*, 2416–2427, 2007.

La Beaujardiere, O. de, C/NOFS: A mission to forecast scintillations, *J. Atmos. Sol. Terr. Phys.*, *66*, 1573, 2004.

La Beaujardiere, O. de, C/NOFS observations of deep plasma depletions at dawn, *Geophys. Res. Lett.*, *36, L00C06*, doi:10.1029/2009GL038884, 2009.

LaBelle, J., M. C. Kelley, and C. E. Seyler, An analysis of the role of drift waves in equatorial spread *F*, *J. Geophys. Res.*, *91*, 5513, 1986.

Larsen, M. F., Winds and shears in the mesosphere and lower thermosphere: results from four decades of chemical release wind measurements, *J. Geophys. Res.*, *107*, 10.1029/2001JA000218, 2002.

Link, R., and L. L. Cogger, A reexamination of the OI 6300- nightglow, *J. Geophys. Res.*, *93*, 9,883–9,892, 1988.

Link, R., and L. L. Cogger, Correction to 'A reexamination of the OI 6300- nightglow', *J. Geophys. Res.*, *94*, 1,556, 1989.

Lühr, H., S. Maus, M. Rother, and D. Cooke, First in-situ observation of nighttime F region currrents with the CHAMP satellite, *Geophys. Res. Lett.*, *29, 10*, 10.1029/2001GL013845, 2002.

Makela, J. J., and E. S. Miller, Optical observation of the growth and day-to-day variability of equatorial plasma bubbles, *J. Geophys. Res.*, *113, A03307*, 2008.

McClure, J. P., S. Singh, D. K. Bambogye, F. S. Johnson, and H. Kil, Occurrence of equatorial *F* region irregularities: Evidence for tropospheric seeding, *J. Geophys. Res.*, *103*, 29,119, 1998.

Murphy, A. H., Skill score based on the mean square error and their relation to the correlation coefficient, *Monthly Weather Review*, *116*, 2417–2424, 1988.

Niranjan, K., P. S. Brahmanandam, P. Ramakrishna Rao, G. Uma, D. S. V. V. D. Prasad, and P. V. S. Rama Rao, Post midnight spread-f occurrence over waltair (17.7° N, 83.3° E) during low and ascending phases of solar activity, *Ann. Geophys.*, *21*, 745–750, 2003.

Ossakow, S. L., Spread *F* theories – A review, *J. Atmos. Terr. Phys.*, *43*, 437, 1981.

Park, J., H. Lühr, C. Stolle, M. Rother, K. W. Min, and I. Michaelis, The characteristics of field-aligned currents associates with equatorial plasma bubbles as observed by the CHAMP satellite, *Ann. Geophys.*, *27*, 2685–2697, 2009.

Park, J., H. Lühr, C. Stolle, M. Rother, K. W. Min, and I. Michaelis, Characteristics of *F*-region dynamo currents deduced from CHAMP magnetic field measurements, *J. Geophys. Res.*, *115*, A10302, 2010.

Picone, J. M., A. E. Hedin, D. P. Drob, and A. C. Aikin, NRLMSISE-00 empirical model of the atmosphere: Statistical comparisons and scientific issues, *J. Geophys. Res.*, *107, A12*, doi: 10.1029/2002JA009430, 2002.

Pottelette, R., M. Malingre, J. J. Berthelier, E. Seran, and M. Parrot, Filamentary Alfvénic structures excited at the edges of equatorial plasma bubbles, *Ann. Geophys.*, *25*, 2159–2165, 2007.

Retterer, J. M., Physics-based forecasts of equatorial radio scintillation for the Communication and Navigation Outage Forecasting System (C/NOFS), *Space Weather*, *3*, S12C03, doi:10.1029/2005SW000146, 2005.

Retterer, J. M., Forecasting low-latitude radio scintillation with 3-D ionospheric plume models: 1. Plume model, *J. Geophys. Res.*, *115, A03306*, doi:10.1029/2008JA013839, 2010.

Retterer, J. M., D. T. Decker, W. S. Borer, R. E. Daniell Jr., and B. G. Fejer, Assimilative modeling of the equatorial ionosphere for scintillation forecasting: Modeling with vertical drifts, *J. Geophys. Res.*, *110*, A11307, doi:10.1029/2002JA009613, 2005.

Richmond, A. D., Numerical model of the equatorial electrojet, *AFCRL–72–*

0668, ERP 421, Air Force Cambridge Research Lab., Hanscom AFB, Bedford, MA, 1972.

Roble, R. G., and E. C. Ridley, A thermosphere-ionosphere-mesosphere-electrodynamics general circulation model, *Geophys. Res. Lett.*, *21*, 417, 1994.

Roe, P. L., Characteristic-based schemes for the euler equations, *Ann. Rev. Fluid Mech.*, *18*, 337, 1986.

Röttger, J., Wavelike structures of large scale equatorial spread *F* irregularities, *J. Atmos. Terr. Phys.*, *35*, 1195, 1973.

Saad, Y., SPARSKIT : A basic tool kit for sparse matrix computations, *RIACS–90–20*, Research Institute for Advanced Computer Science, NASA Ames Research Center, Moffett Field, CA, 1990.

Satyanarayana, P., Y. C. Lee, and J. D. Huba, The stability of a stratefied shear layer, *Phys. Fluids*, *30*, 81, 1987.

Scannapieco, A. J., and S. L. Ossakow, Nonlinear equatorial spread F, *Geophys. Res. Lett.*, *3, 8*, 451–454, 1976.

Scannapieco, A. J., S. L. Ossakow, S. R. Goldman, and J. M. Pierre, Plasma cloud late time striation spectra, *J. Geophys. Res.*, *81*, 6037, 1976.

Scherliess, L., and B. G. Fejer, Radar and satellite global equatorial *F* region vertical drift model, *J. Geophys. Res.*, *104, A4*, 6829–6842, 1999.

Shume, E. B., D. L. Hysell, and J. L. Chau, Zonal wind velocity profiles in the equatorial electrojet derived from phase velocities of type II radar echoes, *J. Geophys. Res.*, *110*, A12308, doi:10.1029/2005JA011210, 2005.

Singh, S., F. S. Johnson, and R. A. Power, Gravity wave seeding of equatorial plasma bubbles, *J. Geophys. Res.*, *102*, 7399, 1997.

Singh, S. B., K. Patel, R. P. Patel, A. K. Singh, and R. P. Singh, Modeling of VHF scintillation observed at low latitude, *J. Phys.: Conf. Ser.*, *208 (1)*, 012065, 2010.

Sobral, J. H. A., H. Takahashi, M. A. Abdu, P. Muralikrishna, Y. Sahai, C. J. Zamlutti, E. R. de Paula, and P. P. Batista, Determination of the quenching rate of the o(1d) by o(3p) from rocket-borne optical (630 nm) and electron density data, *J. Geophys. Res.*, *98, A5*, 7791–7798, 1993.

Stening, R. J., and B. G. Fejer, Lunar tide in the equatorial f region vertical ion drift velocity, *J. Geophys. Res.*, *106, A1*, 221–226, 2001.

Stening, R. J., C. Carmody, and J. Du, Simulating the lunar geomagnetic variations, *J. Geophys. Res.*, *107, A7*, 1125, 2002.

Stolle, C., H. Lühr, M. Rother, and G. Balasis, Magnetic signatures of equatorial spread *F* as observed by the CHAMP satellite, *J. Geophys. Res.*, *111, A02304*, doi:10.1029/2005JA011184, 2006.

Strang, G., On the construction and comparison of difference schemes, *SIAM J. Num. Anal.*, *5*, 506–517, 1968.

Sultan, P. J., Linear theory and modeling of the Rayleigh-Taylor instability leading to the occurrence of equatorial spread *F*, *J. Geophys. Res.*, *101*, 26,875, 1996.

Sweby, P. K., High resolution schemes using flux limiters for hyperbolic conservation laws, *SIAM Journal on Numerical Analysis*, *21*(5), 995–1011, 1984.

Tinsley, B. A., Field aligned airglow observations of transequatorial bubbles in the tropical *F*-region, *J. Atmos. Terr. Phys.*, *44*, 547–557, 1982.

Trac, H., and U. L. Pen, A primer on Eulerian computational fluid dynamics for astrophysicists, *Astrophysics*, *115*, 303–321, 2003.

Tsunoda, R. T., On the enigma of day-to-day variability in equatorial spread *F*, *Geophys. Res. Lett.*, *32*, L08103, doi:10.1029/2005GL022512, 2005.

Tsunoda, R. T., and B. R. White, On the generation and growth of equatorial backscatter plumes. 1. Wave structure in the bottomside *F* layer, *J. Geophys. Res.*, *86*, 3610, 1981.

Tsunoda, R. T., M. J. Barons, J. Owen, and D. M. Towle, Altair: An incoherent scatter radar for equatorial spread *F* studies, *Radio Sci.*, *14*, 1111, 1979.

Tsunoda, R. T., R. C. Livingston, and C. L. Rino, Evidence of a velocity shear in bulk plasma motion associated with the post-sunset rise of the equatorial *F* layer, *Geophys. Res. Lett.*, *8*, 807, 1981.

Vadas, S. L., and D. C. Fritts, Thermospheric response to gravity waves arising from mesoscale convective complexes, *J. Atmos. Sol. Terr. Phys.*, *66*, 781, 2004.

Van-Leer, B., Towards the ultimate conservation difference scheme. II. Monotonicity and conservation combined in a second-order scheme, *J. Comp. Phys.*, *14*, 361, 1974.

Vorst, H. van der, Bi-CGSTAB: A fast and smoothly converging variant of Bi-CG for the solution of nonsymmetric linear systems, *SIAM J. Sci. Statist. Comput.*, *13*, 631–644, 1992.

Woodman, R. F., Coherent radar imaging: Signal processing and statistical properties, *Radio Sci.*, *32*, 2373, 1997.

Woodman, R. F., Spread F- An old equatorial aeronomy problem finally resolved?, *Ann. Geophys.*, *27*, 1915–1934, 2009.

Woodman, R. F., and C. La Hoz, Radar observations of *F* region equatorial irregularities, *J. Geophys. Res.*, *81*, 5447, 1976.

Yokoyama, T., Y. Otsuka, T. Ogawa, M. Yamamoto, and D. L. Hysell, Three-dimensional simulation of the coupled Perkins and *Es* layer instabilities in the nighttime midlatitude ionosphere, *J. Geophys. Res.*, *114, A03308*, doi:10.1029/2008JA013789, 2009.

Zalesak, S. T., and S. L. Ossakow, Nonlinear equatorial spread F: Spatially large bubbles resulting from large horizontal scale initial perturbations, *J. Geophys. Res.*, *85, A5*, 2131–2142, 1980.

Zalesak, S. T., S. L. Ossakow, and P. K. Chaturvedi, Nonlinear equatorial spread *F* - The effect of neutral winds and background Pedersen conductivity., *J. Geophys. Res.*, *87*, 151, 1982.

Zargham, S., and C. E. Seyler, Collisional interchange instability, 1, Numerical simulations of intermediate-scale irregularities, *J. Geophys. Res.*, *92*, 10,073, 1987.

Zargham, S., and C. E. Seyler, Collisional and inertial dynamics of the ionospheric interchange instability, *J. Geophys. Res.*, *94*, 9009, 1989.